University of Technology, Sydney

A Study of Fluid Structure Interactions in Hydraulic Piping of Passive Interconnected Suspensions

by

Jing Zhao

Submitted in fulfilment of the requirements for the degree of

Doctor of Philosophy

Faculty of Engineering and Information Technology

University of Technology, Sydney

May, 2014

CERTIFICATE OF ORIGINAL AUTHORSHIP

I certify that the work in this thesis has not previously been submitted for a degree nor has it been submitted as part of the requirements for a degree except as fully acknowledged within the text.

I also certify that the thesis has been written by me. Any help that I have received in my research work and the preparation of the thesis itself has been acknowledged. In addition, I certify that all information sources and literature used are indicated in the thesis.

Signed

_____

Jing Zhao

Date:

ACKNOWLEDGEMENTS

I would like to express my sincere gratitude my supervisor Professor Nong Zhang. He has been a tremendous mentor for me. I would like to thank him for encouraging my research and for helping me to grow as a research scientist. Special thanks are also extended to my co-supervisor, Dr. Jinchen Ji. He has always been very approachable and helpful. The advice that both of these mentors have given me has been priceless.

I would also like to thank Chris Chapman for his expertise in the lab. His extensive knowledge on both the hardware and software in the laboratory has been most helpful. It has also been enormously beneficial in terms of this project. I extend my gratitude to my colleagues, Dr. Wenlong Hu, Dr. Wade Smith and Dr. Paul Walker for their invaluable help. The financial and infrastructure support for this work by the Australian Research Council, my supervisor and the University of Technology, Sydney, is also gratefully acknowledged.

Many thanks to my family for the love and support they have given me over the years. Words cannot express how grateful I am to my parents for all of the sacrifices that they have made on my behalf. Their consistent encouragement has quite literally sustained me throughout my endeavours.

Jing Zhao
Sydney, April 2014

TABLE OF CONTENTS

NOMENCLATURE & ACRONYM

Variables (for pipe wall or hose wall):

f_x	lateral shear force	F_x	lateral shear force amplitude
f_y	lateral shear force	F_y	lateral shear force amplitude
f_z	axial force	F_z	axial force amplitude
m_x	bending moment to x axis	M_x	bending moment amplitude to x axis
m_y	bending moment to y axis	M_y	bending moment amplitude to y axis
m_z	bending moment to z axis	M_z	bending moment amplitude to z axis
u_x	lateral displacement	U_x	lateral displacement amplitude
u_y	lateral displacement	U_y	lateral displacement amplitude
u_z	axial displacement	U_z	axial displacement amplitude
θ_x	rotate angle to x axis	Θ_x	rotate angle amplitude to x axis
θ_y	rotate angle to y axis	Θ_y	rotate angle amplitude to y axis
θ_z	rotate angle to z axis	Θ_z	rotate angle amplitude to z axis

Variables (for fluid):

p	axial pressure	P	axial pressure amplitude
v	axial velocity	V	axial displacement amplitude

Independent variables:

t	time	x	lateral axis
z	axial axis	y	lateral axis
x	lateral axis	ω	angular frequency

Coefficients:

A	cross-sectional area (m^2)
c_r	circumference of reinforcement of hose wall (m)
D	damping coefficient per unit length (s^{-1})
e	wall thickness (m)
E	Young's modulus of pipe wall (Pa)
E_x	lateral Young's modulus of hose wall (Pa)
E_z	axial Young's modulus of hose wall (Pa)
G	shear modulus of wall (Pa)

I area moment of inertia (m^4)

I^M moment of inertia (kg m^2)

J polar moment of inertia (m^4)

K_E modified bulk modulus of hose section (Pa)

K^* modified fluid bulk modulus of pipe section (Pa)

l length of section or distance (m)

L inductance of hydraulic component

n friction coefficient (s^{-1})

q fluid flow (m^3)

r inner radius of pipe/hose wall (m)

$\bar{r}$ mean radius of pipe wall (m)

r_r radius of reinforcement of hose wall (m)

~~R~~ radius of curvature of pipe bend (m)

R resistance of hydraulic component

~~V~~ volume of gas (m^3)

Z impedance characteristics

γ ratio of specific heats for nitrogen

η rigidity factor for stiffness of elbow

κ shear coefficient for hollow circle cross section

ν Poisson's ratio of pipe wall

ν_x lateral Poisson's ratio of hose wall

ν_z axial Poisson's ratio of hose wall

ρ mass density (kg/m^3)

Subscripts:

f fluid

p pipe wall

h hose wall

m concentrated mass

o orifice

a accumulator

ao orifice at neck of accumulator

pre manufacturer parameter of accumulator

LIST OF FIGURES

LIST OF TABLES

ABSTRACT

This thesis examines the fluid-induced high-frequency vibrations in the hydraulic pipelines of a recently invented vehicle suspension, namely Hydraulically Interconnected Suspension (HIS), which is applied to overcome the compromise between comfort and handling performance. The basic system of the suspension is a liquid-filled pipe-guided fluidic circuit, inside which the produced pressure changes often lead to vibrations of the whole pipeline and associated structures and hence become a source of noise. The results of this study can be extended to similar piping systems.

The modelling approach proposed here is necessarily multidisciplinary, covering vibration theory and fluid dynamics. The one-dimensional wave theory is employed to formulate the equations of motions that govern the dynamics of the fluid-structural system. Piping sections are defined as continuous line elements and discontinuities between the sections as point elements.

The Transfer Matrix Method (TMM) is applied to determine the relationships between individual components. The resulting sets of linear, frequency-dependent state-space equations, which govern the coupled dynamics of the system, are derived and then applied in a variety of ways. Key parameters that influence system dynamics are identified and analyses of their effects are presented.

The theoretical model is validated by experimental investigations. Two piping systems are assembled and free vibration results acquired through both the systems agree well with those of the proposed linear models. The deviation is reasonable and possible impact factors are described. However, the results from a different system configuration reveal the limitations in terms of the linear modelling to precisely represent curved hoses.

The methodology presented is found to be an effective and useful way of modelling liquid-filled pipe-guided piping systems, particularly in the frequency domain. The ob-

tained results suggest possible improvements can be made in relation to decreasing the fluid induced vibration in the piping system and the surrounding structures. However, further investigation is needed. For example, the development of the precise hose bend model or the coupling between the piping system and the connected structures could provide the topic of future studies.

Chapter 1

INTRODUCTION

1.1 Basic Structure and Function of Vehicle Suspension System

The suspension system of a conventional road vehicle is basically composed of three crucial elements: springs, shock absorbers and linkage parts, by which the vehicle body and its wheels are connected. Suspension systems serve two functional aspects: one is for safe handling and driving pleasure, the other is for comfort by isolating the driver and passengers from road shock forces [1]. The isolation from road bumps and vibrations also improves the longevity and durability of the vehicle [2].

Specifically, the primary function of a suspension system is to [3, 4]:

Support the vehicle body
Keep the tyres in contact with the road
Maintain proper ride height of the vehicle
Keep the wheels following the uneven road
Isolate the chassis from the rough road excitation in order to reduce the shock
Maintain the required wheel position relative to the road surface
Control the orientation of the vehicle travel, and
Resist the chassis roll

1.2 Limitation of Conventional Suspension System

The suspension mode is defined as the vertical motion of all wheels relative to the vehicle body. In the context of a four-wheeled vehicle, there are four modes: bounce, roll, pitch, and warp. The bounce mode occurs when all wheels are in phase; roll occurs when wheels on one side (left/right) are in phase; pitch occurs when wheels at one end (front/rear) are in phase; and,wrap occurs when only wheels diagonally-opposed are in

phase. Figure 1.1 shows the first three modes. Vehicle handling, ride, and noise are defined as low-frequency (≤ 2 Hz) directional response, low-to-mid-frequency (0-25 Hz) perceptible vehicle body vibrations, and high-frequency (> 25 Hz) vibrations respectively [4].

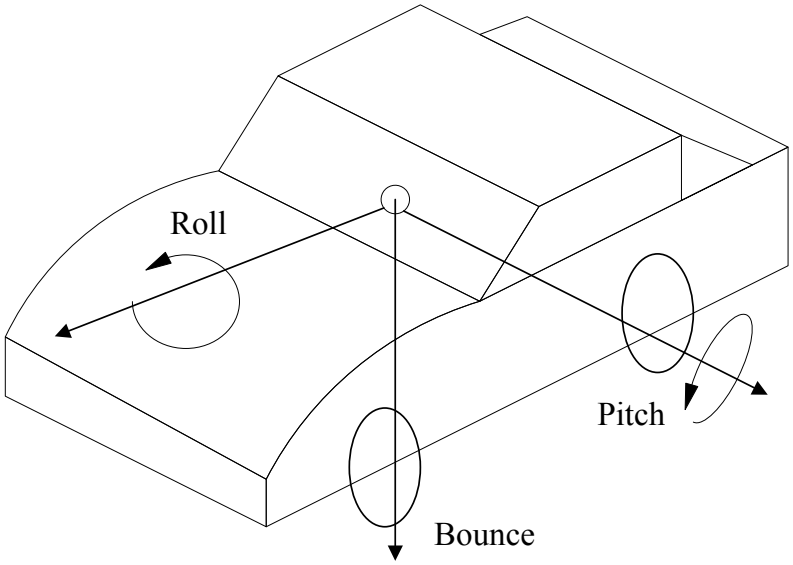

Figure 1.1 Dynamic Modes of Road Vehicle

Conventional suspension systems are generally divided into two groups: solid axles and independent suspensions [4]. The limitation of both groups is the conflict between ride performance and handling effectiveness, which comes from the interdependence of suspension functions between at least two vibration modes. Handling effectiveness directly determines the safety of a vehicle and ride performance represents how comfortable the passengers feel while the vehicle is in motion. Therefore, the most important factor in conventional suspension design is to compromise vehicle safety and passenger comfort.

Rolling is the most dangerous road vehicle mode because it usually incurs serious accidents and can lead to huge losses. Accordingly, a firm suspension can greatly reduce vehicular rollover propensity. On the other hand, in today's highly competitive passenger car market, customers prefer vehicles that provide superior ride comfort, and this typically necessitates a soft, compliant suspension. This conflict between the ride comfort and vehicle handling and stability has led to the development of various advanced suspension systems.

Over the last few decades, the solutions for this problem can generally be divided into two types – active or semi-active suspensions and passive interconnected suspensions. The active or semi-active suspensions improve the vehicle ride performance without compromising handling quality, thus achieving optimisation for all the vibration modes. However, the applications of these advanced suspensions are constrained by extra weight, increased cost, complicated assembly, difficult packaging, reduced reliability, and/or other factors. [1, 4]

Unlike semi-active/active suspensions, passive interconnected suspension can enhance vehicle stability without compromising ride performance by passive suspension technologies. That is, the ride comfort and control efficiency can be achieved without much compromise. Furthermore, the passive suspension technology conquers the drawbacks of active suspension technologies.

1.3 Interconnected Suspension

For conventional suspensions, manufacturers often increase the roll stiffness to avoid vehicle rolling and improve vehicle handling by means of firmer single-wheel springs. However, the stiffer single-wheel springs also increase the stiffness of the bounce, pitch and warp modes, which directly reduces the capacity to isolate road bumps and vibrations from the passengers, in other words, the ride comfort is decreased [5-7]. It is clearly not possible to simultaneously achieve both of the desired goals (ride and handling) at the highest level, as some compromise between the conflicting objectives must be made.

The interconnected suspensions, in which the vehicle's individual wheel stations (i.e., spring-damper elements) are connected to one another, provide greater freedom to assign stiffness and damping properties to each suspension mode, instead of being entirely reliant upon single-wheel station properties to define modal characteristics. The interconneciton can be realised by mechanical, hydraulic and pneumatic means separately or jointly; and can effectively overcome the comfort-handling compromise.

It is noted that fluid interconnections can provide greater potential and flexibility in achieving optimum performance among the various vehicle vibration modes [1]. In

comparsion with mechanical connection, the liquid of hydraulic suspension can increase smooth movement, reduce impacts between elements, and provide more damping in place of damper parts. The hydraulic system is believed to be easier to maintain and simpler to assemble than pneumatic systems. In this way, the requirement of minimal packaging is achieved. Therefore, more vibration can be reduced by the hydraulic suspensions than by mechanical means and the hydraulic linkage produces less maintenance failure than through pneumatic means.

1.4 Hydraulically Interconnected Suspension

Hydraulic systems that are widely used in heavy equipment including certain sub-systems of road vehicles have successfully served their purpose for many years. However, these types of systems have not been applied to light cars until recently. In the last two decades, a number of unique Hydraulically Interconnected Suspension (HIS) systems have been successfully invented and applied to rally cars and passenger vehicles by Kinetic Company, which was bought by a US suspension manufacturer, Tenneco, in 1999 [8]. The study in this thesis focuses on the Kinetic type suspensions, and the approaches can be applied to similar systems.

The Kinetic type HIS systems, no matter what their main purpose is, have a similar system configuration. At each wheel station, a single- or double-acting hydraulic cylinder replaces the vehicle's conventional shock absorber. It sometimes also replaces the spring. The chambers of the cylinders are interconnected by hydraulic circuits, typically containing pipelines, flexible hoses, hydraulic accumulators, damper valves and fittings. Different arrangements of the elements achieve different specific objectives for the suspension.

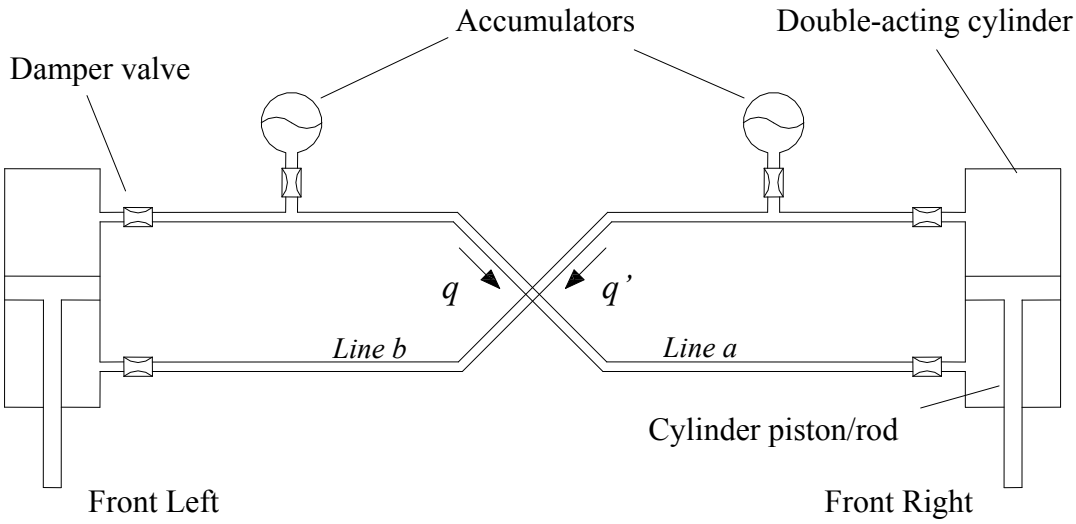

Figure 1.2 Schematic Diagram for Hydraulic Circuit of Half-Car HIS System [9, 10]

Figure 1.2 illustrates an essential structure of the HIS system on the base of the front half of the car. When installed on a vehicle, the piston rods are fixed on wheel stations while the other parts are mounted on the vehicle's chassis. The cylinders and pipes are connected by rubber hoses to accommodate misalignment and reduce mechanical vibration. This type of suspension is particularly useful to improve vehicle rollover resistance [9, 10].

In roll mode, the two pistons move in opposite directions. If we assume that the left piston moves upwards and the right piston moves downwards, fluid flows out of the left-top chamber and the right-bottom chamber. The only place for the displaced fluid is the accumulator on *line a*. Pressure then rises in this line and falls in another line due to the simultaneous fluid flow out of the accumulator on *line b*. A force induced by the pressure difference tends to resist the change, thus stiffness is provided to the roll mode and this increases the anti-roll capacity. [11]

The two pistons move in the same direction when the vehicle is in bounce or pitch mode. If we take the cylinder compression as an example, fluid flows out of the top chambers of both cylinders, which leads to most of the displaced fluid flowing into the bottom chamber of the opposite cylinder. Owing to the piston rods, the volume of each bottom chamber is slightly smaller than the top chamber's volume, thus a small volume of fluid (the rod volume) flows into each of the accumulators and the pressure in both lines

slightly increases. Therefore, the suspension almost has no impact on the bounce and pitch modes, i.e., no change in terms of ride comfort.

The performance of the hydraulic system, which depends upon system volume, system mean pressure, fluid and material properties, valve and cylinder characteristics, accumulator performance, and other system parameters, determines the performance of the whole suspension system. The low-frequency handling effectiveness of the system was investigated in previous research and the results show that for a motor vehicle, the suspension can improve rollover resistance compared with conventional suspension systems [11]. The system performance in low-to-mid-frequency ride performance is well understood [12], but the high-frequency noise characteristics are not clear yet.

Chapter 2

PROJECT DEFINITION

2.1 Problem Statement

The interior noise quality of a vehicle is becoming increasingly important with the advancement in all areas of vehicle technology. The significance of interior noise quality enhancement in automobiles has been identified by Schedlowsky and the need to improve automotive sound quality and control methods has been highlighted [13]. Due to the competitive commercial environment of the modern automotive market, the level of Noise and Vibration Harshness (NVH) is one of the important quality indicators of a passenger car and it must be eliminated or minimised in a cost-effective manner. Further, it has a strong bearing on direct commercial profits and the future success of automotive companies.

The employment of hydraulic systems usually generates undesirable noise. Generally this noise is transmitted from the hydraulic components to the pipeline or connected bodies in the form of fluid or structural vibration. The fluid vibration transmitted along the pipeline is converted to structural vibration by the fluid-structural coupling which occurs at bends, constrictions and terminations. The Fluid-Structural Interaction (FSI) and the resultant acoustic radiation are discussed by Fahy [14]. The structural vibration is transmitted through mountings or supporting structures. This vibration may be transmitted to parts that are remote from the hydraulic system.

The prime cause of Fluid-Borne Noise (FBN) in hydraulic systems is the flow fluctuation that is produced by certain vibration activators. This flow fluctuation acts as an excitation to which the system reacts. If we take the Figure 1.2 as an example, the cylinder parts are fixed on wheel assemblies and the piston rods are made to sit on the car body, or vice-versa. When a vehicle that is equipped with the HIS system runs, the relative movement between wheels and the vehicle body results in the relative movement be-

tween pistons and cylinders. The pressure fluctuations induced by the movement are propagated within the hydraulic circuit and these generate objectionable vibrations.

Since pipe circuits are mounted on the chassis, the vibrations can be transferred to the vehicle structure and become an excitation force to the vehicle. The low- and mid-frequency vibrations influence the vehicle handling and ride whilst the high-frequency vibrations are associated with the vehicle noise. Because the HIS is mounted on the chassis of the vehicle, the vibration induced by the fluid flow dynamically interacts with some of the vehicle's assemblage and/or parts. The dominant natural frequencies of some structures may be high, thus the resonance of high-frequency vibrations of the suspension and other vehicle structures is pronounced and the consequent noise cannot be ignored.

Although the HIS is already developed for application, the advantage of vehicle handling is evaluated by experiments [11], and a theoretical model is established to understand and investigate the vehicle ride performance [12], the understanding of the HIS on high-frequency noise characteristics is absent. Experimental investigations on the existing HIS could be used to develop empirical models and hence develop the understanding of the system. However, it is costly and difficult to analyse the system in order to optimise the system parameters and to apply the knowledge to similar systems.

Therefore, an improved theoretical model of the HIS should be developed for further investigation. To achieve this, the principal part of the HIS – the hydraulic circuit – must be well understood and investigated in detail. In order to effectively reduce the vehicle noise, the focus of this project is to develop an experimentally validated mathematical model of the hydraulic circuit. This serves to investigate the piping system dynamics and high-frequency characteristics, and it provides a theoretical basis for optimising the structural design and assemblage of the HIS system.

2.2 Research Objective and Contribution to Knowledge

In order to extend the understanding on the HIS system and investigate its high-frequency vibration characteristics, a more complicated model for the hydraulic circuit must firstly be developed. The model will be experimentally validated and a sensitivity

analysis of system parameters will be performed with regard to noise problems. The existing HIS can be improved according to the developed model, thus more mature products can be applied to vehicles.

For low-to-mid-frequency investigation, the pipe can be assumed as a rigid body. However, it is inappropriate to use this assumption for high-frequency investigation. Accordingly, an important phenomenon named Fluid-Structure Interaction (FSI) which occurs within the hydraulic system must be considered when the model is developed. The establishment of this model requires the integration of the existing pipe element model and newly developed models of the hydraulic components e.g. hoses, valves, and accumulators.

The proposed contribution to the relative research area and sphere of knowledge is as follows:

(1) develop an in-depth understanding of FSI in the HIS piping circuit;
(2) develop the individual models of hydraulic components and extend the model of pipe element;
(3) develop extensive models for defined hydraulic piping systems;
(4) perform sensitivity analysis of frequency relevant parameters;
(5) provide experimental investigation of vibration characteristics of the HIS system;
(6) recommend possible future works;
(7) improve the understanding of the transfer matrix method (TMM) and impedance method;
(8) provide the theoretical foundation for future optimisation and improvement.

2.3 Outline of Thesis

The existing literature on interconnected suspension systems and hydraulic elements is reviewed in Chapter 3. The developed system and element models are reviewed and the methodologies are described and compared. The relevant studies are also presented and discussed in this chapter.

In Chapter 4, the derived processes of individual component models are described and the development of the system model is presented. The friction coupling and the structural viscous damping are considered as tools to improve the pipe model. The developed hose, valve, and accumulator models are included in the system models.

The experimental investigation is illustrated in Chapter 5. This chapter describes the configurations of the test rig that is used to proceed the experiments. The software and hardware used in the tests are presented and the impact factors are discussed.

Chapter 6 compares the experimental and simulation results and explains the deviation between them. The verification of the system model is presented here.

The impacts of fluidic and structural components on system dynamics are analysed and investigated in Chapter 7. The possibility of reducing noise by modifying the system parameters is discussed.

The thesis concludes in Chapter 8. The achievements and contribution of this research is summarised and possible future studies are recommended by the author.

Chapter 3

LITERATURE REVIEW

3.1 Hydraulically Passive Interconnected Suspension

3.1.1 Early interconnection schemes

One popular way of overcoming the compromise between handling effectiveness and ride comfort is the usage of passive interconnected suspension systems. In this type of system, a displacement at one wheel station can produce forces at other wheel stations [15].

Because of technology limitations, early interconnected suspensions are realised by mechanical means [15, 16]. The anti-roll bar probably is the most simple and widely used interconnection arrangement, although the ride-handling compromise is not successfully resolved by this means. The first widespread suspension interconnections in the automotive industry were realised mechanically on the Citroën 2CV in 1949 [16].

In the 1920s, Hawley [17] invented hydraulic interconnection for suspension systems. Double-acting cylinders were applied in this scheme, but the fluid system transmission characteristics were not considered in detail. Until the 1950s, Moulton's Hydrolastic and Hydragas systems were extensively used, and these hydro-pneumatically interconnected suspension systems attracted widespread interest for about thirty years [18-20]. As shown in Figure 3.1, the gas-liquid containers at each wheel station are connected by pipes.

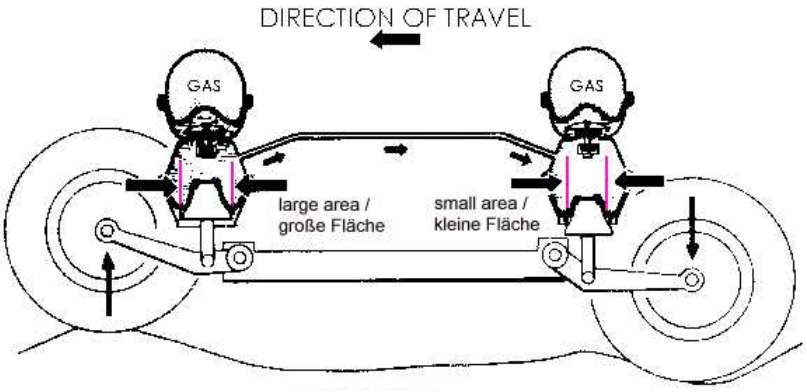

Figure 3.1 Moulton's Hydragas Suspension

Toyota and Nissan developed active interconnected suspensions in pneumatic and hydraulic varieties during the 1980s and 90s, respectively [21, 22]. For both, the emphasis was on the control system development and experimentation instead of detailed fluid system modelling. In the mid 1990s, Liu et al. proposed that a suspension system for increasing roll stiffness could be realised by the hydraulic interconnection form [23-26]. The numerical simulations suggested that roll stiffness could be increased and ride comfort could be improved. However, complex phenomena such as fluid inertia and wave propagation effects were not considered in the modelling techniques. Further, the experimental verification was absent.

3.1.2 Recent research and applications

Most of the aforementioned systems were based on the interconnection of only one pair of wheel stations. Obviously, the extended interconnection of four wheel stations can provide more freedom to manipulate the coupling of different suspension modes. Such systems have been developed and studied [11, 15, 27], and complete modal decoupling can ideally be achieved [15]. In the passenger car market, the requirement of increased roll stiffness, reduced bounce and pitch stiffness and decoupled modes' stiffnesses in a passive system without using motors, pumps, transducers or computer controllers means that the four-wheel interconnection must be employed.

In the late 1990s, some possible four-wheel interconnection arrangements were presented by Ortiz, each comprising hydraulic circuits combined with mechanical linkages [28]. Figure 3.2 shows one hydraulic prototype of the arrangement. A few years later, Zapletal published a similar approach [29] and Figure 3.3 illustrates the

concept of the suspension. In both studies, only conceptual proposals were employed, without theoretical or experimental investigation.

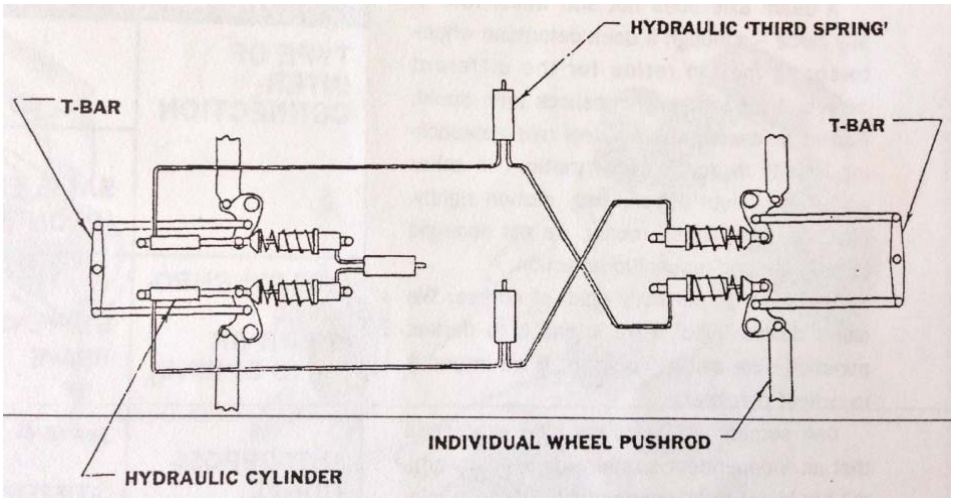

Figure 3.2 Ortiz's Prototype

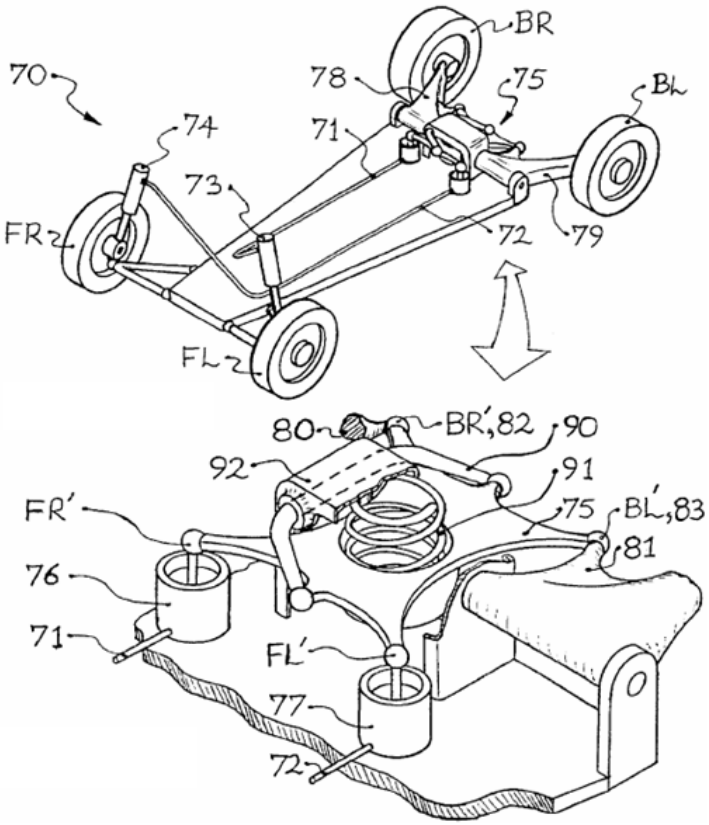

Figure 3.3 Zapletal's Suspension Concept

Following this, Mace demonstrated a theoretical study of existing passive interconnected suspension systems [30], using network theory and system synthesis.

Smith and Walker, almost at the same time, presented their interconnected suspension concept, achieving complete modal decoupling; and they provided possible realisation methods, both mechanical and hydraulic [15]. Although the hydraulic realisation was described in this study, the application of complex components, such as hoses, fittings, accumulators and damper valves, was missing.

In 2006, Mavroudakis and Eberhard published their study of a four-wheel hydraulic interconnection scheme with all modes decoupling [31]. The simulation results showed that the performance of the interconnection arrangement was excellent compared to conventional independent suspensions, but the hydraulic system modelling details were not described. Figure 3.4 illustrates a novel four-wheel interconnection scheme, proposed by Fontdecaba in 2002 [27]. The experimental results showed that the hydraulic implementation had achieved the design goals of the scheme. However, there was no attempt made to develop a theoretical model of the hydrualic prototype.

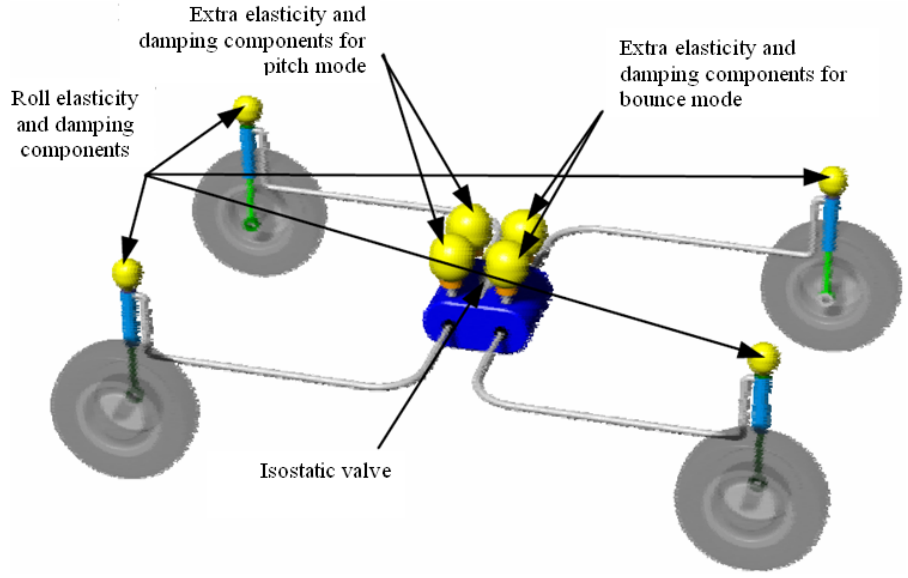

Figure 3.4 Fontdecaba's HIS Scheme

3.1.3 Kinetic HIS systems

Until recently, Wilde *et al.* published the first public-domain study for the applicable hydraulically interconnected suspension system [11]. In this paper, they performed systematic experiments of vehicle handling and compared the results with the performance of a conventional suspension. They concluded that the HIS can provide greater rollover

resistance than the conventional suspension system without significantly sacrificing ride quality.

Most of the literature on interconnected suspensions assumes the ideal interconnecting mechanism and requires time-domain, inefficient, numerical results. Recently, however, Smith [12] investigated the Kinetic H2 suspension in frequency domain. He provided a good understanding of the system and analysed the ride performance of the system. In order to reduce the complexity of the hydraulic circuit model, the pipe FSI was not considered in his research. Nevertheless, this phenomenon cannot be ignored when investigating high-frequency vibrations within the hydraulic system. In this thesis, the FSI of hydraulic piping system is analysed.

3.2 Fluid-Structure Interaction

The interaction between a flexible structure and its internal or surrounding flowing fluid leads to a rich variety of physical phenomena being applied to many fields of engineering. These include: the response of aircraft wings and tall buildings to winds, the vibration of turbine and compressor blades, the flow of liquid through pipes, hoses, tunnels, or arteries, and the oscillation of heat exchangers [32]. It is believed that the FSI is one of the most important issues in modelling and computational studies and the most challenging in terms of multi-physics problems [33]. The literature review in this thesis focuses on the relevant area of this project. As shown in Figure 1.2, the hydraulic circuit is basically a fluid-filled pipe guided system, thus the research about FSI in piping systems will be examined next.

Water-hammer (sometimes referred to as fluid transients) generated by abrupt changes to steady flow in liquid-filled pipe systems [34], is the most important phenomenon in relation to piping systems. The early investigation of FSI in piping systems is an extension of the water-hammer theory [35]. In conventional water-hammer analyses, pipe inertia and axial pipe motion are not taken into account due to the consideration of the rigid pipe assumption [34]. However, pressure waves produce forces that cause the piping systems to move; and the motion, in turn, causes pressure waves. During the fluid transients, pipe systems experience severe dynamic forces. For elastic pipes, dynamic

forces during a water-hammer event induce significant FSI. Therefore, the liquid and piping systems should be treated simultaneously.

When FSI occurs during unsteady flow, the momentum and forces are transferred between piping and the contained liquid. The interaction may be initiated by rapid changes in flow and pressure or the mechanical action of the piping; and it is always made manifest by pipe vibrations and perturbations in the velocity and pressure of the liquid. The interaction of piping can also be transferred to the support mechanisms of the system. [36]

For most piping systems, there are three coupling mechanisms which contribute to dynamic fluid-structure interaction: Poisson coupling, junction coupling, and friction coupling. Poisson coupling represents the relationship between the pressures in the liquid and the axial stresses in the pipe through the radial contraction or expansion of the pipe wall. It is associated with the hoop mode of the pipe [34]. Junction coupling results from the reactions that result from unbalanced pressure forces and changes in liquid momentum at discrete locations in the piping such as in the bends, tees, valves, and orifices [36]. Friction coupling describes the mutual friction between fluid and pipe [34, 37]. In most practical systems, this coupling is insignificant when compared to the other two coupling mechanisms [36-38]. Both Poisson and friction coupling are distributed along the axis of a pipe element, whereas junction coupling acts at specific points in the piping systems [34, 36].

3.3 Modelling

3.3.1 One-dimensional model

With different conditions, the FSI phenomena can be represented in three-dimensional models, two-dimensional models, or one-dimensional models. The three- and two-dimensional models are normally employed to simulate block objects [38, 53] like bridge [40], open shells [41], and aortas [42, 43]. According to previous studies, in the case of the piping system, especially for the very long pipe (the dimension of length is far more than the dimension of diameter), the FSI phenomenon is investigated only in

terms of the liquid-filled pipes and outside constraints [34, 36, 44]. Therefore, the one-dimension model is conventionally applied to demonstrate the FSI of the piping systems.

Pipe elements can be modelled as straight pipes or curved pipes. Zhang et al. use the straight pipe as their research object [45, 46-48], whereas Phillips et al. investigate the curved pipe [49, 50]. The radius of pipe bend is considered in the curve-pipe model, but the models of the two kinds of pipe sections are essentially the same. If we assume that the radius of the curve pipe is infinite and we revise the relevant coefficients of the curve-pipe model, it becomes the straight-pipe model. A detailed explanation is provided in Section 10.1.

The equations indicate that the curve-pipe model cannot represent the pipe elements more precisely than the straight-pipe model. Furthermore, the latter model can provide more flexible ways to simulate piping systems because the curved pipe can be divided into several straight pipe sections that are connected with elbow models. The curve-pipe model can only represents pipes at the two-dimensional plane whereas the straight pipe model can represent pipes at the one-dimensional line, two-dimensional plane or three-dimensional space depending on the different piping setting. These reasons would appear to account for why very few researchers have produced work on the curve-pipe model.

Wiggert, Lavooij and Tijsselling et al. modelled the large piping system by treating each straight pipe section as a pipe reach [34, 36, 37, 51, 44, 52] and combining the pipe reaches with elbows that are considered as internal boundary conditions [38]. Most reported work on FSI in liquid-filled pipes has been concerned with fluid transients and carried out in the time domain. Wiggert and Tijsseling reviewed the majority of the studies in this field [34, 36, 44].

The frequency-domain analysis usually has been deduced by discrete Fourier transforms or Laplace transforms [46]. D'Souza and Oldenburger [53] presented the transforms in their model; and Wilkinson [54] modelled the axial, lateral and torsional vibrations of liquid-filled pipes by the transfer matrices. The Poisson coupling was not included in these models. With the Poisson coupling included, a transfer matrix has been derived by Kuiken [55] to investigate the axial vibration of a straight pipe.

Lesmez [56, 57], Tentarelli [58-61], De Jong [62], Svingen [63], and Li, Yang and Zhang [45, 48] performed the frequency response analysis of pipe systems by applying the TMM to one-dimensional wave theory. Poisson and junction couplings are incorporated in all the theoretical models and the experimental validation is presented. They all adopt the straight pipe section model and describe strong fluid-pipe coupling and axial-lateral-torsional coupling through the use of elbows or curved pipes. The friction coupling and damping influence are considered in some studies [58, 63, 45]. In these models, only structural discontinuities, such as pipe elbows, supports and concentrated masses, are involved. The hydraulic discontinuities like valves, pumps, accumulators, or hoses are not considered.

3.3.2 Models of hydraulic components and circuits

The characteristics of individual hydraulic elements are investigated by Edge and Johnston. The focus of their research is on the resistance coefficients of hydraulic elements such as valves and accumulators [64, 65]. With Tilley they investigated the pressure ripple characteristics of hydraulic circuits before deriving these coefficients [66-68]. The nonlinear mathematical modelling of hydraulic elements is studied by Ionescu [69].

The flexible hose, as an important hydraulic element, is commonly applied in hydraulic systems to reduce assemblage difficulties and mechanical vibrations, which are produced by the FSI at elbows and constrictions. Unlike the studies of rigid pipelines, the modelling of flexible hoses is considerably less documented. However, a more systematic design technique is applied to the hydraulic system where hoses are used because of the increasing knowledge in relation to the dynamics of the flexible hose [70].

Many published works that focus on the investigation of the dynamic behaviour of the fluid-filled hoses come from researchers based at the University of Bath. These researchers have found that the dynamic behaviour of fluid in a hose is affected by the fluid and hose wall properties. In order to reduce pressure fluctuations in a circuit, various models are developed and investigated. A straight hose model is adopted by Longmore [71, 72], Taylor [70], and Johnston [73]. The coupled longitudinal waves in the liquid and hose wall have been described and analysed. Drew et al [74-76] establishes a

model for the hose with tuners in the power steering systems of vehicles by using the impedance matrix.

Unlike the above models, where axial vibrations are only considered, the transmission mechanisms in other directions, namely bending and torsional waves, are considered by Longmore [77, 78] and Tuc [79]. In the earlier study, Longmore and Stammers [80] developed a curved hose model, in which the lateral vibration was combined with the axial vibration mode. Longmore [81, 82] and Johnston [83] presented several methods to obtain the dynamic material properties of flexible hoses that must be used in all types of theoretical models. Through measuring an impedance matrix relating longitudinal waves, the hose properties were derived by Longmore et al. [82]. Johnston and Tim [83] investigated the dynamic properties of Nylon-reinforced hoses and concluded that it has considerably lower bulk moduli and stiffness than steel-reinforced hoses.

There are other studies that concern the dynamic analysis of fluid-filled flexible hoses. Yu and Kojima [84] developed an analytical hose model in the transfer matrix form and determined the static mechanical properties and frequency-dependent mechanical properties of the hose wall by means of the specially designed static expansion method and optimal searching method respectively. Evans and Wilcox [85] presented a model for a specific type of hose that is designed to withstand very high operating pressures. The material properties and the dynamic behaviour of plastic pipes are described and investigated by Prek [86].

There are several studies concerned with the modelling of hydraulic circuits, yet their focus is on the investigation of the entire system as opposed to the hydraulic circuit. Kleinsteuber and Sepehri [87] modelled large-scale hydraulic systems and Cobo et al. [88] investigated the hydraulic system for wheel type loader earth moving equipment. The hydraulic system model in both studies works to simulate the dynamic behaviour of the fluid inside the circuit. Although Rideout and Anderson investigated hydraulic circuits included in the Hydragas Suspension, only very simple hydraulic model were developed as part of the suspension model [19]. The main objective of their research was to study how the suspension influences ride quality.

In 1994, Mrad developed a quarter-car model of a hydraulic active suspension system which includes the pump, accumulator, valves and other hydraulic elements [89]. This is probably the first system model for the hydraulic circuit that combines the models for hydraulic elements with the pure pipe model. Some hydraulic system models are developed for particular applications. Qatu et al. established a system model for vehicle power steering that consists of a pump, hoses, tubes, and a tuned hose [90].

3.4 Methods Used in the Research

3.4.1 Method of analysis

Chaudhry [91] outlines three methods to analyse the steady-oscillatory flows in a hydraulic system: method of characteristics (MOC), impedance method and transfer matrix method (TMM). The MOC is used for analysis in time domain and/or obtaining the general transient response of the systems. The essential idea is to convert the partial differential equations that describe the motion and continuity of unsteady flow into ordinary differential equations [91, 92]. The main advantage of the MOC is to include the nonlinear relationships in the analyses; however a considerable amount of computer time is required for the process. Laooij and Tijsseling [38] combined the MOC with the Finite Element Method (FEM) to solve pipe equations in the time domain.

The TMM is a more efficient procedure in comparison with the FEM due to the streamlined character that is suitable for vector processing computation, although these two numerical methods have different strengths and deficiencies [93]. The impedance method and TMM are used to analyse piping systems in the frequency domain. By using these methods, friction terms and the nonlinear boundary conditions are linearised to deduct solutions. The error introduced by the linearisation can be neglected if the amplitude of oscillations is small. Since the frequency response is directly determined, the required time of computation for the analysis is relatively shorter than that of the MOC.

Rocard [94] introduced the concept of impedance in 1937 and the usage of this method was studied later by Paynter [95], Waller [96], and Wylie [97, 98]. In this method, the terminal impedance is the ratio of the pressure head and the discharge. By using boundary conditions, an impedance diagram between angular frequencies and the determinant

of the terminal impedance is plotted. The resonant frequencies of the system can be obtained at the maximum value of the determinant.

The TMM has been used to analyse structural and mechanical vibrations [99, 100] and to analyse the electrical systems [101]. Chaudhry [102-105] introduced this method to analyse the steady-oscillatory flows and to determine the frequency response of hydraulic systems. It is considered that the TMM is simpler and more systematic than the impedance method [91], especially for analysing systems, in which vibrations of multivariables (e.g. pressure, flow, force, and moment et al.) have to be considered. The literature concerning the application of TMM for pipe systems can be found in the quoted dissertations [56, 58, 62, 63].

3.4.2 Method of implementation

3.4.2.1 MATLAB

In this project, the investigation of liquid-filled pipe-guided hydraulic systems is based on the development of mathematical models and the analysis of system characteristics. All the modelling and analysis processes are implemented by the computational software, MATLAB®.

MATLAB® [106] is a high-level language for technical computing and more than a million engineers and scientists in academia and industry use MATLAB [107]. The computation, visualization, and programming are integrated in an easy-to-use environment, in which problems and solutions are expressed by familiar mathematical notations. The MATLAB system consists of five main parts: desktop tools and the development environment, the MATLAB mathematical function library, the MATLAB language, graphics, and the MATLAB external interfaces/API [106].

The basic data element of MATLAB is an array that does not require dimensioning [106]. This allows many technical computing problems, especially those with matrix and vector formulations, to be solved by writing a programme in a shorter time frame than when using a scalar non-interactive language such as C or FORTRAN. The objec-

tive of this research is to develop and analyse mathematical models that are represented in the form of matrices and vectors.

Many users have contributed to the evolution of MATLAB. The most important feature of MATLAB is probably the toolboxes. These are a family of add-on application-specific solutions [106]. Users can learn and apply specialised technology by comprehensively collecting MATLAB functions (M-files), which extend the MATLAB environment to solve particular kinds of problems.

3.4.2.2 NI LabVIEW

Being employed in the laboratory experiments, the NI LabVIEW collects the input signal and produces output results after an internal dealing process. NI LabVIEW is a system-design software that allows engineers and scientists to create and deploy measurement and control systems through unprecedented hardware integration [108]. It contains a comprehensive set of tools to acquire, analyse, display, and store data, as well as troubleshooting tools. People can solve problems, accelerate productivity, and provide continuous innovation by using this software.

Being called virtual instruments, or VIs, the appearance and operation of NI LabVIEW programs [109] imitate physical instruments, such as oscilloscopes and multimeters. After building a user interface (or front panel) with controls and indicators, codes using VIs and structures are added to control the front panel objects. Controls include knobs, push buttons, dials, and other input mechanisms. Indicators include graphs, LEDs, and other output displays. The code is contained in a block diagram.

NI LabVIEW has been used by millions of engineers and scientists for more than 20 years to develop sophisticated test, measurement, and control applications; and to interface with measurement and control devices [108]. It can be used to communicate with thousands of different hardware devices, such as data acquisition, vision, and motion control devices, as well as GPIB, PXI, VXI, RS232, and RS485 instruments [109]. Time is saved through its comprehensive system design environment, unique graphical programming language, built-in engineering-specific libraries of software functions and hardware interfaces; and data analysis, visualization, and sharing features [108].

The continuous innovation can be realised through a world-class ecosystem of partners and technological alliances, a global and active user community, engineering support, and consistent annual releases [108]. It includes the creation of custom user interfaces for data collection and presentation, the deployment to multiple targets, the integration of multiple programming approaches and so on.

3.5 Relevant Study

3.5.1 Suspension model for analysis of low-frequency vibration

A theoretical model of the hydraulic circuit of Kinetic Suspension System (KSS) is developed by combining individual models of hydraulic elements such as orifices and accumulators and pipe section models [12]. This should be the most relevant study in relation to the present project because the KSS is a typical HIS. In this model, the pipe wall is considered as a rigid body and the analysis of vibration modes focuses on the low-frequency range due to the nature of this study.

The main purpose of this study is to investigate the ride performances and handling effectiveness of a vehicle that is equipped with a KSS. The ride and handling execution depends on the low-frequency vibration modes (below 15 Hz) in the hydraulic circuit of the KSS. In this vibration range, the FSI between the fluid and pipe wall is not significant, thus the FSI is not considered in this hydraulic circuit model and the accuracy of the model is enough to simulate and investigate a seven-freedom half-car model.

However, in order to thoroughly understand the hydraulic circuit and investigate the high-frequency resonance (noise) between the hydraulic circuit and vehicle structures, the FSI between fluid and pipe wall must be considered in the hydraulic model. The pressure or/and flow of fluid is changed by outside stimulation or when it goes through hydraulic components. The changes influence not only the inside liquid but also the outside structures, which include pipe and hose walls as well as supports, masses, elbows etc. Therefore, the pipe is considered as a flexible body rather than a rigid body and the FSI is included in the model.

3.5.2 Methodology

As mentioned in section 3.3.1, the models developed by Lesmez [56, 57], Tentarelli [58-61], De Jong [62], Svingen [63], and Li, Yang and Zhang [45, 48] are applied to analyse the frequency response of the liquid-filled pipe systems. By comparing the mathematical expression, the model described by Lesmez is more flexible to simulate various types of pipe systems, thus this thesis will adopt the flexible theoretical model. However, the consideration of the usual hydraulic components like hoses, valves, and accumulators is not included in all the mentioned studies.

The FSI is very different at the hydraulic level. In the outside structures, the interaction between fluid and structures happens through the pipe wall. At the position of a hydraulic component, the dynamic behaviour of fluid is directly changed by the internal structure of the component. Therefore, the dynamics of hydraulic systems is affected by the properties of hydraulic components. In this thesis, the new models of hydraulic components are developed and the more complex hydraulic circuit model is derived and investigated.

Chapter 4

MATHEMATICAL MODELLING

4.1 Transfer Matrix Method (TMM)

As the series of natural frequencies and modal shapes of the piping system are the key characteristics for investigating the vehicle noise problems produced by pressure changes of the hydraulic circuit, the analyses of the system dynamics focuses on the frequency domain. The system principally consists of pipeline and joint points, through which it can be conveniently regarded as an assemblage of a few simpler substructures [93]. For such cases the algorithm is produced by the chaining of matrix operations and the mathematical model of the system is established by applying TMM.

The basic idea of TMM [93] is to break up a complicated structural system into component parts with simple elastic and dynamic properties that can be readily expressed in a matrix form. These component matrices are considered as movable finite blocks that can be fitted together according to a set of predetermined rules. Different systems are represented by different combination, which express the static and dynamic, and the linear as well as nonlinear properties of the entire system. For a complex numerical analysis of systems, the TMM may be regarded as an effective tool.

According to Tesar and Fillo [93], systems are basically divided into four typical matrix expressions by applying TMM: transfer matrix, nodal matrix, matrix of initial parameters, and matrix of boundary conditions. In this dissertation, the transfer matrix is called the field matrix, and the two latter matrices are both considered as boundary conditions. The method allows that a state vector of variables at one location in the system is related to the state vector at another location by transfer matrices that consist of transfer equations [92].

The state vectors are transferred over the multitude of elements or substructures in the assumed simulation. The field matrix allows the transfer of a state vector from initial to

the end points of an arbitrary element; and the nodal matrix transfers a state vector over nodal points coupling together adjacent elements to form the whole structure. During the coupling process, certain geometric compatibility conditions are satisfied at each point as an internal boundary between two adjacent substructures. The boundary conditions are defined by the matrices of initial and end parameters. [93]

The algorithm of the TMM is to apply matrix multiplications of field and nodal matrices. With the boundary conditions, a set of algebraic equations for determination are defined. The eigenvalue problem can be solved by setting the determinant of the equations equal to zero; after substituting eigenvalues into the original matrices, the eigenvectors are then deducted. For most practical problems that are modelled by TMM, the focus is on finding out and/or analyses of eigenvalues and eigenvectors.

The principal advantages of the TMM are listed below [93]:

1. For the updated complex simulations in arbitrary linear and nonlinear regions, the TMM models the static and dynamic behaviour in a simple way.
2. For various intermediate and total boundary conditions, the TMM offers the capability of dynamic modelling to deal with the variable situations during the deformation process.
3. For statically determinate structures, the TMM allows for using the same algorithm of the line solution to analyse highly redundant systems.
4. Owing to the reduced amount of algebraic equations needed to be solved, another advantage of the TMM is the small demands that it places on computer time and storage.

A disadvantage of this method is the occasional numerical instability of computer calculations, especially in the advanced nonlinear regions of complex simulations. The chain structure of the calculation operations can lead to the accumulation of tolerance and this needs to be carefully controlled, especially for large scale systems.

4.2 Introduction of the System

As shown in Figure 1.2, the system studied in this project is a liquid-filled pipe-guided hydraulic circuit. The basic structure of the system is a piping system and the valves,

accumulators, inertial mass, outside constraints etc. can be considered as joint points. The mathematical representation of this kind of system can be simplified as a one-dimensional model due to the significant difference of dimensions between the longitudinal direction and the two latitudinal directions.

The inside pressure changes produce liquid hammers that hit the pipe wall and cause vibrations. This thesis will study the fluid-induced vibrations in hydraulic circuits, which are mainly due to the impact of pressure ripples on the pipe wall, especially at pipe junctions (e.g. the bend or elbow areas). Here, the pipe wall is considered as a flexible body rather than a rigid body, i.e. the FSI must be included in the developed pipe model. The same condition is also applied to hoses.

The joint points are represented as hydraulic discontinuities and structural discontinuities. The pressure and/or flow of fluid can be changed when going through the hydraulic discontinuities. In addition, the fluidic changes perform effects on the structural discontinuities. Therefore, the phenomenon of FSI is presented at joint points. In order to decrease the complexity of the modelling process, the discontinuities are assumed as non-dimensional points, thus the structure of every point is regarded as a rigid body object. All element models are combined by applying TMM to demonstrate the FSI of the whole system.

4.3 Steel Pipe Modelling

4.3.1 Governing equations

The pipe element analysed in this study is liquid-filled, slender, straight, prismatic, and it has a circular cross-section. It is assumed that the inside liquid and pipe-wall material are linearly elastic and friction free. The phenomenon of cavitation will not occur because of high initial pressure in the hydraulic circuit. The theory developed is valid for the low-frequency acoustic behaviour of the pipe section. This means that the ratios of fluid velocity to wave speed, pipe wall thickness to inner radius of pipe section, inner diameter of pipe section to wavelength, and liquid pressure to fluid bulk modulus are small with respect to unity [36]. Axial, transverse and torsional vibrations are assumed not to influence each other along the straight pipe section.

For the most extensive utilised pipe model, the one-dimensional straight-pipe model, the entire model includes fourteen partial differential equations, known as Equation 4.1, 4.2, 4.3, and 4.4 [36], which are presented by a number of researchers in their published works [36, 56, 57, 63]. These researchers describe the axial (longitudinal), lateral (latitudinal) and torsional vibrations of a single liquid-filled pipe. The equations of longitudinal and torsional directions are the same within all the published works. However, the expressions of latitudinal directions in these studies display slight differences in terms of signals.

$$\begin{cases} \dfrac{\partial p}{\partial z} + \rho_f \dfrac{\partial^2 v}{\partial t^2} = 0 \\ \dfrac{\partial f_z}{\partial z} - \rho_p A_p \dfrac{\partial^2 u_z}{\partial t^2} = 0 \\ \dfrac{f_z}{EA_p} - \dfrac{r\nu}{e_p E} p - \dfrac{\partial u_z}{\partial z} = 0 \\ \dfrac{p}{K^*} - 2\nu \dfrac{\partial u_z}{\partial z} + \dfrac{\partial v}{\partial z} = 0 \end{cases} \quad \text{(Equation 4.1)}$$

$$\begin{cases} \dfrac{f_x}{\kappa_p G_p A_p} + \dfrac{\partial u_x}{\partial z} + \theta_y = 0 \\ m_y + \eta_p E I_p \dfrac{\partial \theta_y}{\partial z} = 0 \\ \dfrac{\partial f_x}{\partial z} + \left(\rho_p A_p + \rho_f A_f\right) \dfrac{\partial^2 u_x}{\partial t^2} = 0 \\ \dfrac{\partial m_y}{\partial z} + \left(\rho_p I_p + \rho_f I_f\right) \dfrac{\partial^2 \theta_y}{\partial t^2} - f_x = 0 \end{cases} \quad \text{(Equation 4.2)}$$

$$\begin{cases} \dfrac{f_y}{\kappa_p G_p A_p} + \dfrac{\partial u_y}{\partial z} + \theta_x = 0 \\ m_x + \eta_p E I_p \dfrac{\partial \theta_x}{\partial z} = 0 \\ \dfrac{\partial f_y}{\partial z} + \left(\rho_p A_p + \rho_f A_f\right) \dfrac{\partial^2 u_y}{\partial t^2} = 0 \\ \dfrac{\partial m_x}{\partial z} + \left(\rho_p I_p + \rho_f I_f\right) \dfrac{\partial^2 \theta_x}{\partial t^2} - f_y = 0 \end{cases} \quad \text{(Equation 4.3)}$$

$$\begin{cases} \dfrac{\partial m_z}{\partial z} - \rho_p J_p \dfrac{\partial^2 \theta_z}{\partial t^2} = 0 \\ m_z - G_p J_p \dfrac{\partial \theta_z}{\partial z} = 0 \end{cases} \quad \text{(Equation 4.4)}$$

where

f_x lateral shear force of wall on x axis

f_y lateral shear force of wall on y axis

f_z axial force of wall

m_x bending moment to x axis

m_y bending moment to y axis

m_z bending moment to z axis

u_x lateral displacement of wall on x axis

u_y lateral displacement of wall on y axis

u_z axial displacement of wall

θ_x rotate angle to x axis

θ_y rotate angle to y axis

θ_z rotate angle to z axis

p fluid pressure

v axial displacement of fluid

A_f cross-sectional area of fluid in pipe (m^2)

A_p cross-sectional area of pipe wall (m^2)

e_p thickness of pipe wall (m)

E Young's modulus of pipe wall (Pa)

G_p shear modulus of pipe wall (Pa)

I_f area moment of inertia of fluid in pipe (m^4)

I_p area moment of inertia of pipe wall (m^4)

J_p polar moment of inertia of pipe wall (m^4)

K^* modified fluid bulk modulus of pipe element (Pa)

r inner radius of pipe wall (m)

η_p rigidity factor for stiffness of elbow of pipe

κ_p shear coefficient for hollow circle cross section of pipe

ν Poisson's ratio of pipe wall

ρ_f mass density of fluid(kg/m^3)

ρ_p mass density of pipe wall (kg/m^3)

t time; x, y, z coordinates

In the governing equations, there are three coefficients that influence the pipe dynamics: the modified fluid bulk modulus K^*, the shear coefficient κ and the rigidity factor η. The

values of the coefficients depend strongly upon the size and shape of the pipe. When the ratio of pipe wall thickness to the inner radius is small with respect to unity, the pipe can be considered as a thin-wall pipe.

According to Tijsseling [51], the modified fluid bulk modulus is defined as:

$$\frac{1}{K^*} = \frac{1}{K} + \frac{2}{E}\left(\frac{r}{e_p} + \frac{1 + e_p / r}{2 + e_p / r} + \nu \right)$$

Thus, this modulus for the thin-wall pipe is [36]: $\frac{1}{K^*} = \frac{1}{K} + \frac{2r}{e_p E}\left(1 - \nu^2\right)$

The shear coefficient for different shapes of cross sections is different. The Timoshenko's beam theory defines the coefficient of the hollow circular cross section as [110]:

$$\kappa_p = \frac{6(1+\nu)(1+m^2)^2}{(7+6\nu)(1+m^2)^2 + 4(5+3\nu)m^2} \qquad \text{where} \qquad m = \frac{r}{r + e_p}$$

For the thin-walled pipe, the m approximately equals one because the inner radius is almost equal to the outer radius. The κ_p can be expressed as: $\kappa_p = \frac{2(1+\nu)}{4+3\nu}$

Notably, the curved pipe is more flexible than expected due to a deformation of the pipe cross section [111]. By considering this influence, the flexural stiffness (EI_p) for a curved pipe is modified as $\eta_\mathrm{p} EI_\mathrm{p}$, in which the η is $\eta_p = \frac{1 + 12(e_p R / \bar{r}^2)^2}{10 + 12(e_p R / \bar{r}^2)^2}$.

where

$\bar{r}$ mean radius of pipe wall (m)

R radius of curvature of pipe bend (m)

For the straight pipe section, the η is equal to one.

4.3.1.1 Equations of latitudinal motions

There are two planes of latitudinal vibrations in this model: one is the *x-z* plane, the other is the *y-z* plane. Wiggert and Tijsseling [36] and Cowper [110] present their equations of the *x-z* plane and the *y-z* plane in the same form, but the expressions of the two papers are different. The equations developed by Lesmez [56, 57] display different

forms for the two planes. In this thesis, the differential equations will be transformed from the time domain to the frequency domain, and matrices including frequency properties will be produced. The different signs will induce different results during the process of this transformation.

The Timoshenko beam theory is applied to derive the equations of the two lateral motions. In order to find out the proper expression of the lateral motions, one of Timoshenko's books [112] is utilised as a reference. In this section, the transverse vibrations, rotary inertia and shearing deformations of prismatic beams are investigated and the equations are derived. Figure 4.1 illustrates the free body diagram of the transverse vibrations of a beam on two planes of latitudinal directions.

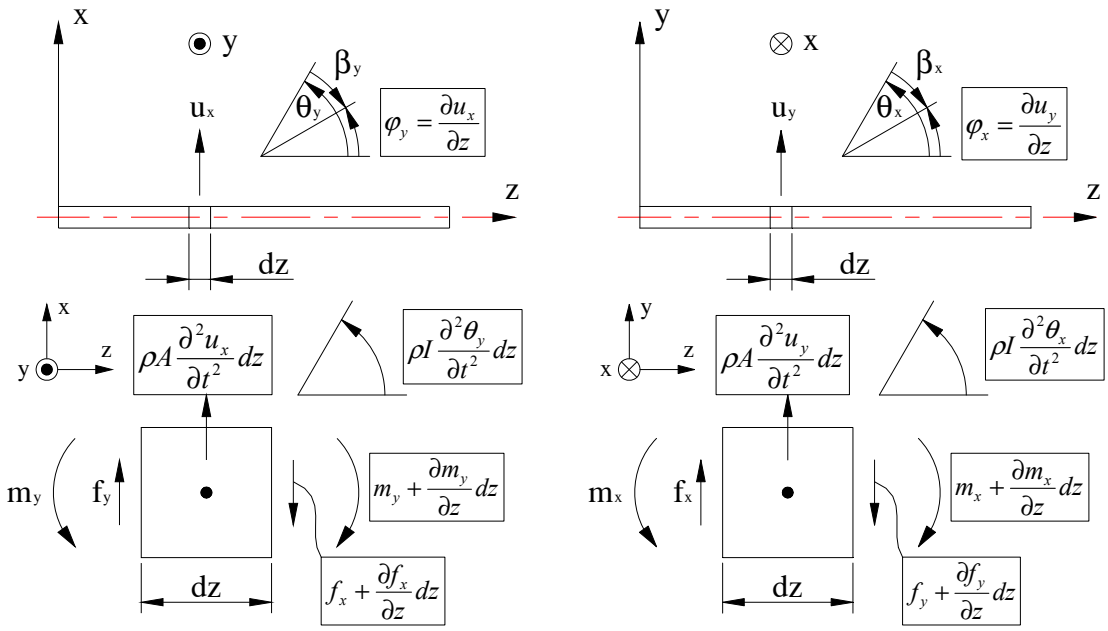

4.1a Diagram of *x*-*z* plane 4.1b Diagram of *y*-*z* plane

Figure 4.1 Free Body Diagram of Transverse Vibration

For a harmonic vibration, the direction of the displacement is opposite to the direction of the acceleration and the outside force. If we assume that the transverse displacements (u_x and u_y) are in a positive direction, the directions of the shearing forces (f_x and f_y terms) are decided as shown in Figure 4.1. From the definition of inertial forces, the direction of inertial forces is opposite to the direction of the accelerations. Therefore, the direction of the inertial forces (ρAdz terms) is also determined. Under these conditions, the dynamic equilibrium condition of forces in the vertical direction (x or y) is:

$$\begin{cases} f_x + \rho A \dfrac{\partial^2 u_x}{\partial t^2} dz - f_x - \dfrac{\partial f_x}{\partial z} dz = 0 \\ f_y + \rho A \dfrac{\partial^2 u_y}{\partial t^2} dz - f_y - \dfrac{\partial f_y}{\partial z} dz = 0 \end{cases} \Rightarrow \begin{cases} \dfrac{\partial f_x}{\partial z} - \rho A \dfrac{\partial^2 u_x}{\partial t^2} = 0 \\ \dfrac{\partial f_y}{\partial z} - \rho A \dfrac{\partial^2 u_y}{\partial t^2} = 0 \end{cases}$$

The rotation angles (φ_x and φ_y terms) depend not only on the rotation of the cross section of the beam but also on the shearing deformations. When the influence of the shearing force is removed, let θ denote the slope of the deflection curve (produced only by the moment). And use β to indicate the angle of shear at the neutral axis in the same cross section, which is caused by the shearing force. Thus, the direction of slope (β_x and β_y) is the same as the moment produced by forces (f_x and f_y terms).

Assuming the angles of rotation (φ_x and φ_y) are in an anticlockwise direction, the directions of angular displacements (θ_x and θ_y) are decided (Figure 4.1). Considering the harmonic vibration, the direction of angular displacement (θ_x and θ_y) is opposite to the direction of the angular accelerations. In addition, the sum of bending moments (m_x and m_y terms), and the direction of the inertial moments (ρIdz terms) is opposite to the direction of the accelerations. The direction of moments is therefore decided. According to Figure 4.1, the total slope is:

$$\begin{cases} \varphi_y = \dfrac{\partial u_x}{\partial z} = \theta_y - \beta_y \\ -\varphi_x = -\dfrac{\partial u_y}{\partial z} = -\theta_x + \beta_x \end{cases} \Rightarrow \begin{cases} \beta_y = \theta_y - \dfrac{\partial u_x}{\partial z} \\ \beta_x = \theta_x - \dfrac{\partial u_y}{\partial z} \end{cases} \qquad \text{(Equation 4.5)}$$

The dynamic equilibrium condition for moments about an axis (y or x) through its centre of mass and perpendicular position to the plane (x-z or y-z) is:

$$\begin{cases} m_y - m_y - \dfrac{\partial m_y}{\partial z} dz - f_x dz - df_x dz + \rho I \dfrac{\partial^2 \theta_y}{\partial t^2} dz = 0 \\ m_x + \dfrac{\partial m_x}{\partial z} dz - m_x + f_y dz + df_y dz - \rho I \dfrac{\partial^2 \theta_y}{\partial t^2} dz = 0 \end{cases} \Rightarrow \begin{cases} \dfrac{\partial m_y}{\partial z} - \rho I \dfrac{\partial^2 \theta_y}{\partial t^2} + f_x \approx 0 \\ \dfrac{\partial m_x}{\partial z} - \rho I \dfrac{\partial^2 \theta_x}{\partial t^2} + f_y \approx 0 \end{cases}$$

From elementary flexure theory, the bending moment and the shearing force are:

$$\begin{cases} m_y - EI\dfrac{\partial \theta_y}{\partial z} = 0 \\ m_x - EI\dfrac{\partial \theta_x}{\partial z} = 0 \end{cases} \quad \& \quad \begin{cases} f_x = \kappa GA\beta_y \\ f_y = \kappa GA\beta_x \end{cases}$$

By substituting the Equation 4.5 for the two β, the shearing force will be:

$$\begin{cases} f_x = \kappa GA\beta_y \\ f_y = \kappa GA\beta_x \end{cases} \Rightarrow \begin{cases} f_x = \kappa GA\left(\theta_y - \dfrac{\partial u_x}{\partial z}\right) \\ f_y = \kappa GA\left(\theta_x - \dfrac{\partial u_y}{\partial z}\right) \end{cases} \Rightarrow \begin{cases} \dfrac{f_x}{\kappa GA} + \dfrac{\partial u_x}{\partial z} - \theta_y = 0 \\ \dfrac{f_y}{\kappa GA} + \dfrac{\partial u_y}{\partial z} - \theta_x = 0 \end{cases}$$

Therefore, the equations of transverse motions are:

$$\begin{cases} \dfrac{\partial f_x}{\partial z} - \left(\rho_p A_p + \rho_f A_f\right)\dfrac{\partial^2 u_x}{\partial t^2} = 0 \\ \dfrac{\partial m_y}{\partial z} - \left(\rho_p I_p + \rho_f I_f\right)\dfrac{\partial^2 \theta_y}{\partial t^2} + f_x = 0 \\ m_y - \eta_p EI_p \dfrac{\partial \theta_y}{\partial z} = 0 \\ \dfrac{f_x}{\kappa_p G_p A_p} + \dfrac{\partial u_x}{\partial z} - \theta_y = 0 \end{cases} \quad \text{(Equation 4.6)}$$

$$\begin{cases} \dfrac{\partial f_y}{\partial z} - \left(\rho_p A_p + \rho_f A_f\right)\dfrac{\partial^2 u_y}{\partial t^2} = 0 \\ \dfrac{\partial m_x}{\partial z} - \left(\rho_p I_p + \rho_f I_f\right)\dfrac{\partial^2 \theta_x}{\partial t^2} + f_y = 0 \\ m_x - \eta_p EI_p \dfrac{\partial \theta_x}{\partial z} = 0 \\ \dfrac{f_y}{\kappa_p G_p A_p} + \dfrac{\partial u_y}{\partial z} - \theta_x = 0 \end{cases} \quad \text{(Equation 4.7)}$$

It can be seen that the formats of the two groups of equations are the same.

4.3.1.2 Friction and damping consideration

The vibration of a straight liquid-filled pipe section is demonstrated by the 14-equation model on the axial, two planes of lateral, and torsional directions. In this model, the friction and damping influence have not been considered. The coefficients of friction coupling and the structural viscous damping could be included by adding some terms into the equations of the axial direction [46], shown as Equation 4.8. These equations can be

expressed in the matrix form (Equation 4.9). For this thesis, the flow inside the pipeline results from the movement of the piston of the cylinder, being modelled as laminar flow. In this case, **C** is a constant matrix [45].

$$\begin{cases} \dfrac{\partial \dot{v}}{\partial t} + \dfrac{1}{\rho_f}\dfrac{\partial p}{\partial z} + n_f \dot{v} - n_f \dot{u}_z = 0 \\ \left[\dfrac{1}{K} + (1-\nu^2)\dfrac{2r}{Ee_p}\right]\dfrac{\partial p}{\partial t} + \dfrac{\partial \dot{v}}{\partial z} - 2\nu\dfrac{\partial \dot{u}_z}{\partial z} = 0 \\ \dfrac{\partial \dot{u}_z}{\partial t} - \dfrac{1}{\rho_p A_p}\dfrac{\partial f_z}{\partial z} - n_p \dot{v} + \left(n_p + D_p\right)\dot{u}_z = 0 \\ \dfrac{r\nu}{e_p E}\dfrac{\partial p}{\partial t} - \dfrac{1}{EA_p}\dfrac{\partial f_z}{\partial t} + \dfrac{\partial \dot{u}_z}{\partial z} = 0 \end{cases} \qquad \text{(Equation 4.8)}$$

where

D_p damping coefficient per unit length of pipe (s^{-1})

n_f fluid friction coefficient (s^{-1})

n_p structural damping coefficient of pipe (s^{-1})

$$\mathbf{A}\frac{\partial \boldsymbol{\varphi}(z,t)}{\partial t} + \mathbf{B}\frac{\partial \boldsymbol{\varphi}(z,t)}{\partial z} + \mathbf{C}\boldsymbol{\varphi}(z,t) = \mathbf{0} \qquad \text{(Equation 4.9)}$$

where $\boldsymbol{\varphi} = \begin{pmatrix} \dot{v} \\ p \\ \dot{u}_z \\ f_z \end{pmatrix}$ $\mathbf{A} = \begin{pmatrix} 1 & 0 & 0 & 0 \\ 0 & \dfrac{1}{K^*} & 0 & 0 \\ 0 & 0 & 1 & 0 \\ 0 & \dfrac{r\nu}{e_p E} & 0 & -\dfrac{1}{EA_p} \end{pmatrix}$ $\dfrac{1}{K^*} = \dfrac{1}{K} + (1-\nu^2)\dfrac{2r}{Ee_p}$

$$\mathbf{B} = \begin{pmatrix} 0 & \dfrac{1}{\rho_f} & 0 & 0 \\ 1 & 0 & -2\nu & 0 \\ 0 & 0 & 0 & -\dfrac{1}{\rho_p A_p} \\ 0 & 0 & 1 & 0 \end{pmatrix} \qquad \mathbf{C} = \begin{pmatrix} n_f & 0 & -n_f & 0 \\ 0 & 0 & 0 & 0 \\ -n_p & 0 & n_p + D_p & 0 \\ 0 & 0 & 0 & 0 \end{pmatrix}$$

The criteria of defining the fluid friction coefficient (n_f) and structural damping coefficient (n_p) is also presented in this paper. It is noted that for thin-walled circular pipes, the relationship between the coefficients n_p and n_f is $n_p = \dfrac{R\rho_f}{2e_p\rho_p} n_f$ [46]. For the lateral

and torsional directions, the hysteretic damping is introduced in the analysis by applying a complex-valued modulus of elasticity [113].

Johnston [68] defines the frequency-dependent friction in laminar pipe flow as a term $\dot{v}A_f \frac{\partial \dot{v}}{\partial z}$. However, when the fluid velocity is much smaller than the speed of sound in fluid, usually this term is ignored. For the HIS system, the fluid fluctuation is produced by the relative movement between wheels and the vehicle body. The velocity of fluid is considerably smaller compared to the sound speed in fluid. Therefore, this friction is not included in the model.

4.3.2 Derivation of field transfer matrix

To apply the TMM, the transfer matrices of every kind of element are needed to be derived first. The field matrix of the pipe element can be obtained by transforming the partial differential equations described in Section 4.3.1 from the time domain to the frequency domain. Lesmez [56] described the transforming process of the governing equations, but the friction and damping impact are not considered in his study. The equations are divided into four groups: axial direction equations describe the longitude vibration modes of the piping system; y-z and x-z lateral direction equations express the radial vibration modes; and torsional direction equations show the torsional vibration around the central axis of the pipe.

Basically, there is no coupling between different directions, thus the transforming process can be derived separately for each direction. Since the friction and damping influence is shown on the axial direction, the revised axial equations are adopted and the new transfer field matrix is derived in this thesis. Equation 4.8 can be displayed as:

$$\begin{cases} \frac{1}{\rho_f}\frac{\partial p}{\partial z} + \frac{\partial^2 v}{\partial t^2} + c_f = 0 \\ \frac{1}{\rho_p A_p}\frac{\partial f_z}{\partial z} - \frac{\partial^2 u_z}{\partial t^2} + c_p = 0 \\ f_z - \frac{A_p r \nu}{e_p} p - EA_p \frac{\partial u_z}{\partial z} = 0 \\ p - 2\nu K^* \frac{\partial u_z}{\partial z} + K^* \frac{\partial v}{\partial z} = 0 \end{cases} \quad \text{where} \quad \begin{cases} c_f = n_f \dot{v} - n_f \dot{u}_z \\ \frac{1}{K^*} = \frac{1}{K} + (1-\nu^2)\frac{2r}{Ee_p} \\ c_p = n_p \dot{v} - (n_p + D_p)\dot{u}_z \end{cases} \qquad \text{(Equation 4.10)}$$

From Equation 4.10, Equation 4.11 and Equation 4.12 are obtained.

$$\begin{cases} \frac{1}{\rho_f}\frac{\partial^2 p}{\partial z^2}+\frac{\partial^3 v}{\partial z\partial t^2}+\frac{\partial c_f}{\partial z}=0 \\ \frac{1}{\rho_p A_p}\frac{\partial^2 f_z}{\partial z^2}-\frac{\partial^3 u_z}{\partial z\partial t^2}+\frac{\partial c_p}{\partial z}=0 \end{cases} \quad \text{(Equation 4.11)}$$

Eq. 4.10 =>

$$\begin{cases} \frac{\partial^2 f_z}{\partial t^2}-\frac{A_p r\nu}{e_p}\frac{\partial^2 p}{\partial t^2}-EA_p\frac{\partial^3 u_z}{\partial z\partial t^2}=0 \\ \frac{\partial^2 p}{\partial t^2}-2\nu K^*\frac{\partial^3 u_z}{\partial z\partial t^2}+K^*\frac{\partial^3 v}{\partial z\partial t^2}=0 \end{cases} \quad \text{(Equation 4.12)}$$

Eq. 4.11 => $$\begin{cases} \frac{\partial^3 v}{\partial z\partial t^2}=-\frac{1}{\rho_f}\frac{\partial^2 p}{\partial z^2}-\frac{\partial c_f}{\partial z} \\ \frac{\partial^3 u_z}{\partial z\partial t^2}=\frac{1}{\rho_p A_p}\frac{\partial^2 f_z}{\partial z^2}+\frac{\partial c_p}{\partial z} \end{cases} \quad \text{(Equation 4.13)}$$

Substitute Equation 4.13 for the third derivative of Equation 4.12, then:

Eq. 4.12 => $$\begin{cases} \frac{E}{\rho_p}\frac{\partial^2 f_z}{\partial z^2}-\frac{\partial^2 f_z}{\partial t^2}+\frac{A_p r\nu}{e_p}\frac{\partial^2 p}{\partial t^2}+EA_p\frac{\partial c_p}{\partial z}=0 \\ \frac{2\nu K^*}{\rho_p A_p}\frac{\partial^2 f_z}{\partial z^2}+\frac{K^*}{\rho_f}\frac{\partial^2 p}{\partial z^2}-\frac{\partial^2 p}{\partial t^2}+2\nu K^*\frac{\partial c_p}{\partial z}+K^*\frac{\partial c_f}{\partial z}=0 \end{cases} \quad \text{(Equation 4.14)}$$

As any vibration can be divided into harmonic waves, the assumption of the variables can be represented as Equation 4.15. Like Galerkin's Method, the time factor and position factor are separated by this way.

$$\begin{cases} u_z(z,t)=U_z(z)e^{j\omega t};\quad p(z,t)=P(z)e^{j\omega t};\quad v(z,t)=V(z)e^{j\omega t};\quad f_z(z,t)=F_z(z)e^{j\omega t} \\ u_x(z,t)=U_x(z)e^{j\omega t};\ \theta_y(z,t)=\Theta_y(z)e^{j\omega t};\ m_y(z,t)=M_y(z)e^{j\omega t};\ f_x(z,t)=F_x(z)e^{j\omega t} \\ u_y(z,t)=U_y(z)e^{j\omega t};\ \theta_x(z,t)=\Theta_x(z)e^{j\omega t};\ m_x(z,t)=M_x(z)e^{j\omega t};\ f_y(z,t)=F_y(z)e^{j\omega t} \\ \theta_z(z,t)=\Theta_z(z)e^{j\omega t};\ m_z(z,t)=M_z(z)e^{j\omega t};\ c_f(z,t)=C_f(z)e^{j\omega t};\ c_p(z,t)=C_p(z)e^{j\omega t} \end{cases} \quad \text{(Eq. 4.15)}$$

where

F_x lateral shear force amplitude of wall on x axis

F_y lateral shear force amplitude of wall on y axis

F_z axial force amplitude of wall

M_x bending moment amplitude to x axis

M_y bending moment amplitude to y axis

M_z bending moment amplitude to z axis

U_x lateral displacement amplitude of wall on x axis

U_y lateral displacement amplitude of wall on y axis

U_z axial displacement amplitude of wall

Θ_x rotate angle amplitude to x axis

Θ_y rotate angle amplitude to y axis

Θ_z rotate angle amplitude to z axis

P fluid pressure amplitude

V axial displacement amplitude of fluid

j imaginary unit

ω angular frequency

Substitute the above expression for the relevant terms of Equation 4.14, then:

$$\frac{E}{\rho_p}F_z''(z)+\omega^2 F_z(z)-\omega^2\frac{A_p r\nu}{e_p}P(z)+EA_pC_p(z)=0 \qquad \text{(Equation 4.16)}$$

Eq. 4.14 =>

$$\frac{2\nu K^*}{\rho_p A_p}F_z''(z)+\frac{K^*}{\rho_f}P''(z)+\omega^2 P(z)+2\nu K^* C_p(z)+K^* C_f(z)=0 \text{ (Equation 4.17)}$$

Eq. 4.16 =>
$$\begin{cases} \omega^2 P(z)=\dfrac{e_p E}{\rho_p A_p r\nu}F_z''(z)+\omega^2\dfrac{e_p}{A_p r\nu}F_z(z)+\dfrac{e_p E}{r\nu}C_p(z) \\ P''(z)=\dfrac{1}{\omega^2}\dfrac{e_p E}{\rho_p A_p r\nu}F_z^{iv}(z)+\dfrac{e_p}{A_p r\nu}F_z''(z)+\dfrac{1}{\omega^2}\dfrac{e_p E}{r\nu}C_p(z) \end{cases} \qquad \text{(Equation 4.18)}$$

Substitute Equation 4.18 for the relevant terms of Equation 4.17, then Equation 4.19 can be derived as:

$$F_z^{iv}(z)+\omega^2\left(\frac{2\rho_f r\nu^2}{e_p E}+\frac{\rho_p}{E}+\frac{\rho_f}{K^*}\right)F_z''(z)+\omega^4\frac{\rho_f}{K^*}\frac{\rho_p}{E}F_z(z)+\omega^2\frac{\rho_f}{K^*}\rho_p A_p C_p(z)$$
$$+\omega^2\frac{2\rho_f r\nu^2}{e_p E}\rho_p A_p C_p(z)+\omega^2\frac{2\rho_f r\nu^2}{e_p E}\frac{\rho_p A_p}{2\nu}C_f(z)+\rho_p A_p C_p(z)=0 \qquad \text{(Equation 4.19)}$$

If we assume $\begin{cases} \gamma = \dfrac{2\rho_f r \nu^2}{e_p E}\omega^2 l^2 \\ \sigma = \dfrac{\rho_p}{E}\omega^2 l^2 \\ \tau = \dfrac{\rho_f}{K^*}\omega^2 l^2 \end{cases}$, then Equation 4.19 can be expressed as:

$$F_z^{iv} + \frac{\gamma+\sigma+\tau}{l^2}F_z'' + \frac{\tau\sigma}{l^4}F_z + \frac{\rho_p A_p}{l^2}\left(C_p\tau + C_p\gamma + \frac{\gamma}{2\nu}C_f\right) + \rho_p A_p C_p = 0 \quad \text{(Equation 4.20)}$$

where l length of section (m)

Let $F_z(z) = \overline{A}e^{\lambda'\frac{z}{l}}$, then $F_z = \overline{A}e^{\frac{\lambda'}{l}z} \Rightarrow \begin{cases} F_z^{iv} = \left(\dfrac{\lambda'}{l}\right)^4 \overline{A}e^{\frac{\lambda'}{l}z} \\ F_z'' = \left(\dfrac{\lambda'}{l}\right)^2 \overline{A}e^{\frac{\lambda'}{l}z} \end{cases}$ (Equation 4.21)

Substitute Equation 4.21 for the relevant terms of Equation 4.20, then:

Eq. 4.20 => $\lambda'^4 + (\tau+\sigma+\gamma)\lambda'^2 + \tau\sigma + C'(\lambda') = 0$ (Equation 4.22)

where $C'(\lambda') = \dfrac{1}{\overline{A}e^{\frac{\lambda'}{l}z}} l^2 \rho_p A_p C_p \left(\tau + \gamma + \dfrac{\gamma}{2\nu}\dfrac{C_f}{C_p} + l^2\right)$

The term $C'(\lambda)$ is the coefficient of friction coupling and the structural viscous damping, whose value is dependent on the system frequency and the length of the pipe section. From the expression, it can be concluded that this coefficient is decreased with the increase in the system frequency and/or decrease with the pipe length. In order to reduce the complexity of the derived process, the coefficient term is simplified as a constant *C''*. The value of can be obtained from engineering experiences. Then the Equation 4.22 is displayed as:

$$\lambda'^4 + (\tau+\sigma+\gamma)\lambda'^2 + \tau\sigma + C'' = 0 \quad \text{(Equation 4.23)}$$

For a quadratic equation "$ax^2 + bx + c = 0$", the solutions are $x_1 = \dfrac{-b+\sqrt{b^2-4ac}}{2a}$ and $x_2 = \dfrac{-b-\sqrt{b^2-4ac}}{2a}$. Therefore, the solutions of Equation 4.23 are:

$$\begin{cases} \lambda'^2_{1,2} = -\dfrac{1}{2}\left[(\tau+\sigma+\gamma) \mp \sqrt{(\tau+\sigma+\gamma)^2 - 4(\tau\sigma + C'')}\right] \\ \lambda'_1 = \pm j\sqrt{\dfrac{1}{2}\left[(\tau+\sigma+\gamma) - \sqrt{(\tau+\sigma+\gamma)^2 - 4(\tau\sigma + C'')}\right]} \\ \lambda'_2 = \pm j\sqrt{\dfrac{1}{2}\left[(\tau+\sigma+\gamma) + \sqrt{(\tau+\sigma+\gamma)^2 - 4(\tau\sigma + C'')}\right]} \end{cases}$$

Since the value of "$\tau + \sigma + \gamma$" is larger than the value of "$\sqrt{(\tau+\sigma+\gamma)^2 - 4(\tau\sigma + C'')}$", $\lambda'^2_{1,2}$ are negative values; and the λ' include frequency and pipe length factors. From the equation $F_z(z) = \overline{A} e^{\lambda' \frac{z}{l}}$, it can be concluded the Equation 4.24, in which the "λ_{12}" is expressed as Equation 4.25.

$$F_z(z) = \overline{A}_1 e^{j\lambda_1 \frac{z}{L}} + \overline{A}_2 e^{-j\lambda_1 \frac{z}{L}} + \overline{A}_3 e^{j\lambda_2 \frac{z}{L}} + \overline{A}_4 e^{-j\lambda_2 \frac{z}{L}} \qquad \text{(Equation 4.24)}$$

$$\begin{cases} \lambda^2_{1,2} = \dfrac{1}{2}\left[(\tau+\sigma+\gamma) \mp \sqrt{(\tau+\sigma+\gamma)^2 - 4(\tau\sigma + C'')}\right] \\ \lambda_1 = \sqrt{\dfrac{1}{2}\left[(\tau+\sigma+\gamma) - \sqrt{(\tau+\sigma+\gamma)^2 - 4(\tau\sigma + C'')}\right]} \\ \lambda_2 = \sqrt{\dfrac{1}{2}\left[(\tau+\sigma+\gamma) + \sqrt{(\tau+\sigma+\gamma)^2 - 4(\tau\sigma + C'')}\right]} \end{cases} \qquad \text{(Equation 4.25)}$$

According to Euler's formula, for any real number x, e^{ix} can be expressed as
$e^{ix} = \cos x + i\sin x$;

hence $e^{\pm j\lambda \frac{z}{l}} = \cos\left(\lambda \dfrac{z}{l}\right) \pm j \sin\left(\lambda \dfrac{z}{l}\right)$. (Equation 4.26)

Substitute Equation 4.26 for the relevant terms of Equation 4.25, then:

$$F_z(z) = A_1 \cos\left(\lambda_1 \frac{z}{l}\right) + A_2 \sin\left(\lambda_1 \frac{z}{l}\right) + A_3 \cos\left(\lambda_2 \frac{z}{l}\right) + A_4 \sin\left(\lambda_2 \frac{z}{l}\right) \qquad \text{(Equation 4.27)}$$

where $A_1 = \overline{A}_1 + \overline{A}_2$; $A_2 = j(\overline{A}_1 - \overline{A}_2)$; $A_3 = \overline{A}_3 + \overline{A}_4$; $A_4 = j(\overline{A}_3 - \overline{A}_4)$

Equation 4.28 is obtained by substituting Equation 4.15 for the relevant terms of Equation 4.10.

$$\begin{cases} U_z(z) = -\dfrac{F_z'(z)}{\omega^2 \rho_p A_p} - \dfrac{C_p(z)}{\omega^2} \\ P(z) = \dfrac{F_z(z) - EA_p U_z'(z)}{\nu A_p b} \\ V(z) = \dfrac{P'(z)}{\omega^2 \rho_f} + \dfrac{C_f(z)}{\omega^2} \end{cases}$$

(Equation 4.28)

If substitute Equation 4.27 for Equation 4.28, it can be derived:

$$\begin{cases} U_z(z)=\dfrac{l}{A_pE\sigma}\left\{\lambda_1\left[A_1\sin\left(\lambda_1\dfrac{z}{l}\right)-A_2\cos\left(\lambda_1\dfrac{z}{l}\right)\right]+\lambda_2\left[A_3\sin\left(\lambda_2\dfrac{z}{l}\right)-A_4\cos\left(\lambda_2\dfrac{z}{l}\right)\right]\right\}-\dfrac{C_p(z)}{\omega^2} \\ P(z)=\dfrac{(\sigma-\lambda_1^2)}{A_pvb\sigma}\left[A_1\cos\left(\lambda_1\dfrac{z}{l}\right)+A_2\sin\left(\lambda_1\dfrac{z}{l}\right)\right]+(\sigma-\lambda_2^2)\left[A_3\cos\left(\lambda_2\dfrac{z}{l}\right)+A_4\sin\left(\lambda_2\dfrac{z}{l}\right)\right] \\ V(z)=\dfrac{-l}{A_pvbK^*\tau\sigma}\left\{(\sigma-\lambda_1^2)\lambda_1\left[A_1\sin\left(\lambda_1\dfrac{z}{l}\right)-A_2\cos\left(\lambda_1\dfrac{z}{l}\right)\right]+(\sigma-\lambda_2^2)\lambda_2\left[A_3\sin\left(\lambda_2\dfrac{z}{l}\right)-A_4\cos\left(\lambda_2\dfrac{z}{l}\right)\right]\right\}+\dfrac{C_f(z)}{\omega^2} \end{cases} \quad \text{(Equation 4.29)}$$

Combine Equation 4.27 and Equation 4.29, then:

$$\left.\begin{matrix}\text{Equation 4.27}\\ \text{Equation 4.29}\end{matrix}\right\}\Rightarrow\begin{Bmatrix}U_z\\P\\V\\F_z\end{Bmatrix}=\begin{bmatrix}B_1\sin\left(\lambda_1\dfrac{z}{l}\right) & -B_1\cos\left(\lambda_1\dfrac{z}{l}\right) & B_2\sin\left(\lambda_2\dfrac{z}{l}\right) & -B_2\cos\left(\lambda_2\dfrac{z}{l}\right)\\ B_3\cos\left(\lambda_1\dfrac{z}{l}\right) & B_3\sin\left(\lambda_1\dfrac{z}{l}\right) & B_4\cos\left(\lambda_2\dfrac{z}{l}\right) & B_4\sin\left(\lambda_2\dfrac{z}{l}\right)\\ -B_5\sin\left(\lambda_1\dfrac{z}{l}\right) & B_5\cos\left(\lambda_1\dfrac{z}{l}\right) & -B_6\sin\left(\lambda_2\dfrac{z}{l}\right) & B_6\cos\left(\lambda_2\dfrac{z}{l}\right)\\ \cos\left(\lambda_1\dfrac{z}{l}\right) & \sin\left(\lambda_1\dfrac{z}{l}\right) & \cos\left(\lambda_2\dfrac{z}{l}\right) & \sin\left(\lambda_2\dfrac{z}{l}\right)\end{bmatrix}\begin{Bmatrix}A_1\\A_2\\A_3\\A_4\end{Bmatrix}+\begin{Bmatrix}-\dfrac{C_p(z)}{\omega^2}\\0\\\dfrac{C_f(z)}{\omega^2}\\0\end{Bmatrix} \quad \text{(Equation 4.30)}$$

where $B_1=\dfrac{l\lambda_1}{A_pE\sigma}$ $B_2=\dfrac{l\lambda_2}{A_pE\sigma}$ $B_3=\dfrac{\sigma-\lambda_1^2}{A_pvb\sigma}$ $B_4=\dfrac{\sigma-\lambda_2^2}{A_pvb\sigma}$ $B_5=\dfrac{(\sigma-\lambda_1^2)l\lambda_1}{A_pvbK^*\tau\sigma}$ $B_6=\dfrac{(\sigma-\lambda_2^2)l\lambda_2}{A_pvbK^*\tau\sigma}$

The Equation 4.30 can be expressed as "[s(z)] = [B(z)] [A] + [C(z)]". Figure 4.2 illustrates a certain pipe section at a one-dimensional coordinate. This section has two nodes: *i* and *i–1*. For node *i–1*, it can be obtained:

$[s_{i-1}] = [B(0)]\ A + [C(0)] \Rightarrow A = [B(0)]^{-1}\ [s_{i-1}] - [B(0)]^{-1}\ [C(0)]$ (Equation 4.31)

For node *i*, the state vector can be displayed as: $[s_i] = [B(l)]\ A + [C(l)]$ (Equation 4.32)

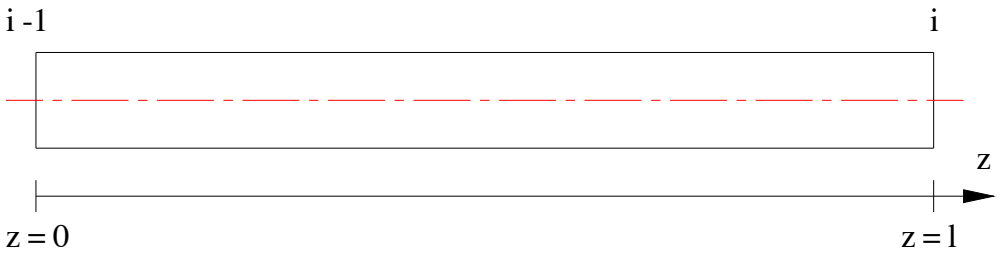

Figure 4.2 One-Dimensional representation of Pipe Section

Substitute Equation 4.31 for the relevant term of Equation 4.32, then:

$[s_i] = [T^F]\ [s_{i-1}] + [C(l)] - [T^F]\ [C(0)]$ (Equation 4.33)

i.e.

$$\begin{Bmatrix} U_z \\ P \\ V \\ F_z \end{Bmatrix}^i = \begin{bmatrix} T_{11}^F & T_{12}^F & T_{13}^F & T_{14}^F \\ T_{21}^F & T_{22}^F & T_{23}^F & T_{24}^F \\ T_{31}^F & T_{32}^F & T_{33}^F & T_{34}^F \\ T_{41}^F & T_{42}^F & T_{43}^F & T_{44}^F \end{bmatrix} \begin{Bmatrix} U_z \\ P \\ V \\ F_z \end{Bmatrix}^{i-1} + \begin{Bmatrix} -\dfrac{C_p(l)}{\omega^2} \\ 0 \\ \dfrac{C_f(l)}{\omega^2} \\ 0 \end{Bmatrix} - \begin{bmatrix} T_{11}^F & T_{12}^F & T_{13}^F & T_{14}^F \\ T_{21}^F & T_{22}^F & T_{23}^F & T_{24}^F \\ T_{31}^F & T_{32}^F & T_{33}^F & T_{34}^F \\ T_{41}^F & T_{42}^F & T_{43}^F & T_{44}^F \end{bmatrix} \begin{Bmatrix} -\dfrac{C_p(0)}{\omega^2} \\ 0 \\ \dfrac{C_f(0)}{\omega^2} \\ 0 \end{Bmatrix}$$

where

$$[T^F] = [B(l)][B(0)]^{-1} = \begin{bmatrix} T_{11}^F & T_{12}^F & T_{13}^F & T_{14}^F \\ T_{21}^F & T_{22}^F & T_{23}^F & T_{24}^F \\ T_{31}^F & T_{32}^F & T_{33}^F & T_{34}^F \\ T_{41}^F & T_{42}^F & T_{43}^F & T_{44}^F \end{bmatrix}; [C(l)] = \begin{Bmatrix} -\dfrac{C_p(l)}{\omega^2} \\ 0 \\ \dfrac{C_f(l)}{\omega^2} \\ 0 \end{Bmatrix}; [C(0)] = \begin{Bmatrix} -\dfrac{C_p(0)}{\omega^2} \\ 0 \\ \dfrac{C_f(0)}{\omega^2} \\ 0 \end{Bmatrix}$$

$[T^f]$ is the transfer field matrix of this pipe section. According to Equation 4.30, the matrices $[B(l)]$ and $[B(0)]^{-1}$ can be obtained. And the expressions of the elements of $[T^f]$ are shown as the following sixteen equations.

$$[\mathrm{B}(l)]=\begin{bmatrix} \dfrac{l\lambda_1}{A_pE\sigma}\sin\lambda_1 & -\dfrac{l\lambda_1}{A_pE\sigma}\cos\lambda_1 & \dfrac{l\lambda_2}{A_pE\sigma}\sin\lambda_2 & -\dfrac{l\lambda_2}{A_pE\sigma}\cos\lambda_2 \\ \dfrac{\sigma-\lambda_1^2}{A_pvb\sigma}\cos\lambda_1 & \dfrac{\sigma-\lambda_1^2}{A_pvb\sigma}\sin\lambda_1 & \dfrac{\sigma-\lambda_2^2}{A_pvb\sigma}\cos\lambda_2 & \dfrac{\sigma-\lambda_2^2}{A_pvb\sigma}\sin\lambda_2 \\ -\dfrac{(\sigma-\lambda_1^2)l\lambda_1}{A_pvbK^*\tau\sigma}\sin\lambda_1 & \dfrac{(\sigma-\lambda_1^2)l\lambda_1}{A_pvbK^*\tau\sigma}\cos\lambda_1 & -\dfrac{(\sigma-\lambda_2^2)l\lambda_2}{A_pvbK^*\tau\sigma}\sin\lambda_2 & \dfrac{(\sigma-\lambda_2^2)l\lambda_2}{A_pvbK^*\tau\sigma}\cos\lambda_2 \\ \cos\lambda_1 & \sin\lambda_1 & \cos\lambda_2 & \sin\lambda_2 \end{bmatrix}$$

$$[\mathrm{B}(0)]^{-1}=\begin{bmatrix} 0 & -\dfrac{A_pvb\sigma}{\lambda_1^2-\lambda_2^2} & 0 & \dfrac{\sigma-\lambda_2^2}{\lambda_1^2-\lambda_2^2} \\ -\dfrac{A_pE\sigma(\sigma-\lambda_2^2)}{l\lambda_1(\lambda_1^2-\lambda_2^2)} & 0 & -\dfrac{A_pvbK^*\tau\sigma}{l\lambda_1(\lambda_1^2-\lambda_2^2)} & 0 \\ 0 & \dfrac{A_pvb\sigma}{\lambda_1^2-\lambda_2^2} & 0 & -\dfrac{\sigma-\lambda_1^2}{\lambda_1^2-\lambda_2^2} \\ \dfrac{A_pE\sigma(\sigma-\lambda_1^2)}{l\lambda_2(\lambda_1^2-\lambda_2^2)} & 0 & \dfrac{A_pvbK^*\tau\sigma}{l\lambda_2(\lambda_1^2-\lambda_2^2)} & 0 \end{bmatrix}$$

$$\begin{cases} T_{11}^F=\dfrac{\sigma(\cos\lambda_1-\cos\lambda_2)-(\lambda_2^2\cos\lambda_1-\lambda_1^2\cos\lambda_2)}{\lambda_1^2-\lambda_2^2} \\ T_{12}^F=-\dfrac{lvb}{E}\dfrac{\lambda_1\sin\lambda_1-\lambda_2\sin\lambda_2}{\lambda_1^2-\lambda_2^2} \\ T_{13}^F=\dfrac{vbK^*\tau}{E}\dfrac{\cos\lambda_1-\cos\lambda_2}{\lambda_1^2-\lambda_2^2} \\ T_{14}^F=\dfrac{l}{A_pE\sigma}\dfrac{\sigma(\lambda_1\sin\lambda_1-\lambda_2\sin\lambda_2)-(\lambda_2^2\lambda_1\sin\lambda_1-\lambda_1^2\lambda_2\sin\lambda_2)}{\lambda_1^2-\lambda_2^2} \end{cases}$$

$$\begin{cases} T_{21}^F=-\dfrac{E}{lvb}\dfrac{(\sigma-\lambda_1^2)(\sigma-\lambda_2^2)}{\lambda_1^2-\lambda_2^2}\left(\dfrac{\sin\lambda_1}{\lambda_1}-\dfrac{\sin\lambda_2}{\lambda_2}\right) \\ T_{22}^F=\dfrac{(\lambda_1^2\cos\lambda_1-\lambda_2^2\cos\lambda_2)-\sigma(\cos\lambda_1-\cos\lambda_2)}{\lambda_1^2-\lambda_2^2} \\ T_{23}^F=\dfrac{K^*\tau}{l(\lambda_1^2-\lambda_2^2)}\left[(\lambda_1\sin\lambda_1-\lambda_2\sin\lambda_2)-\sigma\left(\dfrac{\sin\lambda_1}{\lambda_1}-\dfrac{\sin\lambda_2}{\lambda_2}\right)\right] \\ T_{24}^F=\dfrac{(\sigma-\lambda_1^2)(\sigma-\lambda_2^2)}{A_pvb\sigma(\lambda_1^2-\lambda_2^2)}(\cos\lambda_1-\cos\lambda_2) \end{cases}$$

$$\begin{cases} T_{31}^F = -\dfrac{E}{\nu b K^* \tau} \dfrac{\left(\sigma-\lambda_1^2\right)\left(\sigma-\lambda_2^2\right)}{\lambda_1^2-\lambda_2^2}\left(\cos\lambda_1-\cos\lambda_2\right) \\ T_{32}^F = \dfrac{l}{K^*\tau} \dfrac{\sigma\left(\lambda_1\sin\lambda_1-\lambda_2\sin\lambda_2\right)-\left(\lambda_1^2\lambda_1\sin\lambda_1-\lambda_2^2\lambda_2\sin\lambda_2\right)}{\lambda_1^2-\lambda_2^2} \\ T_{33}^F = \dfrac{\left(\lambda_1^2\cos\lambda_1-\lambda_2^2\cos\lambda_2\right)-\sigma\left(\cos\lambda_1-\cos\lambda_2\right)}{\lambda_1^2-\lambda_2^2} \\ T_{34}^F = -\dfrac{l}{A_p \nu b K^* \tau\sigma} \dfrac{\left(\sigma-\lambda_1^2\right)\left(\sigma-\lambda_2^2\right)}{\lambda_1^2-\lambda_2^2}\left(\lambda_1\sin\lambda_1-\lambda_2\sin\lambda_2\right) \end{cases}$$

$$\begin{cases} T_{41}^F = \dfrac{A_p E\sigma}{l\left(\lambda_1^2-\lambda_2^2\right)}\left[\left(\lambda_2^2\dfrac{\sin\lambda_1}{\lambda_1}-\lambda_1^2\dfrac{\sin\lambda_2}{\lambda_2}\right)-\sigma\left(\dfrac{\sin\lambda_1}{\lambda_1}-\dfrac{\sin\lambda_2}{\lambda_2}\right)\right] \\ T_{42}^F = -A_p \nu b\sigma \dfrac{\cos\lambda_1-\cos\lambda_2}{\lambda_1^2-\lambda_2^2} \\ T_{43}^F = -\dfrac{A_p \nu b K^* \tau\sigma}{l\left(\lambda_1^2-\lambda_2^2\right)}\left(\dfrac{\sin\lambda_1}{\lambda_1}-\dfrac{\sin\lambda_2}{\lambda_2}\right) \\ T_{44}^F = \dfrac{\sigma\left(\cos\lambda_1-\cos\lambda_2\right)-\left(\lambda_2^2\cos\lambda_1-\lambda_1^2\cos\lambda_2\right)}{\lambda_1^2-\lambda_2^2} \end{cases}$$

The relationship of axial vibrations between the adjacent nodes (*i* and *i–1*) is shown in Equation 4.33, in which the axial field transfer matrix of the pipe sections is expressed as:

$$\left[T^{F}_{f\text{-}p}\right]= \qquad \text{(Equation 4.34)}$$

$$\begin{bmatrix} \sigma C_2 - C_0 & \dfrac{l\left(C_1 - B^* C_3\right)}{E^*} & \dfrac{K^* \tau C_2}{E^*} & \dfrac{l\left[(\sigma+\gamma)C_3 - C_1\right]}{F^*} \\ \dfrac{E^* \sigma\gamma C_3}{l} & (\tau+\gamma)C_2 - C_0 & \dfrac{K^* \tau\left[(\tau+\gamma)C_3 - C_1\right]}{l} & -\dfrac{E^* \gamma C_2}{F^*} \\ \dfrac{E^* \sigma\gamma C_2}{K^* \tau} & \dfrac{l\left\{(\tau+\gamma)C_1 - \left[(\tau+\gamma)^2 + \sigma\gamma\right]C_3\right\}}{K^* \tau} & (\tau+\gamma)C_2 - C_0 & \dfrac{E^* l\gamma\left(B^* C_3 - C_1\right)}{F^* K^* \tau} \\ \dfrac{F^* \sigma\left(C_1 - \sigma C_3\right)}{l} & -\dfrac{F^* \sigma C_2}{E^*} & -\dfrac{F^* K^* \tau\sigma C_3}{E^* l} & \sigma C_2 - C_0 \end{bmatrix}$$

where

$$\frac{1}{K^*} = \frac{1}{K} + \frac{2r}{e_p E}\left(1 - \nu^2\right); \quad E^* = \frac{e_p E}{r\nu}; \quad F^* = A_p E;$$

$$\tau = \frac{\rho_f}{K^*}\omega^2 l^2; \quad \sigma = \frac{\rho_p}{E}\omega^2 l^2; \quad \gamma = \frac{2\rho_f \nu}{E^*}\omega^2 l^2;$$

$$\lambda_1^2 = \frac{1}{2}\left(B^* - \sqrt{B^{*2} - 4\left(\tau\sigma + C''\right)}\right); \quad B^* = \tau + \sigma + \gamma$$

$$\lambda_2^2 = \frac{1}{2}\left(B^* + \sqrt{B^{*2} - 4\left(\tau\sigma + C''\right)}\right); \quad C' = \text{constant}$$

$$C_0 = \frac{\lambda_2^2 \cos\lambda_1 - \lambda_1^2 \cos\lambda_2}{\lambda_1^2 - \lambda_2^2}; \quad C_1 = \frac{1}{\lambda_1^2 - \lambda_2^2}\left(\lambda_2^2 \frac{\sin\lambda_1}{\lambda_1} - \lambda_1^2 \frac{\sin\lambda_2}{\lambda_2}\right);$$

$$C_2 = \frac{\cos\lambda_1 - \cos\lambda_2}{\lambda_1^2 - \lambda_2^2}; \quad C_3 = \frac{1}{\lambda_1^2 - \lambda_2^2}\left(\frac{\sin\lambda_1}{\lambda_1} - \frac{\sin\lambda_2}{\lambda_2}\right)$$

From Equation 4.6, Equation 4.7, and Equation 4.4, the transfer field matrices of the x-z plane, y-z plane, and torsional direction can be derived. The detailed transforming process is described by Lesmez [56]. The relationship of lateral vibrations in two planes between the adjoining nodes (*i* and *i–1*) is shown in Equation 4.35, in which the lateral field transfer matrix of the pipe elements is expressed in Equation 4.36. The relationship of torsional vibrations between the two nodes is represented as Equation 4.37; and the torsional field transfer matrix of the pipe elements is shown as Equation 4.38.

$$\begin{Bmatrix} U_x \\ \Theta_y \\ M_y \\ F_x \end{Bmatrix}^i = \left[T^{F}_{x\text{-}y}\right]\begin{Bmatrix} U_x \\ \Theta_y \\ M_y \\ F_x \end{Bmatrix}^{i-1} \quad \& \quad \begin{Bmatrix} U_y \\ \Theta_x \\ M_x \\ F_y \end{Bmatrix}^i = \left[T^{F}_{x\text{-}y}\right]\begin{Bmatrix} U_y \\ \Theta_x \\ M_x \\ F_y \end{Bmatrix}^{i-1} \qquad \text{(Equation 4.35)}$$

$$\left[\mathrm{T}_{\text{x-y}}^{\mathrm{F}}\right]=\begin{bmatrix} C_0+\sigma C_2 & l\left[C_1+(\sigma-\tau)C_3\right] & \dfrac{l^2C_2}{\eta^*} & -\dfrac{l^3\left[\sigma C_1+\left(\sigma^2+\gamma\right)C_3\right]}{\eta^*\gamma} \\ \dfrac{\gamma C_3}{l} & C_0-\tau C_2 & \dfrac{l(C_1-\tau C_3)}{\eta^*} & -\dfrac{l^2C_2}{\eta^*} \\ \dfrac{\eta^*\gamma C_2}{l^2} & -\dfrac{\eta^*\left[\tau C_1-\left(\tau^2+\gamma\right)C_3\right]}{l} & C_0-\tau C_2 & -l\left[C_1+(\sigma-\tau)C_3\right] \\ -\dfrac{\eta^*\gamma(C_1+\sigma C_3)}{l^3} & -\dfrac{\eta^*\gamma C_2}{l^2} & -\dfrac{\gamma C_3}{l} & C_0+\sigma C_2 \end{bmatrix}$$

where (Equation 4.36)

$$\eta^*=\eta_p EI_p;\quad \tau=\frac{\rho_p I_p+\rho_f I_f}{\eta_p EI_p}\omega^2 l^2;\quad \sigma=\frac{\rho_p A_p+\rho_f A_f}{\kappa_p G_p A_p}\omega^2 l^2;\quad \gamma=\frac{\rho_p A_p+\rho_f A_f}{\eta_p EI_p}\omega^2 l^4;$$

$$\lambda_1^2=\frac{1}{2}\left[\sqrt{(\sigma+\tau)^2+4\gamma}+(\sigma-\tau)\right];\quad \lambda_2^2=\frac{1}{2}\left[\sqrt{(\sigma+\tau)^2+4\gamma}-(\sigma-\tau)\right];$$

$$C_0=\frac{\lambda_2^2\cosh\lambda_1+\lambda_1^2\cos\lambda_2}{\lambda_1^2+\lambda_2^2};\quad C_1=\frac{1}{\lambda_1^2+\lambda_2^2}\left(\lambda_2^2\frac{\sinh\lambda_1}{\lambda_1}+\lambda_1^2\frac{\sin\lambda_2}{\lambda_2}\right);$$

$$C_2=\frac{\cosh\lambda_1-\cos\lambda_2}{\lambda_1^2+\lambda_2^2};\qquad C_3=\frac{1}{\lambda_1^2+\lambda_2^2}\left(\frac{\sinh\lambda_1}{\lambda_1}-\frac{\sin\lambda_2}{\lambda_2}\right)$$

$$\begin{Bmatrix}\Theta_z\\ M_z\end{Bmatrix}^i=\left[\mathrm{T}_{\text{z-z}}^{\mathrm{F}}\right]\begin{Bmatrix}\Theta_z\\ M_z\end{Bmatrix}^{i-1} \qquad \text{(Equation 4.37)}$$

$$\left[\mathrm{T}_{\text{z-z}}^{\mathrm{F}}\right]=\begin{bmatrix}\cos\lambda & \dfrac{l}{G^*\lambda}\sin\lambda\\ -\dfrac{G^*\lambda}{l}\sin\lambda & \cos\lambda\end{bmatrix}\text{ where } G^*=G_pJ_p;\quad \lambda=\omega l\sqrt{\frac{\rho_p}{G_p}} \text{ (Equation 4.38)}$$

There are some differences between the equations of Lesmez and Equation 4.34 and 4.36 due to the different expression methods of the two studies and the probable editing errors of his thesis. Combining the Equation 4.33, 4.35, and 4.37, the entire field transfer matrix of pipe elements is:

$$
\begin{Bmatrix}
U_z \\ P \\ V \\ \frac{F_z}{U_x} \\ \Theta_y \\ M_y \\ \frac{F_x}{U_y} \\ \Theta_x \\ M_x \\ \frac{F_y}{\Theta_z} \\ M_z
\end{Bmatrix}^{i}
=
\begin{bmatrix}
\left[\mathrm{T}^{\mathrm{F}}_{\mathrm{f\text{-}p}}\right] & & [0] & \\
& \left[\mathrm{T}^{\mathrm{F}}_{\mathrm{x\text{-}y}}\right] & & \\
& & \left[\mathrm{T}^{\mathrm{F}}_{\mathrm{x\text{-}y}}\right] & \\
[0] & & & \left[\mathrm{T}^{\mathrm{F}}_{\mathrm{z\text{-}z}}\right]
\end{bmatrix}
\begin{Bmatrix}
U_z \\ P \\ V \\ \frac{F_z}{U_x} \\ \Theta_y \\ M_y \\ \frac{F_x}{U_y} \\ \Theta_x \\ M_x \\ \frac{F_y}{\Theta_z} \\ M_z
\end{Bmatrix}^{i-1}
+
\begin{Bmatrix}
-C_p(l)/\omega^2 \\ 0 \\ C_f(l)/\omega^2 \\ \frac{0}{0} \\ 0 \\ 0 \\ \frac{0}{0} \\ 0 \\ 0 \\ \frac{0}{0} \\ 0
\end{Bmatrix}^{i-1}
-
\begin{bmatrix}
\left[\mathrm{T}^{\mathrm{F}}_{\mathrm{f\text{-}p}}\right] & & [0] & \\
& \left[\mathrm{T}^{\mathrm{F}}_{\mathrm{x\text{-}y}}\right] & & \\
& & \left[\mathrm{T}^{\mathrm{F}}_{\mathrm{x\text{-}y}}\right] & \\
[0] & & & \left[\mathrm{T}^{\mathrm{F}}_{\mathrm{z\text{-}z}}\right]
\end{bmatrix}
\begin{Bmatrix}
-C_p(0)/\omega^2 \\ 0 \\ C_f(0)/\omega^2 \\ \frac{0}{0} \\ 0 \\ 0 \\ \frac{0}{0} \\ 0 \\ 0 \\ \frac{0}{0} \\ 0
\end{Bmatrix}^{i-1}
$$

(Equation 4.39)

4.3.3 Validation of field matrix

For many practical applications, the axial and one plane of lateral vibrations are normally analysed and investigated. Equation 4.1 describes the axial motion (z axis) of the pipe wall and fluid; and Equation 4.3 represents the y-z plane of transverse vibrations of the pipeline. In the actual applications, the two-dimensional and three-dimensional coordinates are used for different situations. In this dissertation, the basic coordinates established by the y and z axes are applied to the relevant expression and discussions.

In the Lesmez thesis [56], the derived matrices are verified by experiments. Since the fluid friction and structural damping have not been considered in these matrices and the expression is not the same as the matrices derived in the last section, more validation is needed.

Li etc. [45] presented an experiment in their paper and this system is used to verify the axial matrix. Table 4.1 lists the system parameters of the tube described in this paper, which lead to the modal frequencies shown in Table 4.2. Table 4.2 compares the calculation frequencies derived by the matrices in this thesis and the results displayed in this paper. It can be concluded that the two sets of frequencies show very little difference.

Table 4.1 System Parameters of Li's Example

Pipe properties	Fluid properties	System properties
Length: l = 4.5 m	Bulk modulus: K = 2.41 GPa	p_0 = 2.0 MPa
Inner radius: r = 26 mm	Density: ρ_f = 999 kg/m^3	
Wall thickness: e = 3.945 mm		
Young's modulus: E = 168 GPa		
Poisson's ratio: ν = 0.3		
Density: ρ_p = 7985 kg/m^3		
Mass at left end: m_0 = 1.312 kg		
Mass at right end: m_l = 0.3258 kg		

Table 4.2 Axial Matrix Verification

Frequency (Hz)	f_1	f_2	f_3	f_4	f_5	f_6	f_7	f_8
Li's paper	172	286	455	473	627	741	907	945
Axial matrix	171	285	454	472	626	740	907	944

For the lateral matrix, the model studied by Zhang and Hayama [114] is applied. The state variable method is used to analyse the model in Zhang's paper and the experimental validation is displayed. Table 4.3 gives the required system parameters; and Table 4.4 indicates that the simulation results of the model presented in this thesis is very similar to the frequency results shown in the paper. According to Table 4.2 and 4.4, it can be confidently concluded that the derived pipe model properly represents the dynamics of the liquid-filled straight pipe situation.

Table 4.3 System Parameters of Zhang's Example

Pipe properties	**Fluid properties**	**System properties**
Length: l = 2 m	Bulk modulus: K = 2.2 GPa	p_0 = 0 MPa
Inner radius: r = 8.05 mm	Density: ρ_f = 1000 kg/m^3	
Wall thickness: e = 2.8 mm		
Young's modulus: E = 210 GPa		
Shear modulus: G = 79.3 GPa		
Poisson's ratio: v = 0.3		
Density: ρ_p = 7860 kg/m^3		
Mass at ends: $m_0 = m_l$ = 0 kg		

Table 4.4 Lateral Matrix Verification

Frequency (Hz)	f_1	f_2	f_3	f_4	f_5
Zhang's paper	31.05	85.61	167.89	277.31	414.26
Axial matrix	31.11	85.55	167.51	276.53	412.13

4.4 Flexible Hose Modelling

Flexible hoses used in hydraulic piping systems can decrease the vibration induced by the pressure changes of the fluid. It also reduces the propagation speed of pressure ripples in the pipeline. For the HIS system studied in this research, hoses are equipped at the ends of pipelines, which tolerate the unfit assembly between the cylinders (fixed on wheel stations) and pipelines (mounted on vehicle chassis). For other HIS system mentioned in Chapter three, the hoses are not applied at the middle position of the pipeline may be because of the assembly requirement.

The hydraulic system always includes hoses, which typically consist of three main parts: the inner lining, the reinforcement and the outer lining or cover [70]. By employing one dimensional wave theory, four-equation longitudinal models can be derived and these models are normally divided into straight hose models and curved hose models. Longmore and Taylor developed a straight hose model [70, 71]; and a curved hose model is described by Longmore and Stammers [80]. Compared with the straight mode, the curved hose model replaces the force in the hose wall by the lateral displacement. Due to the combination requirement with pipe section model, the straight hose model is selected in this thesis.

4.4.1 Assumption [70, 71]

It is assumed that the curvature of a hose section is negligible so that any transverse bending vibration is not coupled with the longitudinal vibrations. The mean flow velocity is assumed to be negligible in comparison to the wave velocities. The influence of viscous losses in the fluid is not included in the model. It is also assumed that the radius of the hose is small compared with the acoustic wavelength in the fluid, which implies that the radial inertia of the fluid and the hose wall can be neglected.

The wall tension is taken almost entirely by the reinforcement that is made of homogeneous material, thus the hose wall is regarded as a thin cylindrical shell located at the mid-radius of the reinforcement. The densities of the lining and cover can be added to that of the reinforcement. Since the reinforcement of hydraulic hoses is normally one or two braids of high tensile steel wire, the Young's modulus of hose wall at lateral direc-

tion (E_x) is less than the one at longitudinal direction (E_z) due to this structure. The Poisson's ratios of hose wall at the two directions (ν_x and ν_z) are also different.

4.4.2 Field transfer matrix

The governing equation of a straight hose element in the axial direction is shown as Equation 4.40 [70, 71], in which the friction and damping factors are not included.

$$\begin{cases} \dfrac{\partial p}{\partial z}+\rho_f\dfrac{\partial^2 v}{\partial t^2}=0 \\ \dfrac{\partial f_z}{\partial z}-\rho_h c_r\dfrac{\partial^2 u_z}{\partial t^2}=0 \\ f_z-\nu_z c_r r_r p-E_z c_r\dfrac{\partial u_z}{\partial z}=0 \\ p-(2\nu_z-\psi_h)K_E\dfrac{\partial u_z}{\partial z}+\psi_f K_E\dfrac{\partial v}{\partial z}=0 \end{cases} \quad \text{where} \begin{cases} \dfrac{1}{K_E}=\dfrac{1}{K_C}+\dfrac{2r(1-\nu_z\nu_x)}{E_x} \\ \dfrac{1}{K_C}=\dfrac{\psi_f}{K_f}+\dfrac{\psi_h}{K_h} \\ \psi_f=\dfrac{A_f}{A_f+A_h} \quad \psi_h=\dfrac{A_h}{A_f+A_h} \\ c_r=2\pi r_r \end{cases} \qquad \text{(Equation 4.40)}$$

A_h cross-sectional area (m^2)

c_r circumference of reinforcement of hose wall (m)

e_h wall thickness (m)

E_x lateral Young's modulus of hose wall (Pa)

E_z axial Young's modulus of hose wall (Pa)

K_E modified bulk modulus of hose section (Pa)

r_r radius of reinforcement of hose wall (m)

ν_x lateral Poisson's ratio of hose wall

ν_z axial Poisson's ratio of hose wall

ρ_h mass density (kg/m^3)

According to Equation 4.10, the friction and damping factors can be added as:

$$\begin{cases} \dfrac{\partial p}{\partial z}+\rho_f\dfrac{\partial^2 v}{\partial t^2}+c_f=0 \\ \dfrac{\partial f_z}{\partial z}-\rho_h c_r\dfrac{\partial^2 u_z}{\partial t^2}+c_h=0 \\ f_z-\nu_z c_r r_r p-E_z c_r\dfrac{\partial u_z}{\partial z}=0 \\ p-(2\nu_z-\psi_h)K_E\dfrac{\partial u_z}{\partial z}+\psi_f K_E\dfrac{\partial v}{\partial z}=0 \end{cases} \quad \text{where} \begin{cases} c_f=n_f\dot{v}-n_f\dot{u}_z \\ c_h=n_h\dot{v}-(n_h+D_h)\dot{u}_z \end{cases} \qquad \text{(Equation 4.41)}$$

D_h damping coefficient per unit length of hose (s^{-1})

n_h structural damping coefficient of hose (s^{-1})

If we compare Equation 4.41 with Equation 4.10, it can be concluded that the two equations are similar. Table 4.5 lists the differences.

Table 4.5 Equation Comparison

Equation 4.10	A_p	v	r/e	E	$2v$	K^*
Equation 4.41	c_r	v_z	r_r	E_z	$2v_z - \psi_h$	$\psi_f K_E$

Using the similar deriving process, the axial field transfer matrix of the hose sections is:

$$\left[T^{F}_{f\text{-}h}\right] = \qquad \text{(Equation 4.42)}$$

$$\begin{bmatrix} \sigma C_2 - C_0 & \frac{l\left(C_1 - B^* C_3\right)}{E^*} & \frac{K^* \tau C_2}{E^*} & \frac{l\left[(\sigma+\gamma)C_3 - C_1\right]}{F^*} \\ \frac{E^* \sigma \gamma C_3}{l} & (\tau+\gamma)C_2 - C_0 & \frac{K^* \tau\left[(\tau+\gamma)C_3 - C_1\right]}{l} & -\frac{E^* \gamma C_2}{F^*} \\ \frac{E^* \sigma \gamma C_2}{K^* \tau} & \frac{l\left\{(\tau+\gamma)C_1 - \left[(\tau+\gamma)^2 + \sigma\gamma\right]C_3\right\}}{K^* \tau} & (\tau+\gamma)C_2 - C_0 & \frac{E^* l \gamma\left(B^* C_3 - C_1\right)}{F^* K^* \tau} \\ \frac{F^* \sigma\left(C_1 - \sigma C_3\right)}{l} & -\frac{F^* \sigma C_2}{E^*} & -\frac{F^* K^* \tau \sigma C_3}{E^* l} & \sigma C_2 - C_0 \end{bmatrix}$$

where

$$E^* = \frac{E_z}{v_z r_r}; \quad F^* = E_z c_r; \quad K^* = \psi_f K_E;$$

$$\tau = \frac{\rho_f}{K^*}\omega^2 l^2; \quad \sigma = \frac{\rho_h}{E_z}\omega^2 l^2; \quad \gamma = \frac{\rho_f\left(2v_z - \psi_h\right)}{\psi_f E^*}\omega^2 l^2;$$

$$\lambda_1^2 = \frac{1}{2}\left(B^* - \sqrt{B^{*2} - 4\left(\tau\sigma + C''\right)}\right); \quad B^* = \tau + \sigma + \gamma$$

$$\lambda_2^2 = \frac{1}{2}\left(B^* + \sqrt{B^{*2} - 4\left(\tau\sigma + C''\right)}\right); \quad C'' = \text{constant}$$

$$C_0 = \frac{\lambda_2^2 \cos\lambda_1 - \lambda_1^2 \cos\lambda_2}{\lambda_1^2 - \lambda_2^2}; \quad C_1 = \frac{1}{\lambda_1^2 - \lambda_2^2}\left(\lambda_2^2 \frac{\sin\lambda_1}{\lambda_1} - \lambda_1^2 \frac{\sin\lambda_2}{\lambda_2}\right);$$

$$C_2 = \frac{\cos\lambda_1 - \cos\lambda_2}{\lambda_1^2 - \lambda_2^2}; \quad C_3 = \frac{1}{\lambda_1^2 - \lambda_2^2}\left(\frac{\sin\lambda_1}{\lambda_1} - \frac{\sin\lambda_2}{\lambda_2}\right)$$

Regarding the hose as *soft* pipe, the lateral and torsional field transfer matrices are expressed as Equation 4.43 and 4.44 respectively according to Equation 4.36 and 4.38.

$$\left[\mathrm{T}^{\mathrm{F}}_{\text{x-y}}\right]=\begin{bmatrix} C_0+\sigma C_2 & l\left[C_1+(\sigma-\tau)C_3\right] & \dfrac{l^2C_2}{\eta^*} & -\dfrac{l^3\left[\sigma C_1+\left(\sigma^2+\gamma\right)C_3\right]}{\eta^*\gamma} \\ \dfrac{\gamma C_3}{l} & C_0-\tau C_2 & \dfrac{l(C_1-\tau C_3)}{\eta^*} & -\dfrac{l^2C_2}{\eta^*} \\ \dfrac{\eta^*\gamma C_2}{l^2} & -\dfrac{\eta^*\left[\tau C_1-\left(\tau^2+\gamma\right)C_3\right]}{l} & C_0-\tau C_2 & -l\left[C_1+(\sigma-\tau)C_3\right] \\ -\dfrac{\eta^*\gamma(C_1+\sigma C_3)}{l^3} & -\dfrac{\eta^*\gamma C_2}{l^2} & -\dfrac{\gamma C_3}{l} & C_0+\sigma C_2 \end{bmatrix}$$

where (Equation 4.43)

$$\eta^*=\eta_h E_x I_h;\quad \tau=\frac{\rho_h I_h+\rho_f I_f}{\eta_h E_x I_h}\omega^2 l^2;\quad \sigma=\frac{\rho_h A_h+\rho_f A_f}{\kappa_h G_h A_h}\omega^2 l^2;\quad \gamma=\frac{\rho_h A_h+\rho_f A_f}{\eta_h E_x I_h}\omega^2 l^4;$$

$$\lambda_1^2=\frac{1}{2}\left[\sqrt{(\sigma+\tau)^2+4\gamma}+(\sigma-\tau)\right];\quad \lambda_2^2=\frac{1}{2}\left[\sqrt{(\sigma+\tau)^2+4\gamma}-(\sigma-\tau)\right];$$

$$C_0=\frac{\lambda_2^2\cosh\lambda_1+\lambda_1^2\cos\lambda_2}{\lambda_1^2+\lambda_2^2};\quad C_1=\frac{1}{\lambda_1^2+\lambda_2^2}\left(\lambda_2^2\frac{\sinh\lambda_1}{\lambda_1}+\lambda_1^2\frac{\sin\lambda_2}{\lambda_2}\right);$$

$$C_2=\frac{\cosh\lambda_1-\cos\lambda_2}{\lambda_1^2+\lambda_2^2};\qquad C_3=\frac{1}{\lambda_1^2+\lambda_2^2}\left(\frac{\sinh\lambda_1}{\lambda_1}-\frac{\sin\lambda_2}{\lambda_2}\right)$$

G_h shear modulus of wall (Pa)

I_h area moment of inertia (m^4)

η_h rigidity factor for stiffness of elbow

κ_h shear coefficient for hollow circle cross section

$$\left[\mathrm{T}^{\mathrm{F}}_{\text{z-z}}\right]=\begin{bmatrix} \cos\lambda & \dfrac{l}{G^*\lambda}\sin\lambda \\ -\dfrac{G^*\lambda}{l}\sin\lambda & \cos\lambda \end{bmatrix} \text{ where } G^*=G_hJ_h;\ \lambda=\omega l\sqrt{\frac{\rho_h}{G_h}} \quad \text{(Equation 4.44)}$$

J_h polar moment of inertia (m^4)

Since the hose wall is considered as a thin cylindrical shell, the thickness of hose wall e_h is equal to zero. Therefore, the coefficient η_h is equal to 0.1, and $\kappa_h=\dfrac{2(1+\nu_x)}{4+3\nu_x}$. Like Equation 4.40, the entire field transfer matrix of the hose elements is:

$$
\begin{Bmatrix} U_z \\ P \\ V \\ F_z \\ \hline U_x \\ \Theta_y \\ M_y \\ F_x \\ \hline U_y \\ \Theta_x \\ M_x \\ F_y \\ \hline \Theta_z \\ M_z \end{Bmatrix}^{i} = \begin{bmatrix} \left[\mathrm{T}^{\mathrm{F}}_{\mathrm{f\text{-}h}}\right] & & & [0] \\ & \left[\mathrm{T}^{\mathrm{F}}_{\mathrm{x\text{-}y}}\right] & & \\ & & \left[\mathrm{T}^{\mathrm{F}}_{\mathrm{x\text{-}y}}\right] & \\ [0] & & & \left[\mathrm{T}^{\mathrm{F}}_{\mathrm{z\text{-}z}}\right] \end{bmatrix} \begin{Bmatrix} U_z \\ P \\ V \\ F_z \\ \hline U_x \\ \Theta_y \\ M_y \\ F_x \\ \hline U_y \\ \Theta_x \\ M_x \\ F_y \\ \hline \Theta_z \\ M_z \end{Bmatrix}^{i-1} + \begin{Bmatrix} -C_h(l)/\omega^2 \\ 0 \\ C_f(l)/\omega^2 \\ 0 \\ \hline 0 \\ 0 \\ 0 \\ 0 \\ \hline 0 \\ 0 \\ 0 \\ 0 \\ \hline 0 \\ 0 \end{Bmatrix}^{i-1} - \begin{bmatrix} \left[\mathrm{T}^{\mathrm{F}}_{\mathrm{f\text{-}h}}\right] & & & [0] \\ & \left[\mathrm{T}^{\mathrm{F}}_{\mathrm{x\text{-}y}}\right] & & \\ & & \left[\mathrm{T}^{\mathrm{F}}_{\mathrm{x\text{-}y}}\right] & \\ [0] & & & \left[\mathrm{T}^{\mathrm{F}}_{\mathrm{z\text{-}z}}\right] \end{bmatrix} \begin{Bmatrix} -C_h(0)/\omega^2 \\ 0 \\ C_f(0)/\omega^2 \\ 0 \\ \hline 0 \\ 0 \\ 0 \\ 0 \\ \hline 0 \\ 0 \\ 0 \\ 0 \\ \hline 0 \\ 0 \end{Bmatrix}^{i-1} \qquad \text{(Equation 4.45)}
$$

4.5 Modelling of Structural Discontinuities

As in any other chain system, a pipe system is treated as a collection of straight pipe elements that are joined end-to-end by various discontinuities, such as mass, supports, elbows and so on. Equilibrium and continuity relationships between the two sides of the interrupted nodes constitute the basis of their point transfer matrices. The point matrices of concentrated mass, spring support, and pipe bend have been derived in a two-dimensional space. The impact of the masses and supports on three directions (x, y, z) are decoupled. At the position of pipe bends, the junction coupling of the fluid pressure and the pipe wall moments and forces between the pipe sections are generated. These are due to the difference in orientation.

4.5.1 Concentrated mass

The impact of a concentrated mass (m_i) at axial and two lateral directions is described by Lesmez [56]. Figure 4.3 illustrates the influence at the torsional direction.

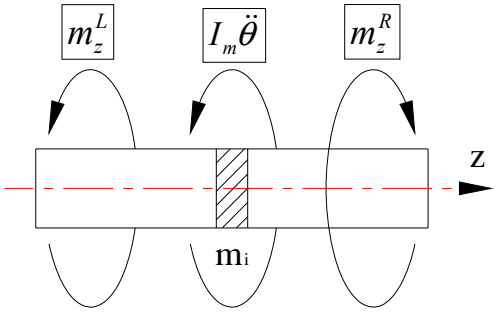

Figure 4.3 Free Body Diagram of Concentrated Mass at Torsional Direction

From the figure, it is derived that "$m_z^L + I_m^M \ddot{\theta}_z^L = m_z^R$". After substituting Equation 4.15 for the relevant term, it can be obtained that:

$$M_z^R = -\omega^2 I_m^M \Theta_z^L + M_z^L \qquad \text{(Equation 4.46)},$$

where the moment of inertia of the mass is expressed as "$I_m^M = \frac{1}{2} m_i \left(r + e_p\right)^2$" due to the negligible volume of the mass. According to the continuity of the pipe wall, the angular displacements of the two sides of the mass are the same. Therefore, the entire point transfer matrix of the concentrated mass is:

$$
\begin{Bmatrix} U_z \\ P \\ V \\ F_z \\ \hline U_x \\ \Theta_y \\ M_y \\ F_x \\ \hline U_y \\ \Theta_x \\ M_x \\ F_y \\ \hline \Theta_z \\ M_z \end{Bmatrix}^R_i
=
\left[\begin{array}{cccc|cccc|cccc|cc}
1 & 0 & 0 & 0 & & & & & & & & & & \\
0 & 1 & 0 & 0 & & & & & & & & & & \\
0 & 0 & 1 & 0 & & & & & & & & & & \\
-m_i\omega^2 & 0 & 0 & 1 & & & & & & & & & & \\
\hline
 & & & & 1 & 0 & 0 & 0 & & & & & & \\
 & & & & 0 & 1 & 0 & 0 & & & & & & \\
 & & & & 0 & 0 & 1 & 0 & & & & & & \\
 & & & & -m_i\omega^2 & 0 & 0 & 1 & & & & & & \\
\hline
 & & & & & & & & 1 & 0 & 0 & 0 & & \\
 & & & & & & & & 0 & 1 & 0 & 0 & & \\
 & & & & & & & & 0 & 0 & 1 & 0 & & \\
 & & & & & & & & -m_i\omega^2 & 0 & 0 & 1 & & \\
\hline
 & & & & & & & & & & & & 1 & 0 \\
 & & & & & & & & & & & & -I_m^M\omega^2 & 1
\end{array}\right]_{mass}
\begin{Bmatrix} U_z \\ P \\ V \\ F_z \\ \hline U_x \\ \Theta_y \\ M_y \\ F_x \\ \hline U_y \\ \Theta_x \\ M_x \\ F_y \\ \hline \Theta_z \\ M_z \end{Bmatrix}^L_i
$$

(Equation 4.47)

4.5.2 Spring support

Figure 4.4 illustrates the free body diagram of a typical spring support on the axial direction and it includes the damping effect. Equation 4.48 can be derived from the diagram. Substituting Equation 4.15 for the relevant terms of this equation, with the consideration of continuous pipe wall and continuous fluid velocities and continuous fluid pressure, the effect of axial spring support is described as Equation 4.49. The same deriving process can be obtained in *x* and *y* directions, thus the entire point transfer matrix of the spring support can be expressed as Equation 4.50.

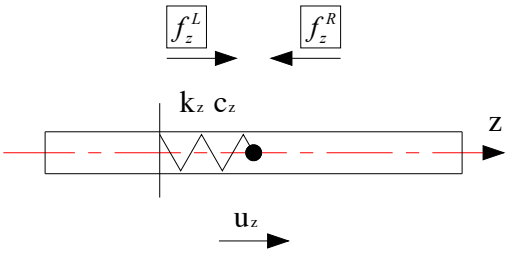

Figure 4.4 Free Body Diagram of Spring Support at Axial Direction

$$f_z^R = f_z^L + k_z u_z + c_z \dot{u}_z \quad \Rightarrow \quad F_z^R = (k_z + j\omega c_z) U_z^L + F_z^L \qquad \text{(Equation 4.48)}$$

$$\begin{Bmatrix} U_z \\ P \\ V \\ F_z \end{Bmatrix}_R = \begin{bmatrix} 1 & 0 & 0 & 0 \\ 0 & 1 & 0 & 0 \\ 0 & 0 & 1 & 0 \\ k_z + j\omega c_z & 0 & 0 & 1 \end{bmatrix} \begin{Bmatrix} U_z \\ P \\ V \\ F_z \end{Bmatrix}_L \qquad \text{(Equation 4.49)}$$

where c_z structural damping at z coordinate

$$
\begin{Bmatrix}
U_z \\ P \\ V \\ F_z \\ \hline U_x \\ \Theta_y \\ M_y \\ F_x \\ \hline U_y \\ \Theta_x \\ M_x \\ F_y \\ \hline \Theta_z \\ M_z
\end{Bmatrix}_i^R
=
\begin{bmatrix}
1 & 0 & 0 & 0 & & & & & & & & \\
0 & 1 & 0 & 0 & & & & & & & & \\
0 & 0 & 1 & 0 & & & & & & & & \\
k_z + j\omega c_z & 0 & 0 & 1 & & & & & & & & \\ \hline
 & & & & 1 & 0 & 0 & 0 & & & & \\
 & & & & 0 & 1 & 0 & 0 & & & & \\
 & & & & 0 & 0 & 1 & 0 & & & & \\
 & & & & k_x + j\omega c_x & 0 & 0 & 1 & & & & \\ \hline
 & & & & & & & & 1 & 0 & 0 & 0 \\
 & & & & & & & & 0 & 1 & 0 & 0 \\
 & & & & & & & & 0 & 0 & 1 & 0 \\
 & & & & & & & & k_y + j\omega c_y & 0 & 0 & 1 \\ \hline
 & & & & & & & & & & & \\
 & & & & & & & & & & &
\end{bmatrix}
\begin{bmatrix}
[0] & \\ & \\ & \\ & \\ & \\ & \\ & \\ & \\ & \\ & \\ & \\ & \\ & \\ 1 & 0 \\ 0 & 1
\end{bmatrix}_{spt}
\begin{Bmatrix}
U_z \\ P \\ V \\ F_z \\ \hline U_x \\ \Theta_y \\ M_y \\ F_x \\ \hline U_y \\ \Theta_x \\ M_x \\ F_y \\ \hline \Theta_z \\ M_z
\end{Bmatrix}_i^L
$$

(Equation 4.50)

where

c_x structural damping at x coordinate

c_y structural damping at y coordinate

4.5.3 Pipe elbow

The orientation of one pipe element is different from the one of the adjacent pipe element at the point of a pipe bend, in which the coupling of the velocities and forces of fluid and pipe wall are produced. It is very difficult to calculate the changes at the right side of the pipe bend from the analysis of the free body diagram of the bend. However, if we assume two local coordinates for the two pipe elements, named *right coordinates* and *left coordinates* respectively, the relationship between the pipe sections can be clearly described by transforming the coordinates.

Equation 4.51 shows the relationship. The φ_{pq} is the angle from the positive direction of left coordinates to right coordinates. The subscript "p" refers to the axis of left coordinates, and "q" refers to the axis of right coordinates. Since cos φ = cos (– φ), the "φ_{pq}" can be defined as the angle that is less than π, i.e. $\varphi_{pq} \leq \pi$.

$$\begin{Bmatrix} x \\ y \\ z \end{Bmatrix}^R = \begin{bmatrix} \cos\varphi_{11} & \cos\varphi_{21} & \cos\varphi_{31} \\ \cos\varphi_{12} & \cos\varphi_{22} & \cos\varphi_{32} \\ \cos\varphi_{13} & \cos\varphi_{23} & \cos\varphi_{33} \end{bmatrix} \begin{Bmatrix} x \\ y \\ z \end{Bmatrix}^L \qquad \text{(Equation 4.51)}$$

where
$$\begin{Bmatrix} \cos\varphi_{11} = x^L \to x^R & \cos\varphi_{21} = y^L \to x^R & \cos\varphi_{31} = z^L \to x^R \\ \cos\varphi_{12} = x^L \to y^R & \cos\varphi_{22} = y^L \to y^R & \cos\varphi_{32} = z^L \to y^R \\ \cos\varphi_{13} = x^L \to z^R & \cos\varphi_{23} = y^L \to z^R & \cos\varphi_{33} = z^L \to z^R \end{Bmatrix}$$

The following equations describe the relations between the left and right sides of the pipe bend on fluid velocity and pipe wall velocities and forces. The rotating angles and moments of the pipe wall and the fluid pressure are not influenced by the orientation changes.

$$\begin{cases} p^R = p^L \\ f_z^R + A_f p^R = f_x^L \cos\varphi_{13} + f_y^L \cos\varphi_{23} + \left(f_z^L + A_f p^L\right)\cos\varphi_{33} \\ f_x^R = f_x^L \cos\varphi_{11} + f_y^L \cos\varphi_{21} + \left(f_z^L + A_f p^L\right)\cos\varphi_{31} \\ f_y^R = f_x^L \cos\varphi_{12} + f_y^L \cos\varphi_{22} + \left(f_z^L + A_f p^L\right)\cos\varphi_{32} \end{cases}$$

$$\begin{cases} v^R - u_z^R = v^L - u_z^L \\ u_z^R = u_x^L \cos\varphi_{13} + u_y^L \cos\varphi_{23} + u_z^L \cos\varphi_{33} \\ u_x^R = u_x^L \cos\varphi_{11} + u_y^L \cos\varphi_{21} + u_z^L \cos\varphi_{31} \\ u_y^R = u_x^L \cos\varphi_{12} + u_y^L \cos\varphi_{22} + u_z^L \cos\varphi_{32} \end{cases}$$

If substitute Equation 4.15 for the above equations, it can be derived:

$$\begin{cases} U_z^R = \cos\varphi_{33} U_z^L + \cos\varphi_{13} U_x^L + \cos\varphi_{23} U_y^L \\ V^R = V^L + (\cos\varphi_{33} - 1) U_z^L + \cos\varphi_{13} U_x^L + \cos\varphi_{23} U_y^L \\ F_z^R = A_f (\cos\varphi_{33} - 1) P^L + \cos\varphi_{33} F_z^L + \cos\varphi_{13} F_x^L + \cos\varphi_{23} F_y^L \\ U_x^R = \cos\varphi_{31} U_z^L + \cos\varphi_{11} U_x^L + \cos\varphi_{21} U_y^L \\ F_x^R = A_f \cos\varphi_{31} P^L + \cos\varphi_{31} F_z^L + \cos\varphi_{11} F_x^L + \cos\varphi_{21} F_y^L \\ U_y^R = \cos\varphi_{32} U_z^L + \cos\varphi_{12} U_x^L + \cos\varphi_{22} U_y^L \\ F_y^R = A_f \cos\varphi_{32} P^L + \cos\varphi_{32} F_z^L + \cos\varphi_{12} F_x^L + \cos\varphi_{22} F_y^L \end{cases} \quad \text{and} \quad \begin{cases} P^R = P^L; \\ \Theta_y^R = \Theta_y^L; \quad M_y^R = M_y^L; \\ \Theta_x^R = \Theta_x^L; \quad M_x^R = M_x^L; \\ \Theta_z^R = \Theta_z^L; \quad M_z^R = M_z^L \end{cases}$$

Therefore, the point transfer matrix of the pipe bend is shown as Equation 4.52.

$$
\begin{Bmatrix} U_z \\ P \\ V \\ F_z \\ U_x \\ \Theta_y \\ M_y \\ F_x \\ U_y \\ \Theta_x \\ M_x \\ F_y \\ \Theta_z \\ M_z \end{Bmatrix}_i^R =
\begin{bmatrix}
\cos\varphi_{33} & 0 & 0 & 0 & \cos\varphi_{13} & 0 & 0 & 0 & \cos\varphi_{23} & 0 & 0 & 0 & 0 & 0 \\
0 & 1 & 0 & 0 & 0 & 0 & 0 & 0 & 0 & 0 & 0 & 0 & 0 & 0 \\
\cos\varphi_{33}-1 & 0 & 1 & 0 & \cos\varphi_{13} & 0 & 0 & 0 & \cos\varphi_{23} & 0 & 0 & 0 & 0 & 0 \\
0 & A_f(\cos\varphi_{33}-1) & 0 & \cos\varphi_{33} & 0 & 0 & 0 & \cos\varphi_{13} & 0 & 0 & 0 & \cos\varphi_{23} & 0 & 0 \\
\cos\varphi_{13} & 0 & 0 & 0 & \cos\varphi_{11} & 0 & 0 & 0 & \cos\varphi_{21} & 0 & 0 & 0 & 0 & 0 \\
0 & 0 & 0 & 0 & 0 & 1 & 0 & 0 & 0 & 0 & 0 & 0 & 0 & 0 \\
0 & 0 & 0 & 0 & 0 & 0 & 1 & 0 & 0 & 0 & 0 & 0 & 0 & 0 \\
0 & A_f\cos\varphi_{31} & 0 & \cos\varphi_{31} & 0 & 0 & 0 & \cos\varphi_{11} & 0 & 0 & 0 & \cos\varphi_{21} & 0 & 0 \\
\cos\varphi_{32} & 0 & 0 & 0 & \cos\varphi_{12} & 0 & 0 & 0 & \cos\varphi_{22} & 0 & 0 & 0 & 0 & 0 \\
0 & 0 & 0 & 0 & 0 & 0 & 0 & 0 & 0 & 1 & 0 & 0 & 0 & 0 \\
0 & 0 & 0 & 0 & 0 & 0 & 0 & 0 & 0 & 0 & 1 & 0 & 0 & 0 \\
0 & A_f\cos\varphi_{32} & 0 & \cos\varphi_{32} & 0 & 0 & 0 & \cos\varphi_{12} & 0 & 0 & 0 & \cos\varphi_{22} & 0 & 0 \\
0 & 0 & 0 & 0 & 0 & 0 & 0 & 0 & 0 & 0 & 0 & 0 & 1 & 0 \\
0 & 0 & 0 & 0 & 0 & 0 & 0 & 0 & 0 & 0 & 0 & 0 & 0 & 1
\end{bmatrix}_{bend}
\begin{Bmatrix} U_z \\ P \\ V \\ F_z \\ U_x \\ \Theta_y \\ M_y \\ F_x \\ U_y \\ \Theta_x \\ M_x \\ F_y \\ \Theta_z \\ M_z \end{Bmatrix}_i^L
$$

(Equation 4.52)

4.6 Modelling of Fluidic Discontinuities

A hydraulic system consists of not only structural discontinuities, but also fluidic break-points like valves and accumulators. According to previous studies, the models of hydraulic components are developed on the basis of rigid pipe structures [12, 91, 98, 115]. With this assumption, the impedance characteristics of the components, which include the resistance (pressure loss), the inductance (fluid inertia) and the capacitance (fluid compressibility), are investigated [64-68, 116-120]. The fluid system equations obtained from these approaches are linear, but frequency-dependent, and the analysis process is in the frequency domain. This thesis models the hydraulic components with a flexible pipe assumption. They are treated as fluidic discontinuities of a hydraulic circuit. And the impedance characteristics of the components are included in their point transfer matrices.

4.6.1 Valve

The hydraulic system includes various valves, in which the relief valves are investigated by Edge, Johnston and Brunelli [64, 116, 117]. The valves employed in the HIS system studied in this thesis are multi-stage, shim-stack-and-spring damper valves [12]. The main function of the valves is to provide damping of the HIS. The relationship between pressure loss and flow rate is nearly proportional [12], thus the valve is simplified as a sharp-edged constant-area orifice when it is modelled. According to the block reference of MATLAB® [121], this type of orifice is modelled as the fixed orifice block, as shown in Figure 4.5.

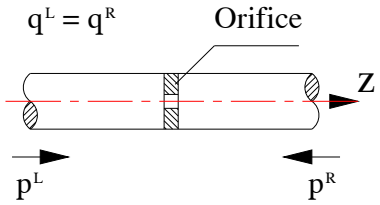

Figure 4.5 Sharp-Edged Constant-Area Orifice

Flow rate (q) through the orifice is proportional to the pressure differential across the orifice. Under the working condition of the HIS, the value of the Reynolds number for the hydraulic circuit is less than the critical Reynolds number, thus the flow rate is de-

termined according to the equation "$q = k_{orf}\,(p^R - p^L)$", in which k_{orf} is the orifice coefficient [121]. For laminar flow and a low Reynolds number condition, the pressure-flow characteristic for the orifice can be given by the equation "$\Delta p/q = Z_o = R_o + j\omega L_o$", in which Z_o is impedance coefficient; R_o is resistance coefficient; and L_o is inductance coefficient [65, 118].

The discontinuities are considered as points, thus the mass and dimension of the orifice is ignored. Additionally, at the point, the orifice and pipe wall are regarded as rigid bodies. Figure 4.6 illustrates the free body diagram of the orifice.

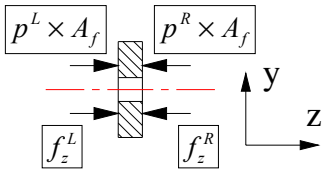

Figure 4.6 Free Body Diagram of Fixed Orifice

The fluid flow is not changed if we discount the leakage between the edge of the orifice and the pipe wall. The flow can be expressed as three equations; then Equation 4.53 and Equation 4.54 can be derived.

$$\left.\begin{aligned} q &= A_f\left(\dot{v}^L - \dot{u}_z^L\right) \\ q &= \frac{p^L - p^R}{Z_o} \\ q &= A_f\left(\dot{v}^R - \dot{u}_z^R\right) \end{aligned}\right\} \Rightarrow \begin{cases} p^R = p^L - A_f Z_o\left(\dot{v}^L - \dot{u}_z^L\right) & \text{(Equation 4.53)} \\ \dot{v}^R - \dot{u}_z^R = \dot{v}^L - \dot{u}_z^L & \text{(Equation 4.54)} \end{cases}$$

From the Figure 4.6, it is derived that "$f_z^R + p^R A_f = p^L A_f + f_z^L$". Substitute p^R for Equation 4.53, then: $f_z^R = f_z^L + Z_o A_f^2\left(\dot{v}^L - \dot{u}_z^L\right)$. (Equation 4.55)

Considering the continuity of the pipe wall with the negligible mass and volume of the orifice, it can obtain the next equations.

$$\begin{cases} u_z^R = u_z^L; \quad u_x^R = u_x^L; \quad u_y^R = u_y^L \\ \theta_y^R = \theta_y^L; \quad \theta_x^R = \theta_x^L; \quad \theta_z^R = \theta_z^L \\ m_y^R = m_y^L; \quad m_x^R = m_x^L; \quad m_z^R = m_z^L \\ f_x^R = f_x^L; \quad f_y^R = f_y^L \end{cases}$$

Combining Equation 4.53, 4.54, and 4.55 and substituting Equation 4.15 for the relevant terms of the equations, Equation 4.56 can be derived. Equation 4.57 is the matrix form of Equation 4.56.

$$\begin{cases} U_z^R = U_z^L; \quad P^R = j\omega Z_o A_f U_z^L + P^L - j\omega Z_o A_f V^L \\ V^R = V^L; \quad F_z^R = -j\omega Z_o A_f^2 U_z^L + j\omega Z_o A_f^2 V^L + F_z^L \\ U_x^R = U_x^L; \quad \Theta_y^R = \Theta_y^L; \quad M_y^R = M_y^L; \quad F_x^R = F_x^L \\ U_y^R = U_y^L; \quad \Theta_x^R = \Theta_x^L; \quad M_x^R = M_x^L; \quad F_y^R = F_y^L \\ \Theta_z^R = \Theta_z^L; \quad M_z^R = M_z^L \end{cases} \qquad \text{(Equation 4.56)}$$

$$
\begin{Bmatrix} U_z \\ P \\ V \\ \hline F_z \\ U_x \\ \Theta_y \\ M_y \\ \hline F_x \\ U_y \\ \Theta_x \\ M_x \\ \hline F_y \\ \Theta_z \\ M_z \end{Bmatrix}_i^R = \begin{bmatrix} 1 & 0 & 0 & 0 \\ j\omega Z_o A_f & 1 & -j\omega Z_o A_f & 0 \\ 0 & 0 & 1 & 0 \\ -j\omega Z_o A_f^2 & 0 & j\omega Z_o A_f^2 & 1 \end{bmatrix} \begin{bmatrix} 1 & 0 & 0 & 0 \\ 0 & 1 & 0 & 0 \\ 0 & 0 & 1 & 0 \\ 0 & 0 & 0 & 1 \end{bmatrix} \begin{bmatrix} 1 & 0 & 0 & 0 \\ 0 & 1 & 0 & 0 \\ 0 & 0 & 1 & 0 \\ 0 & 0 & 0 & 1 \end{bmatrix} \begin{bmatrix} [0] \\ \hline [0] \\ \hline 1 & 0 \\ 0 & 1 \end{bmatrix}_{orf} \begin{Bmatrix} U_z \\ P \\ V \\ \hline F_z \\ U_x \\ \Theta_y \\ M_y \\ \hline F_x \\ U_y \\ \Theta_x \\ M_x \\ \hline F_y \\ \Theta_z \\ M_z \end{Bmatrix}_i^L
$$

(Equation 4.57)

4.6.2 Accumulator

The accumulator studied in this research is the gas-charged accumulator, named the nitrogen-filled diaphragm-type hydraulic accumulator [12]. The accumulator consists of two chambers separated by an elastomeric diaphragm. One is filled with pre-charged gas and the other with fluid from the hydraulic circuit. When the fluid pressure at the hydraulic circuit becomes higher than the pre-charged pressure, fluid enters the accumulator chamber and compresses the gas. A drop of fluid pressure in the circuit pushes the stored fluid back into the system [122].

Figure 4.7 shows a gas-charged accumulator, with an orifice fixed at the neck.

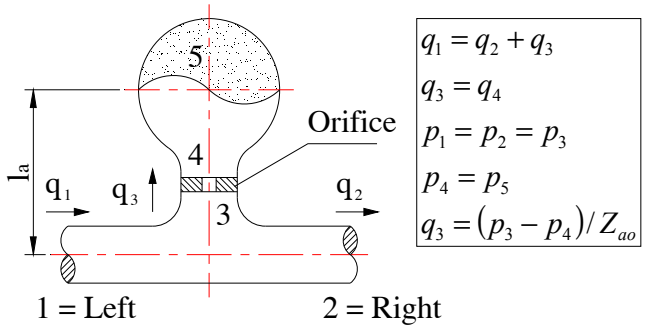

Figure 4.7 Gas-Charged Accumulator

The status of the accumulator can be divided into two stages: one is from pre-charge to start-working (non-adiabatic process), the other is working condition (adiabatic process). The stages are described by the following equations:

$$\begin{cases} p_0 \not{V}_0 = p_{pre} \not{V}_{pre} \quad \Rightarrow \quad p_0 = \dfrac{p_{pre} \not{V}_{pre}}{\not{V}_0} & \text{non - adiabatic stage} \\ p_5 \left(\not{V}_0 - \not{V}_f \right)^{\gamma} = p_0 \not{V}_0^{\gamma} \Rightarrow p_5 = p_0 \left(\dfrac{\not{V}_0}{\not{V}_0 - \not{V}_f} \right)^{\gamma} & \text{adiabatic stage} \end{cases}$$

where

$\not{V}$ volume of gas (m^3)

γ ratio of specific heats for nitrogen

Under working condition, it can be concluded that "$p_5 (\not{V}_0 - \not{V}_f)^{\gamma}$ = constant". (Eq. 4.58) If we logarithmically transform the two sides of the equation, then we can obtain the differential form of the equation, which can be displayed as:

$$\text{Equation 4.58} \Rightarrow \ln(p_5)+\gamma\ln(\forall_0-\forall_f)=\ln(\text{constant}) \Rightarrow \frac{\dot{p}_5}{p_5}+\frac{\gamma}{\forall_0-\forall_f}\frac{d(\forall_0-\forall_f)}{dt}=0$$

$$\Rightarrow \frac{\dot{p}_5}{p_5}+\frac{\gamma}{\forall_0-\forall_f}\left(-\frac{d\forall_f}{dt}\right)=\frac{\dot{p}_5}{p_5}+\frac{\gamma}{\forall_0-\forall_f}(-q_3)=0$$

$$\Rightarrow \quad q_3=\frac{\dot{p}_5(\forall_0-\forall_f)}{\gamma p_5} \qquad \text{(Equation 4.59)}$$

In the equations, p_0 is the pre-pressure of the hydraulic circuit; $\forall_0$ is the gas volume in the accumulator under this pre-pressure; $\forall_f$ is the volume of fluid flowing into the accumulator; and p_{pre} and $\forall_{pre}$ are the gas pressure and volume of the accumulator as manufacturer parameters.

The impedance characteristic of the accumulator is defined as "$Z_a = p_4/q_4$" [64]. Since "$q_3 = q_4$" and "$p_4 = p_5$", substitute Equation 4.59 for q_4, then it can be obtained that "$Z_a=\frac{(p_5)^2\gamma}{\dot{p}_5(\forall_0-\forall_f)}$". If substitute Equation 4.15 ($p = P\,e^{j\omega t}$) for p_5, Equation 4.60 can be concluded.

$$Z_a=\frac{P_5^2\left(e^{j\omega t}\right)^2\gamma}{j\omega P_5(\forall_0-\forall_f)e^{j\omega t}}=\frac{p_5^2\gamma}{j\omega p_5(\forall_0-\forall_f)} \qquad \text{(Equation 4.60)}$$

If we ignore the influence of the orifice, the relationship between pressures is "$p_1 = p_2 = p_3 = p_4 = p_5$". Since p_0 is the mean value of p_1, it can be concluded that "$p_1^2 = p_0^2$". According to ideal gas law, it can be derived that "$p_5(\forall_0-\forall_f)=p_{pre}\forall_{pre}$". Combining these conditions, equation 4.60 can be expressed as "$Z_a=\frac{\gamma p_0^2}{j\omega p_{pre}\forall_{pre}}$".(Equation 4.61)

It is defined that the impedance characteristics of an accumulator consist of three parameters: capacitance, inductance, and resistance [64], shown as Equation 4.62. They describe the capacitance term that is the same as Equation 4.61. The inductance (L_a) is due to the inertia of the fluid contained within the accumulator, which will become significant at higher frequencies. Under most circumstances, the resistance (R_a) has a minor effect and may be ignored.

$$Z_a = \frac{\gamma p_0^2}{j\omega p_{pre} V_{pre}} + j\omega L_a + R_a \qquad \text{(Equation 4.62)}$$

From Figure 4.7, if the orifice is included in the consideration, the following equations can serve to describe the relationship between fluid pressure and flow rate at the accumulator.

$$\left.\begin{aligned} &p_4 = q_4 Z_a \\ &q_3 = q_4 = \frac{p_3 - p_4}{Z_{ao}} \\ &p_1 = p_2 = p_3 \end{aligned}\right\} \Rightarrow \quad q_3 = \frac{p_1}{Z_a + Z_{ao}}; \quad \left.\begin{aligned} &q_1 = q_2 + q_3 \\ &q_1 = A_f(\dot{v}_1 - \dot{u}_{z1}) \\ &q_2 = A_f(\dot{v}_2 - \dot{u}_{z2}) \end{aligned}\right\} \Rightarrow \quad \dot{v}_2 - \dot{u}_{z2} = \dot{v}_1 - \dot{u}_{z1} - \frac{q_3}{A_f}$$

$$\Rightarrow \quad \dot{v}^R - \dot{u}_z^R = \dot{v}^L - \dot{u}_z^L - \frac{p^L}{A_f(Z_a + Z_{ao})} \qquad \text{(Equation 4.63)}$$

where $Z_a = \frac{\gamma p_0^2}{j\omega p_{pre} V_{pre}} + j\omega L_a + R_a; \quad Z_{ao} = R_{ao} + j\omega L_{ao}$

Z_{ao} impedance of orifice in the accumulator

L_{ao} inductance of orifice in the accumulator

R_{ao} resistance of orifice in the accumulator

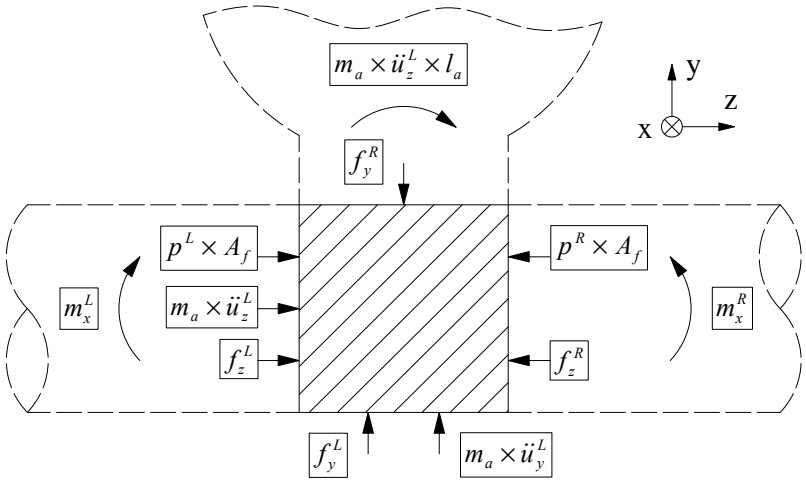

Figure 4.8 Free Body Diagram of T Junction of Accumulator

Figure 4.8 shows the free body diagram of the fluid at the junction of the accumulator and the pipe, in which m_a is the mass of the accumulator and l_a is the distance between the centre line of the pipe and the centre of the accumulator ball. From this figure, it can be derived that:

$$\begin{cases} p^L A_f + f_z^L + m_a \ddot{u}_z^L = p^R A_f + f_z^R \quad \Rightarrow \quad f_z^R = f_z^L + m_a \ddot{u}_z^L \\ f_y^L + m_a \ddot{u}_y^L = f_y^R \quad \Rightarrow \quad f_y^R = f_y^L + m_a \ddot{u}_y^L \\ m_x^L + m_a \ddot{u}_z^L l_a = m_x^R \quad \Rightarrow \quad m_x^R = m_x^L + m_a \ddot{u}_z^L l_a \end{cases} \qquad \text{(Equation 4.64)}$$

Ignoring the volume of accumulator, the pipe wall is treated as a continuous body, thus it can be obtained that "$u_z^R = u_z^L$", "$u_y^R = u_y^L$", and "$\theta_x^R = \theta_x^L$". If substitute Equation 4.15 for the relevant terms of the three equations and Equation 4.63 and 4.64, it can be derived that:

$$\begin{cases} U_z^R = U_z^L; \quad P^R = P^L \\ V^R = -\dfrac{1}{j\omega A_f \left(Z_a + Z_{ao}\right)} P^L + V^L; \quad F_z^R = -\omega^2 m_a U_z^L + F_z^L \\ U_y^R = U_y^L; \quad \Theta_x^R = \Theta_x^L \\ M_x^R = -\omega^2 m_a l_a U_z^L + M_x^L; \quad F_y^R = -\omega^2 m_a U_y^L + F_y^L \end{cases} \qquad \text{(Equation 4.65)}$$

Figure 4.8 illustrates the relations of forces and moments in the y-z plane. Applying the same analysis to the x-z plane, it can be concluded that the moment created by the accumulator does not have any effect on this plane. Then Equation 4.66 can be derived.

$$U_x^R = U_x^L; \quad \Theta_y^R = \Theta_y^L; \quad M_y^R = M_y^L; \quad F_x^R = -\omega^2 m_a U_x^L + F_x^L \qquad \text{(Equation 4.66)}$$

At the torsional direction, the influence of the accumulator is a concentrated mass, thus it can be obtained that "$m_z^L + I_a^M \ddot{\theta}_z^L = m_z^R$". Substitute Equation 4.15 for the relevant term, then:

$$M_z^R = -\omega^2 I_a^M \Theta_z^L + M_z^L \qquad \text{(Equation 4.67)}$$

where I_a^M moment of inertia of accumulator (kg m^2)

The point transfer matrix of accumulators is obtained by combining Equation 4.65, 4.66 and 4.67, shown as Equation 4.68.

$$
\begin{Bmatrix}
U_z \\ P \\ V \\ \dfrac{F_z}{U_x} \\ \Theta_y \\ M_y \\ \dfrac{F_x}{U_y} \\ \Theta_x \\ M_x \\ \dfrac{F_y}{\Theta_z} \\ M_z
\end{Bmatrix}_i^R
=
\begin{bmatrix}
\begin{array}{cccc}
1 & 0 & 0 & 0 \\
0 & 1 & 0 & 0 \\
0 & -\dfrac{1}{j\omega A_f\left(Z_a + Z_{ao}\right)} & 1 & 0 \\
-\omega^2 m_a & 0 & 0 & 1
\end{array}
& [0] & [0] & [0] \\
[0] &
\begin{array}{cccc}
1 & 0 & 0 & 0 \\
0 & 1 & 0 & 0 \\
0 & 0 & 1 & 0 \\
-\omega^2 m_a & 0 & 0 & 1
\end{array}
& [0] & [0] \\
[0] & [0] &
\begin{array}{cccc}
1 & 0 & 0 & 0 \\
0 & 1 & 0 & 0 \\
0 & 0 & 1 & 0 \\
-\omega^2 m_a & 0 & 0 & 1
\end{array}
& [0] \\
[0] & [0] & [0] &
\begin{array}{cc}
1 & 0 \\
-\omega^2 I_a^M & 1
\end{array}
\end{bmatrix}_{acm}
\begin{Bmatrix}
U_z \\ P \\ V \\ \dfrac{F_z}{U_x} \\ \Theta_y \\ M_y \\ \dfrac{F_x}{U_y} \\ \Theta_x \\ M_x \\ \dfrac{F_y}{\Theta_z} \\ M_z
\end{Bmatrix}_i^L
$$

(Equation 4.68)

4.7 Element Model Combination

One system always consists of multiple sub-systems. The matrices of various types of elements are described in the above sections. In order to obtain the model of a hydraulic circuit, the single matrix of every element is combined with each other. For the type of liquid-filled pipe-guided hydraulic circuits, different combinations of elements comprise different systems. Since the circuit is located at the three-dimensional space, the local coordinates of one pipe/hose section are different to those of the other. Before connecting the component matrices, their coordinates need to be uniform. For the description of the transform process and derivation of the transform matrix refer to the study of Lesmez [56].

4.7.1 Coordinate transformation

The transfer matrices and state vectors are developed based on the local coordinate system (*x*-*y*-*z*), which is associated with every particular subsystem. In order to combine the state vectors of one pipe or hose element to those of the adjacent element, the local state vectors are represented by applying a set of global coordinates (*X*-*Y*-*Z*), which are fixed with the whole system. The local coordinates and the global coordinates are related by a transformation matrix. The direction cosines of local axes and global axes are used to define the matrix.

The relationship between each local coordinate and the global coordinates is very similar to the situation of the pipe bend. For each pipe or hose element, the global coordinates can be regarded as the "*left coordinates*". Therefore, Equation 4.69 describes the relationship. The φ_{pq} is the angle from the positive direction of local coordinates to global coordinates. The subscript "*p*" refers to the axis of local coordinates, and "*q*" refers to the axis of global coordinates. Since cos φ = cos (– φ), the "φ_{pq}" can be defined as the angle that is less than π, i.e. $\varphi_{pq} \leq \pi$.

$$\begin{Bmatrix} x \\ y \\ z \end{Bmatrix} = \begin{bmatrix} \cos\varphi_{Xx} & \cos\varphi_{Yx} & \cos\varphi_{Zx} \\ \cos\varphi_{Xy} & \cos\varphi_{Yy} & \cos\varphi_{Zy} \\ \cos\varphi_{Xz} & \cos\varphi_{Yz} & \cos\varphi_{Zz} \end{bmatrix} \begin{Bmatrix} X \\ Y \\ Z \end{Bmatrix} \qquad \text{(Equation 4.69)}$$

When the transfer matrices of all elements are combined, the coordinate-transformation matrices of middle elements are eliminated during the mathematical process. It can be concluded that the final transfer matrix of the whole system is only related to the transformation matrices at the beginning and the end elements. Without considering the friction and damping impact, the final equation is expressed as Equation 4.70.

$$\mathbf{S}_N^R = \mathbf{t}_{N-1}^{-1}\,\mathbf{T}'\,\mathbf{t}_1\,\mathbf{S}_1^L \qquad \text{(Equation 4.70)}$$

where

$\mathbf{S}_N^R$ the state vector of the end node

$\mathbf{S}_1^L$ the state vector of the beginning node

$\mathbf{t}_{N-1}^{-1}$ the coordinate-transformation matrix of the end element

$\mathbf{t}_1$ the coordinate-transformation matrix of the beginning element

$\mathbf{T}'$ the combined transfer matrix of all nodes and elements

The coordinate-transformation matrix $\mathbf{t}$ is a 14×14 matrix and given by:

$$
\mathbf{t} = \begin{bmatrix}
\cos\varphi_{Zz} & 0 & 0 & 0 & \cos\varphi_{Xz} & 0 & 0 & 0 & \cos\varphi_{Yz} & 0 & 0 & 0 & 0 & 0 \\
0 & 1 & 0 & 0 & 0 & 0 & 0 & 0 & 0 & 0 & 0 & 0 & 0 & 0 \\
\cos\varphi_{Zz} - 1 & 0 & 1 & 0 & \cos\varphi_{Xz} & 0 & 0 & 0 & \cos\varphi_{Yz} & 0 & 0 & 0 & 0 & 0 \\
0 & A_f\left(\cos\varphi_{Zz} - 1\right) & 0 & \cos\varphi_{Zz} & 0 & 0 & 0 & \cos\varphi_{Xz} & 0 & 0 & 0 & \cos\varphi_{Yz} & 0 & 0 \\
\cos\varphi_{Xz} & 0 & 0 & 0 & \cos\varphi_{Xx} & 0 & 0 & 0 & \cos\varphi_{Yx} & 0 & 0 & 0 & 0 & 0 \\
0 & 0 & 0 & 0 & 0 & 1 & 0 & 0 & 0 & 0 & 0 & 0 & 0 & 0 \\
0 & 0 & 0 & 0 & 0 & 0 & 1 & 0 & 0 & 0 & 0 & 0 & 0 & 0 \\
0 & A_f \cos\varphi_{Zx} & 0 & \cos\varphi_{Zx} & 0 & 0 & 0 & \cos\varphi_{Xx} & 0 & 0 & 0 & \cos\varphi_{Yx} & 0 & 0 \\
\cos\varphi_{Zy} & 0 & 0 & 0 & \cos\varphi_{Xy} & 0 & 0 & 0 & \cos\varphi_{Yy} & 0 & 0 & 0 & 0 & 0 \\
0 & 0 & 0 & 0 & 0 & 0 & 0 & 0 & 0 & 1 & 0 & 0 & 0 & 0 \\
0 & 0 & 0 & 0 & 0 & 0 & 0 & 0 & 0 & 0 & 1 & 0 & 0 & 0 \\
0 & A_f \cos\varphi_{Zy} & 0 & \cos\varphi_{Zy} & 0 & 0 & 0 & \cos\varphi_{Xy} & 0 & 0 & 0 & \cos\varphi_{Yy} & 0 & 0 \\
0 & 0 & 0 & 0 & 0 & 0 & 0 & 0 & 0 & 0 & 0 & 0 & 1 & 0 \\
0 & 0 & 0 & 0 & 0 & 0 & 0 & 0 & 0 & 0 & 0 & 0 & 0 & 1
\end{bmatrix}
$$

4.7.2 Matrix combination

Adopting the TMM to model a hydraulic circuit requires the integration of field transfer matrices and point transfer matrices. The field matrices of pipes and hoses express the forces and displacements at one section of the structure in terms of the corresponding forces and displacements at an adjacent section [56, 57]. The point matrices, which express the relation of the two sides of the discrete locations, include structural discontinuities such as supports, mass or bend and fluidic discontinuities like the accumulator and orifice.

The entire transfer matrix of the whole system can be developed by combining the field transfer matrices and point transfer matrices. The relation is shown in Equation 4.71, in which **P** represents the point matrix, **F** indicates the field matrix, **S** stands for the state vector, and **C** is the matrix of accumulative friction and damping. After applying boundary conditions, the rank of system transfer matrix **T** is reduced and this derives a new matrix, which can be named **TT**. The content of this matrix depends on the original matrix **T** and the boundary conditions. The natural frequencies of the system can be found when the determinant of the new matrix (**TT**) is equal to zero. The modal shape of a certain frequency is obtained by substituting the frequency back to Equation 4.71. Figure 4.9 presents a flow chart to describe the algorithm of searching the required results.

$$\mathbf{S}_N^R = \mathbf{T}\,\mathbf{S}_1^L + \mathbf{C} \qquad \text{where} \qquad \mathbf{T} = \mathbf{t}_{N-1}^{-1}\mathbf{P}_N\left(\prod_{i=N-1}^{1}\mathbf{F}_i\,\mathbf{P}_i\right)\mathbf{t}_1 \qquad \text{(Equation 4.71)}$$

$1, i, N$ nodal number

With boundary conditions, Equation 4.18 is derived from Equation 4.17.

$\mathbf{TT}\,\mathbf{S}_1^L = 0$ where **TT** new derived matrix with reduced rank

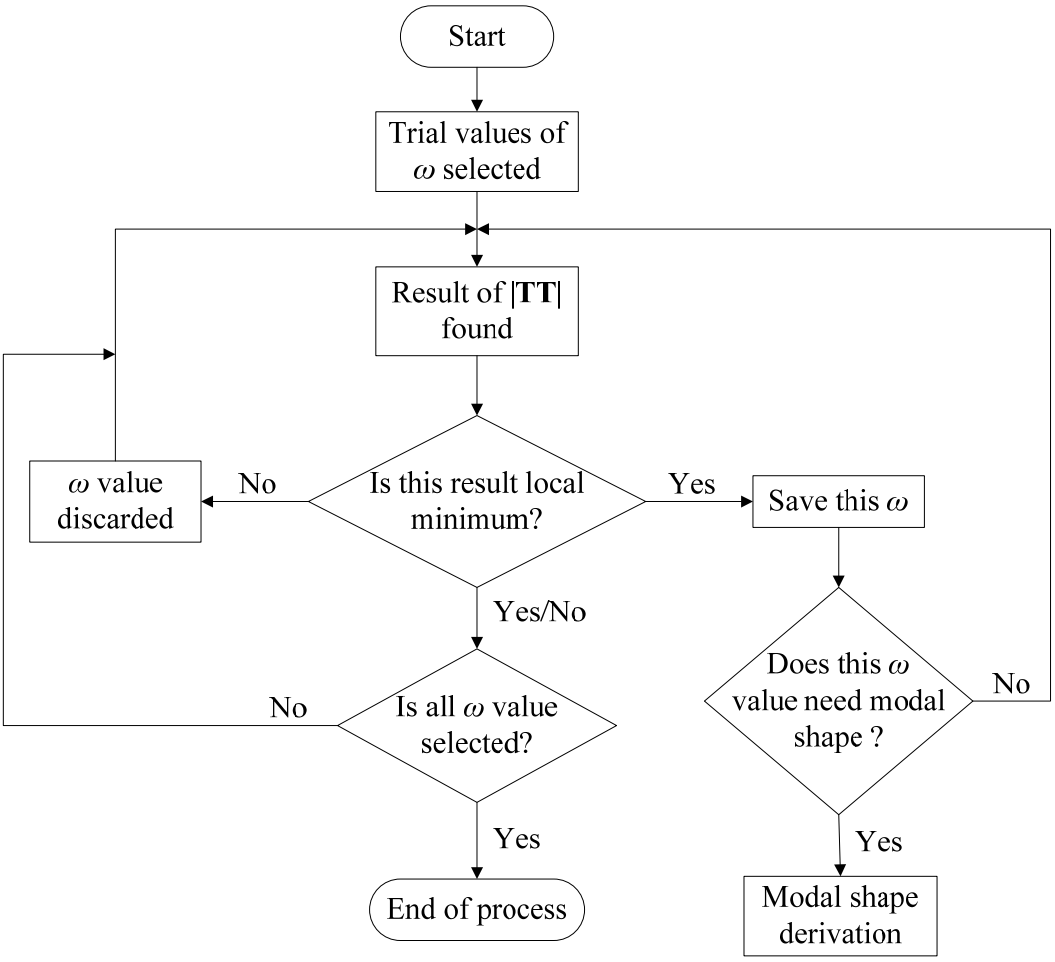

Figure 4.9 Flow Chart of Result Searching Algorithm

4.8 Concluding Remarks

The mathematical representations of pipes, hoses, structural discontinuities and fluidic discontinuities are described and derived in this chapter. The methodology of establishing element models and system models are presented and discussed. The newly developed matrices expand the contents of the TMM employed in the research system.

The friction and damping effects are considered on the basis of a conventional one dimensional model of the straight pipe element. For the lateral directions, the confusion of signs is identified by applying Timoshenko's beam theory to derive the governing equations. During the process of deriving the pipe element model, the errors of research references are corrected.

The developed models of hoses, valves, and accumulators provide the extended understanding of fluid structure interactions in hydraulic piping systems. Although the assumptions of the models are relatively simple compared to actual situations, the requirements of this research are satisfied and the models can be applied to similar systems.

Chapter 5

SYSTEM EXPERIMENTS

The system experiments are employed to validate the model outlined in the previous section. In this chapter, the configuration of experimental apparatus and the process of the tests are described and presented; the remarkable notes and data acquisition are notified; and the factors that influence the experiments are discussed. The content includes an illustration of the hydraulic circuits installed on a test rig, an introduction to utilised data acquisition equipment, including the hardware and software, a description of experimental procedures, and sources of experimental errors.

5.1 Test Rig

5.1.1 System installation

Figure 5.1 is a schematic diagram that illustrates the hydraulic circuits equipped on a test rig. Figure 5.2 and 5.3 show the photos of the test rig used in this research. This test rig was designed at the University of Technology, Sydney (UTS). A number of tests are conducted on the two different hydraulic circuits of the test rig to experimentally determine the system characteristics over a particular frequency range of interest (being less than 1500 Hz).

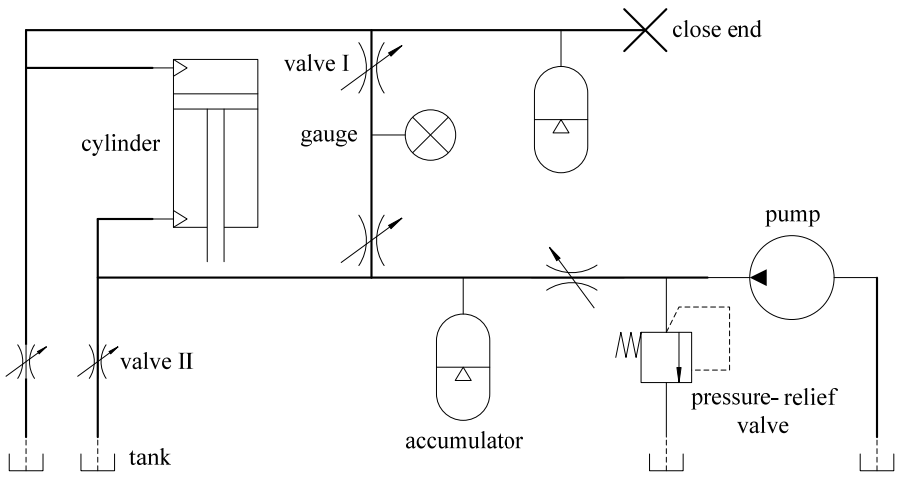

Figure 5.1 Schematic Diagram of Hydraulic Circuit

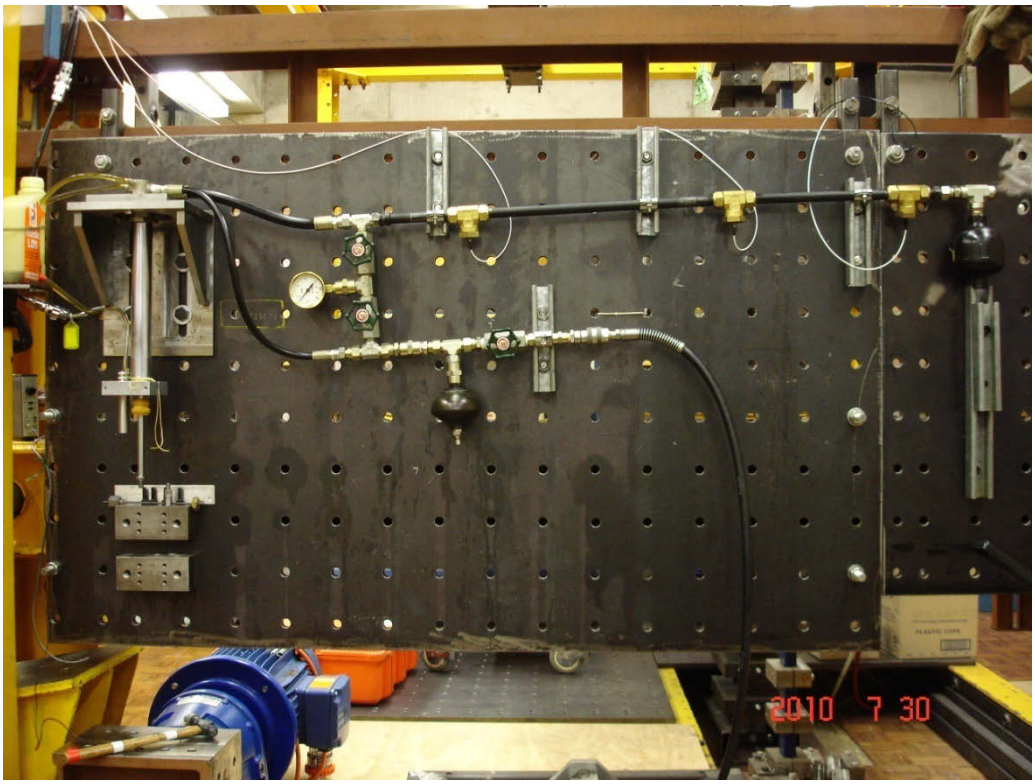

Figure 5.2 Photo of Test Rig (Frequency Test of Hydraulic Circuit 1)

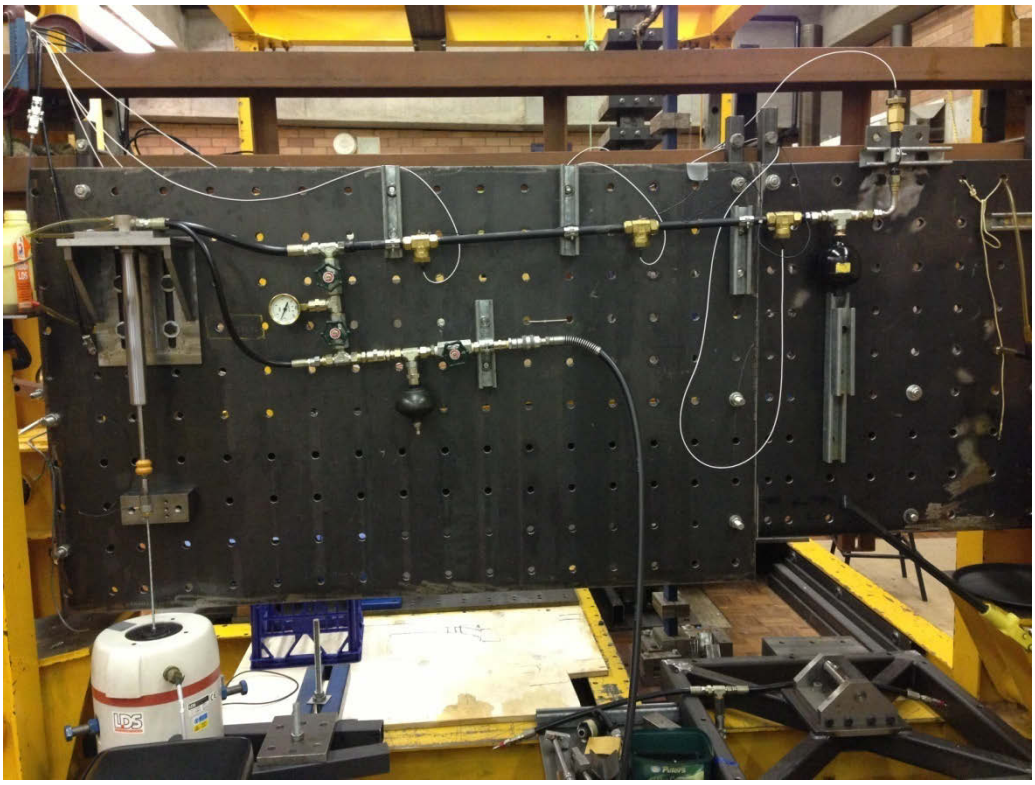

Figure 5.3 Photo of Test Rig (Modal Shape Test of Hydraulic Circuit 2)

As displayed in Figure 5.2 and 5.3, the two circuits installed on the test rig basically consist of a double acting hydraulic cylinder located at the left, two nitrogen-filled diaphragm-type hydraulic accumulators, a pressure gauge in the middle branch, two kinds of blocking valves, several pressure transducers, hydraulic hoses, and steel pipes. Both of them include two lines, an upper line and a lower line. One side of the upper line is linked to the upper chamber of the cylinder and the other side is closed by a metal plug or a pressure transducer. The lower line is linked to the lower chamber of the cylinder on one side and the pump on the other side.

The experiments are performed on the upper line and the lower line serves to settle the test conditions of the upper line. The experiments involve two types of piping circuits: one is a straight pipeline, and the other is an L-shaped pipeline. Both consist of pipes, pressure transducers, accelerometer transducers, a hose and an accumulator. The experimental lines are fixed on the test rig by supports. The circuits are filled with hydraulic oil and the upper lines are separated from the lower ones by blocking valves that are completely hermetic. The ends and joint positions of the pipelines are sealed by geometric structures (i.e. slope surface) or physical materials (i.e. sealing tape).

5.1.2 System pressurisation

According to Figure 5.1, the two lines connect to an oil tank and the tank is connected to the pump by plastic pipes (see Figure 5.2 or 5.3). The tank is separated from the circuits by type II valves. For the experiments in this research, the test circuits needs to be pressurised. When the pipeline is installed on the test rig, type I and II valves are opened and the metal plug is loosened at the close end. The pressure-relief valve is closed before hydraulic oil is pumped into the pipeline.

The phenomenon of pipeline cavitations is not considered in this research, thus air bubbles need to be removed from the systems in the experiments. In order to achieve this, the pipes are tapped when the oil is pumped through the whole circuit. During this process, the pressure in the circuits is equal to the atmospheric pressure. Since the ends of the upper pipeline are slightly higher than the other positions (shown in Figure 5.2 and 5.3), the bubbles move towards the ends when the oil moves around the pipelines. When there are no bubbles shown in the plastic pipes and the close-end position, the type II

valves are closed and the metal plug is tightly screwed. As a consequence, the influence of air bubbles can be ignored.

Oil continues to be pumped into the pipelines. The internal pressure begins to increase and the value of the pressure gauge is changed. The type I valves are closed when the system pressure achieves the purpose. It needs to be noted that the gauge value is the relative pressure, thus the absolute pressure is the gauge value plus the atmospheric pressure. The upper line is separated to other parts of the system at this stage and various experiments can be performed on this line. The pump and valves used in this test rig are all manually operated.

The pre-pressure of the experimental circuit is the gauge value plus the atmospheric pressure. The gauge value is influenced by the fluid in the vertical pipe. The amount of fluid in this pipe is changed by opening and closing the two type I valves and this strongly impacts on the internal pressure. Therefore, the method of closing the type I valve is in accordance with its distance to the pump, i.e. the valve I nearest the pump is closed first, then the one under the gauge, and finally, the one near the upper line. In order to obtain the accurate value of pre-pressure in the experimental line, the gauge value is recorded before the last type I valve is closed. At this point, the pressure gauge only measures the pressure of the upper line.

5.2 Experimental Instruments and Data Acquisition

5.2.1 Hardware

5.4a Data Acquisition Module

5.4b Pressure Transducer

5.4c Accelerometer Transducer & Amplifier

5.4d Hammer

5.4e Force Transducer & Amplifier

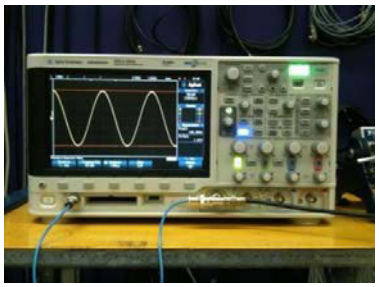

5.4f Digital Storage Oscilloscope

5.4g Power Amplifier

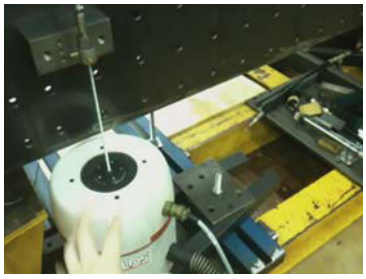

5.4h Force Transducer & Shaker

5.4i Shaker Blower

Figure 5.4 Experimental Instruments

Figure 5.4 shows the photos of Experimental instruments used in the tests. Photo 5.4a is a compact data acquisition module that acquires test data from all types of transducers and transfers the data to the computer. The module applies the IEPE (Integrated Electronics Piezo Electric) standard that ensures compatibility with the equipment of many manufacturers.

Photo 5.4b is a pressure transducer and Photo 5.4c is an accelerometer transducer with its amplifier. Photo 5.4d is an experimental impact hammer, in which a force transducer is incorporated. Photo 5.4e is a single force transducer with an amplifier. This instrument is applied for the modal shape tests. All the transducers transform electric voltage signals into the measurement data that are transferred to the computer and a particular software is employed to process the original data.

Photo 5.4f is a digital storage oscilloscope that is employed as a wave generator in the modal shape tests. It is connected with a power amplifier displayed in Photo 5.4g. The signal of harmonic waves under certain frequencies can be generated by the oscilloscope and it is amplified before being applied to drive a shaker shown in Photo 5.4h. The physical vibrations are excited by the shaker and then drive the piston to form the input of the tests. As shown in this photo, the single force transducer is installed be-

tween the cylinder piston rod and the shaker rod to measure the force changes during the tests. Photo 5.4i is an air blower that is joined to the shaker by a soft pipe and this takes off the heat produced by the working shaker.

5.2.2 Software

The data acquisition module is a product of National Instruments (NI) Corporation, which is an American company which operates on a global scale. The pressure transducers are connected to the module directly. The accelerometer transducers and the force transducer are connected to the module through amplifiers. The acquired signals of all the transducers are electric voltage values. These signals need to be transformed to the relevant International Unit (IU) for A/D converting. The module is connected to a computer with a USB port and this transfers the measured digital data. Software named Measurement & Automation Explorer is installed in this computer to perform the transformation. Figure 5.5 shows the interface of the software.

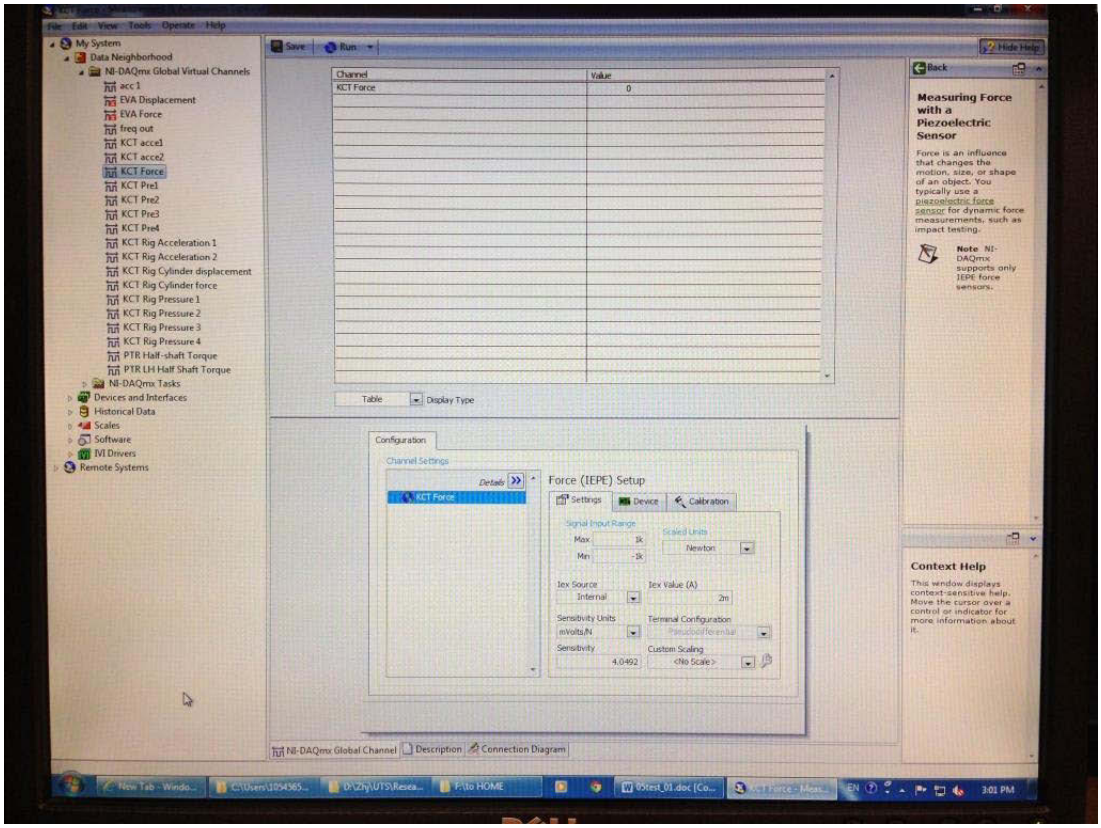

Figure 5.5 Measurement & Automation Explorer Interface

For every transducer, the transforming relationship between the voltage signal and the relevant IU is unique, and this even applies to the same model transducers. For example, the pressure transducers are of the same model and they all have proportional coefficients between the voltage and the IU (MPa). The value of their coefficients is about 0.7, but for each transducer this value is a slightly different. They are 0.7077, 0.7003, 0.6925, and 0.693 respectively. This NI software is employed to set up the relationship for each transducer according to the sensitivity parameters offered by its manufacturer. This procedure eliminates errors in the acquired data due to the technical differences of the transducers and it ensures that the test data operates according to the same criteria.

Once the test data prepared by the NI software is ready, it can be analysed by LabVIEW. As discussed in Chapter Three, LabVIEW is widely used to develop experimental applications and to interface with measurement and control devices. It provides the unique graphical programming language to perform these functions. Figure 5.6 displays the LabVIEW interface of the modal shape test and its graphic programme. The measured data e.g. trigger strength, pressure response, accelerometer response and frequency response functions and excitation frequencies, amplitudes and phase differences of modal shape tests can be shown through the LabVIEW software.

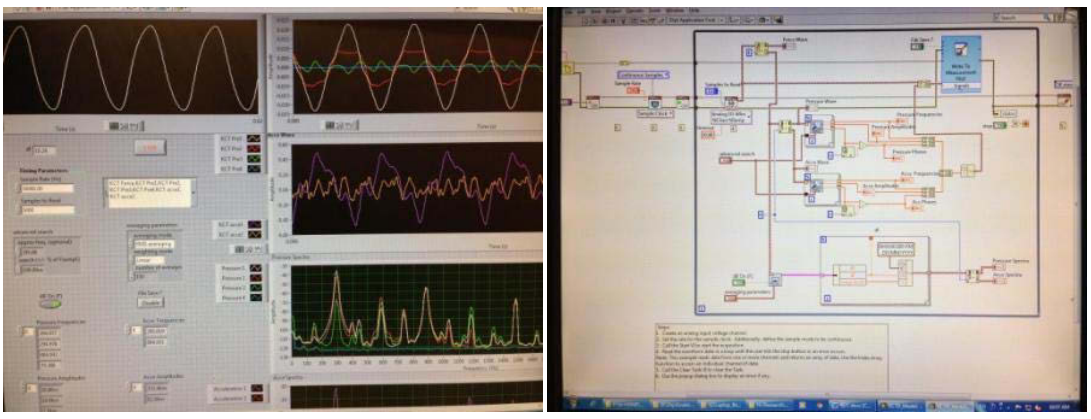

5.6a Experimental Interface 5.6b Graphic Programme

Figure 5.6 NI LabVIEW

The two software programmes and the data acquisition module are made by the NI Corporation. Therefore, the test data is transformed, transferred and processed between the same series of products, which reduces the inter-transformation steps, decreases internal errors and increases the reliability and the processing speed.

5.2.3 Experimental data acquisition

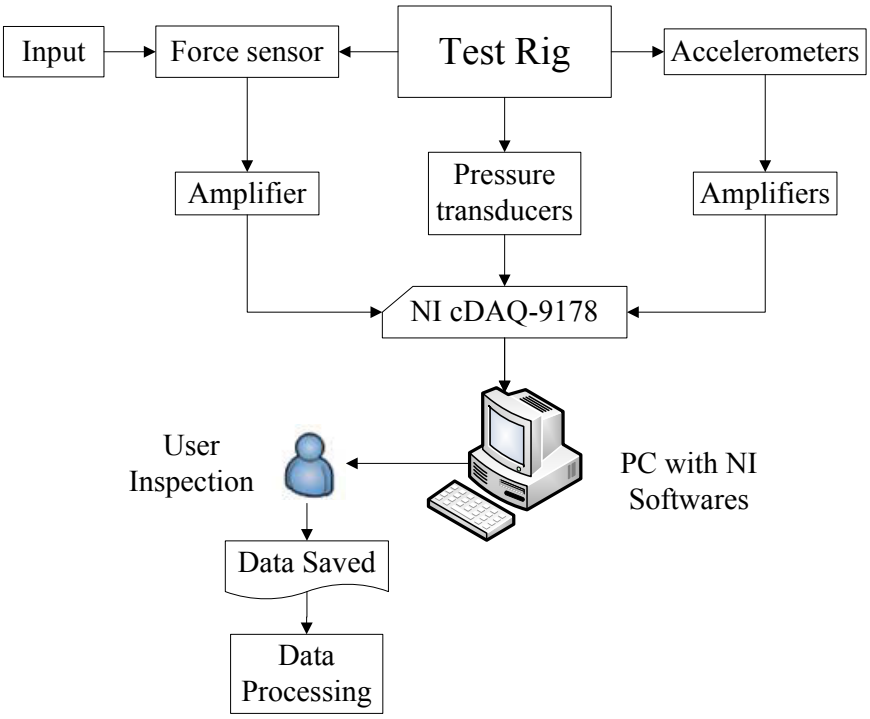

Figure 5.7 Flow Chart of Test Rig Data Acquisition

A diagram of the test rig data acquisition layout is shown in Figure 5.7. The data recorded are the input force signal, response pressure and acceleration signals. Table 5.1 gives the technical specifications of the transducers used in the experiments. The signals from the transducers are sent to a PC that is equipped with an NI data acquisition card (model NI cDAQ-9178). The force and acceleration signals go through separate amplifiers (Dytran 4705M5 and 4705M4, respectively) before they reach the card. The NI software, installed in the PC, graphically displays both time and frequency domain information and allows the user to inspect the data before saving it. The measured data is processed to provide the required information for the subsequent analysis.

Table 5.1 Technical Specifications of Transducers [123]

Transducer	Manufacturer	Model	Measuring range	Sensitivity
Force transducer	Bruel & Kjaer	8201	4000 N	3.69 pC/N
Pressure transducer	PCB Piezotronics	111A26	3448 kPa	0.07 kPa
Accelerometer transducer	Bruel & Kjaer	4344	20000 g	2.66 mV/g

5.3 System Natural Frequency Identification

The experiments that are used to identify the system natural frequencies are frequency response tests. In the tests, the bottom of the cylinder piston rod is knocked by a hammer at the vertical direction and one upward hit is an input signal of a test. The response signals come from the pressure transducers and accelerometer transducers. The frequency response function of the system vibration is obtained by dividing the spectrum of the output signal by that of the input signals, as shown in Equation 5.1.

$$\text{Frequency response} = \frac{\text{Output signal spectrum}}{\text{Input signal spectrum}} \qquad \text{(Equation 5.1)}$$

Figure 5.8 displays the NI LabVIEW interface of the frequency response tests. The four figures show the trigger force, pressure response, accelerometer response, and the frequency response. The vertical axes illustrate the magnitude of each signal. The first figure is the trigger signal produced by the hammer hit. Its horizontal axis is the sample rate of the tests. The second figure is the pressure response signal at the time domain; and the third figure is the accelerometer response signal. The horizontal axis of these two figures is the time range, which is 0.2 seconds. The last figure displays the frequency response spectra of every transducer, which are the magnitude of the frequency response versus the frequency range (i.e. the horizontal axis).

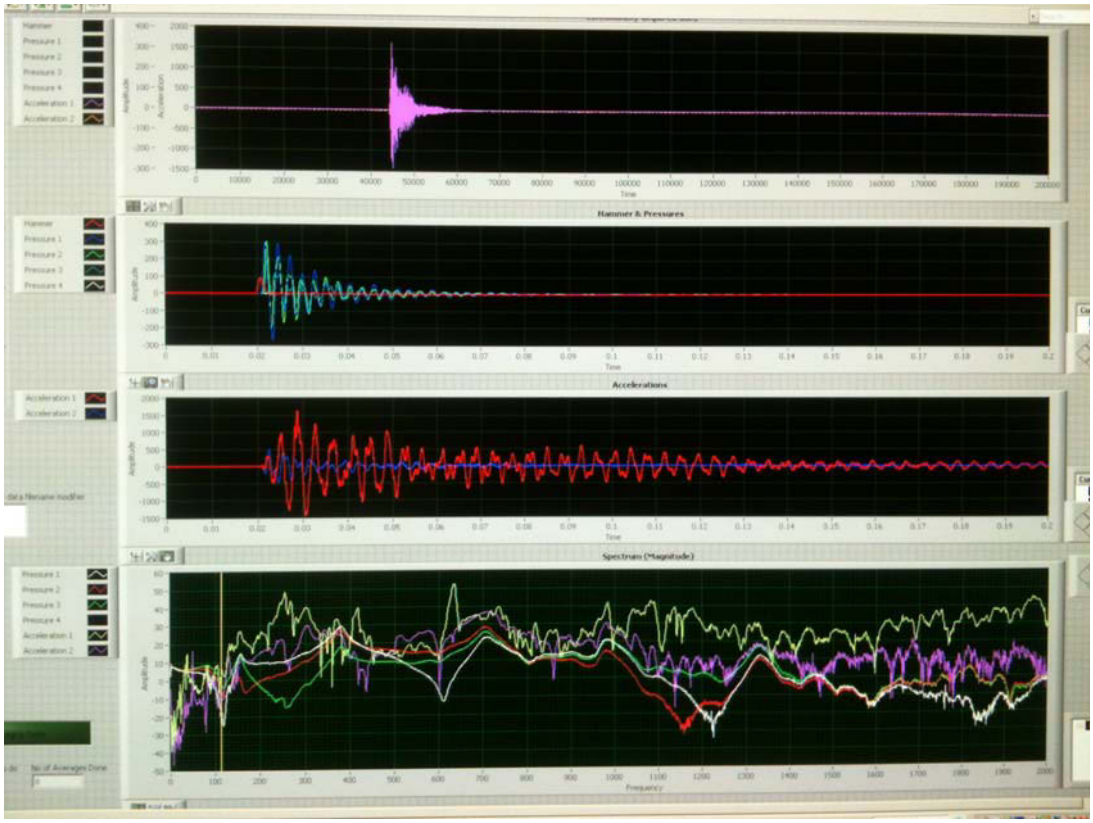

Figure 5.8 Interface of Frequency Tests

In order to improve the accuracy of the results and decrease the effect of noise, a number of the same tests are performed and the average result is obtained. From Figure 5.8, it can be seen that the vibration induced by the hammer hit lasts a very short time and the fluidic and structural responses last longer. Therefore, the intervals between every hit are about one second and this provides enough time for the vibrations of the system to settle down.

In these experiments, Equation 5.1 is used to calculate a series of frequency response spectra for each hammer hit. Integrating all the spectra, the average spectrum is obtained. This average method can be performed only in the frequency domain. For the experiments which serve to identify system natural frequencies in this study, the data were processed in the frequency domain.

The frequency spectrum acquired from the signal processing of NI LabVIEW is influenced by number the hammer hit, i.e. the average times. Figure 5.9 illustrates the frequency spectra of different average times. The signals from an accelerometer transducer and a pressure transducer were analysed and compared. The purple lines represent the

results with thirty average times; the yellow lines show fifty average times; and the blue lines show one hundred average times.

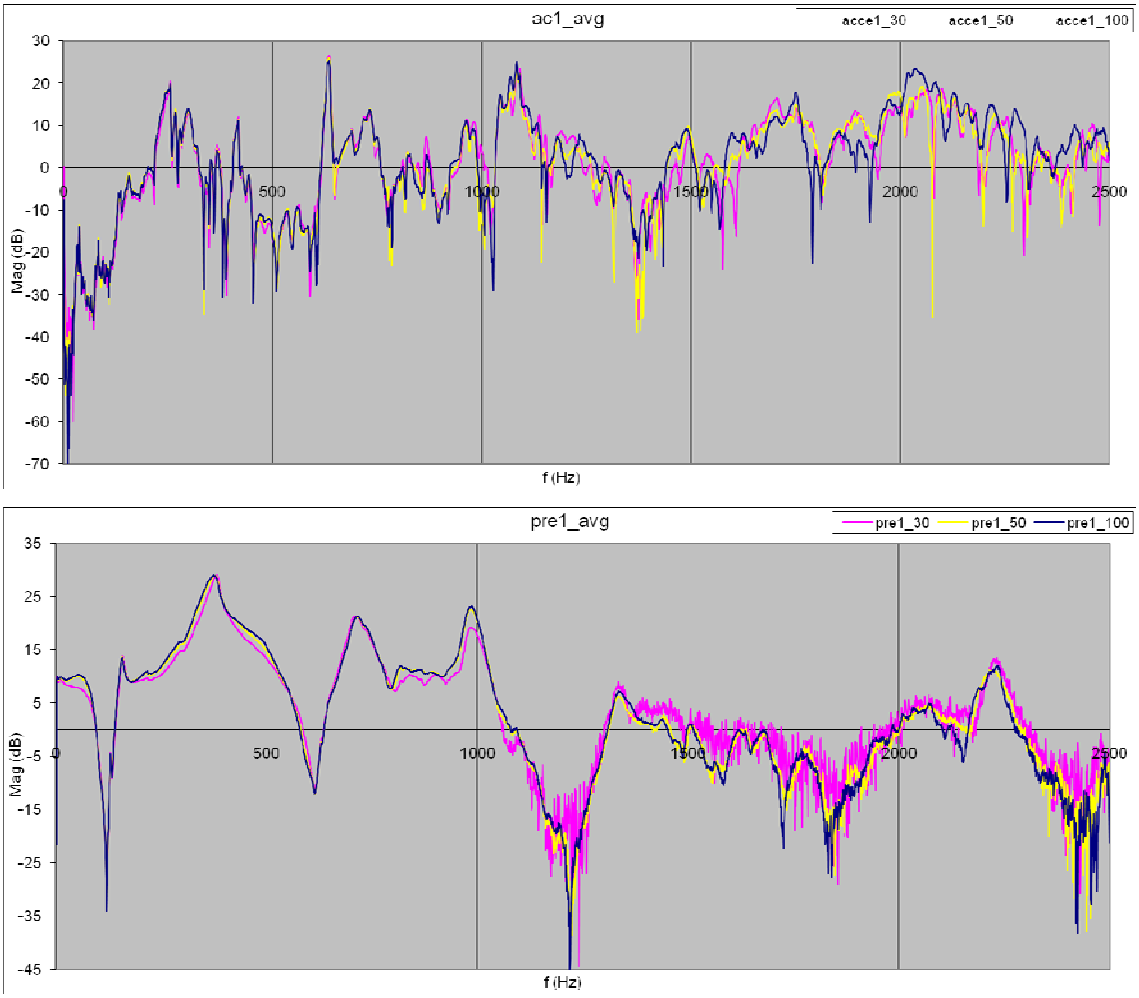

Figure 5.9 Frequency Spectra of Different Average Times

It can be concluded that increasing hit times can reduce the effect of noise, especially at the high-frequency range. However, the higher average times result in a longer period for the test. According to the figure, the curve of fifty times is quite smooth and the peaks are clear, therefore the fifty times average is adopted as the average hammer hit number in the experiments.

Some hammer hits fail because they are too mild or they hit the wrong position. All these hits cannot achieve the required strength, thus the LabVIEW is set to ignore such hits. The NI LabVIEW acquires each hit signal at a certain period. If a hammer hit is missed during the recording period, the hit is considered as a failed hit. This type of hit is also skipped by the LabVIEW setting.

The system frequency response measured by the pressure transducers is mainly influenced by the fluid fluctuation in the axial direction. The two accelerometer transducers equipped on the hydraulic circuit 1 (Figure 5.2) measure the axial and lateral signals respectively. One is installed near the middle pressure transducer and it measures the lateral acceleration of the system. The other is installed at the close end and it measures the axial acceleration. For the hydraulic circuit 2 (Figure 5.3), an extra pressure transducer is installed in the system and both accelerometer transducers are in same direction. As the circuit 2 is an L-shaped pipeline, the local coordinates for each straight pipe are different. The second accelerometer transducer measures the axial signal at the local position, but it is on the lateral direction of the other pipe.

5.4 Modal Shape Tests

The modal shape tests measure the response signals at a series of locations on the pipeline under defined frequencies. The sinusoidal wave of a certain frequency replaces the hammer hits as the input signals. Paralleling Figure 5.4, the wave is produced by the digital storage oscilloscope and enhanced by the amplifier. It is also used to drive the shaker that is connected to the bottom of the piston rod. For each interested frequency, the most important factors are the magnitude and phases of the response waves. The NI LabVIEW can record the input signal and all response signals. The response signals are plotted in one chart to produce the modal shape of the frequency (see Figure 6.6 and 6.7).

Figure 5.6a shows the interface of modal shape tests. The left figure represent the input waves, and the first two right figures represent the response waves of the pressure transducers and the accelerometer transducers respectively. The other two figures on the right hand side are the response frequency spectra of the pressure transducers and accelerometer transducers respectively. The amplitude and phases of response waves from all the transducers are shown in the tables on the left hand side.

The input sinusoidal waves should have strong power to resist the noise and external effects. However, according to the restriction of the instruments, the shape of the wave could be changed when the input amplitude is too large. This will lead to unreliable re-

sponse signals. Under this circumstance, choosing the proper wave amplitude is essential. After setting the interested frequency, there are two ways to change the wave amplitude: the first is to adjust the output of the digital storage oscilloscope; the second is to adjust the amplifier. According to the measured wave shown in the LabVIEW, the input wave amplitude is kept on the level that is a little lower than the shape-changing one.

When the input signal settles down, the response signals are recorded after about a half minute, during which time the system can be stabilised. The modal shape information of fluid pressure is directly recorded from the pressure transducers. Unfortunately, the pressure modal shapes of the whole pipeline cannot be produced in these experiments due to the limited number of pressure transducers. However, the relationships between the several points show the partial pressure modal shapes.

For the structural modal shape tests, we can set up a number of the same model accelerometer transducers along the pipeline and the response signals from these transducers can be acquired. However, the added transducers increase the mass of the pipes even though each one is small. Although the accelerometers are light compared to the pipeline, they still change the configuration of the system and consequently change the condition of the tests.

In the modal shape tests, only two accelerometer transducers are employed, one is the reference transducer and the other is the mobile transducer. By moving the mobile transducer along the pipeline, the response signal of each position is recorded. The modal shapes of the pipeline can be derived by combining all the measured responses. Again, a half minute is needed after each movement to wait for the steady state of the system.

5.5 Influence Factors

The experiments are influenced by various factors, such as temperature, noise, instruments, test methods, and human factors. The effects of these factors are described and discussed in this section.

5.5.1 Circumstance and instruments

The increased temperature results in the enhanced pressure that affects the system natural frequencies, thus the room temperature influences the measured results. The experiments are performed at the laboratory with central air conditioning, in which the room temperature is stable. The noise may affect the experimental results, especially for noise which is under a regular frequency. Since the source of noise is numerous, it is very difficult to predict and/or eliminate the influence of noise. However, the amplitudes of noise are much lower than the measured signals and its impact can therefore be ignored. The experiments can also be performed at times where there is no noise.

Although some bigger accelerometer transducers have higher measuring qualities, the accelerometer transducers used in these experiments are types of small transducers which weigh about five grams. The reason for selecting small ones is to reduce the influence of the transducers' mass on the system characteristics. Especially for the modal shape tests, the mobile transducer actually changes the system configuration at each move. The small accelerometer transducers can minimise these effects. The extra glue that is used to stick the accelerometer transducers on the pipelines also has some effect on the experiments.

Some experiments are performed by using two sets of instruments. The measuring results are influenced by the instrument difference. Table 5.2 shows the frequency results of the straight pipeline, which are measured by pressure transducers for the straight pipeline. It can be concluded that the difference is not very large, but it is obvious. Therefore, the change of instruments actually affects the measuring results even if it is for the very same experiment.

Table 5.2 Comparison between Instruments (Pressure Transducer Measurement)

Frequency (Hz)	f_1	f_2	f_3	f_4
Old instruments	128	369	700	992
New instruments	132	388	711	990

5.5.2 Human factors

There are some human factors that can influence the measuring results. With the blower, the shaker applied at modal shapes tests is heated during the experiments, especially at low-frequency tests. In order to avoid the overheating of the shaker, some modal shape tests need to be interrupted. Since the amplitudes of the vibrations in these tests are adjusted by hand, the output amplitudes are different before and after the interruption. Therefore, the measured modal shapes can have small errors.

Another factor is the mobile accelerometer transducer. While performing the modal shape tests, the mobile transducer is moved by hand. It is planned that the transducer measures the lateral signal for each position. However, when it is moved, the position and direction of this transducer may not always be at the exact place and this can influence the measurements.

5.5.3 Experimental methods

Different experimental methods lead to different measured results. A new method of the frequency tests is attempted after finishing all the experiments. A "*sine sweep*" is used as the input signal to replace the hammer hits. The term means the input signals are sinusoidal waves and the frequencies are from a lower value to a higher value. The sine sweep is generated by the digital storage oscilloscope. The system configuration is similar to the one in the modal shape tests.

Figure 5.10 compares the frequency spectra of different input methods by using the measured signals of an accelerometer transducer and a pressure transducer. The blue lines display the results of the hammer hit method; and the red lines represent the results of the sine sweep method. It can be concluded that with the sine sweep method, the response signals are more distinct. Due to limitations of time and equipment, this method is not employed in this research. However, it can be considered as an improved method for further studies.

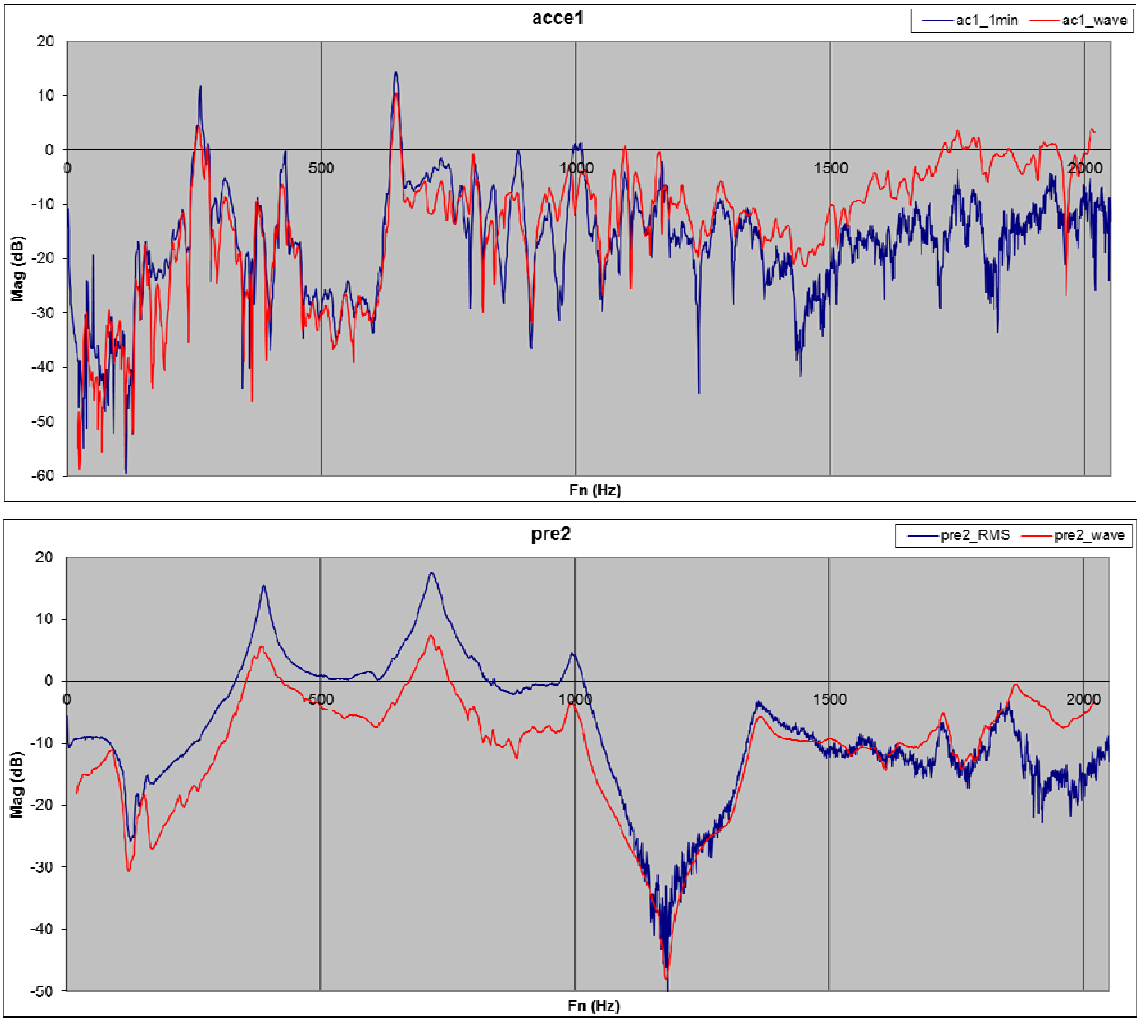

Figure 5.10 Comparisons of Hammer Input and Sine Sweep Input

5.6 Concluding Remarks

The experiments of measuring system natural frequencies and modal shapes for two pipelines are described in this chapter. The piping systems are settled on a university-established test rig. The configurations of the test rig and the experimental equipment are introduced and described. The usage and performance of test instruments and software are presented. The data acquirement process is illustrated by a flow chart.

The procedures of the experiments are explained and the remarkable features of performing the tests are distinguished. The test preparation step is to pre-pressurise the pipeline and remove air bubbles from the system. During frequency tests, the certificated hits are identified and counted; and the average times show its impact on the experimental results. For the modal shape tests, the instruments can be improved to in-

crease the accuracy and content of the results.

The factors that influence the measuring results are also discussed in this chapter. Some circumstantial factors can be controlled and others cannot. The experimental instruments are selected by considering the effects on system configurations and their sensitivities. A new experimental method for the frequency test is offered and compared to the one applied in this research. Since it shows better results, it could be viewed as a viable methodological alternative for future work.

Chapter 6

RESULTS COMPARISON AND VALIDATION

This chapter presents the simulation of the test pipelines. The mathematical simplification is described and the system parameters of the simulation model are selected. In this chapter, the calculation results are compared with the experimental results. The proposed models are then verified according to the comparison.

6.1 Mechanical Parameter of Simulation Model

6.1.1 Model assumption

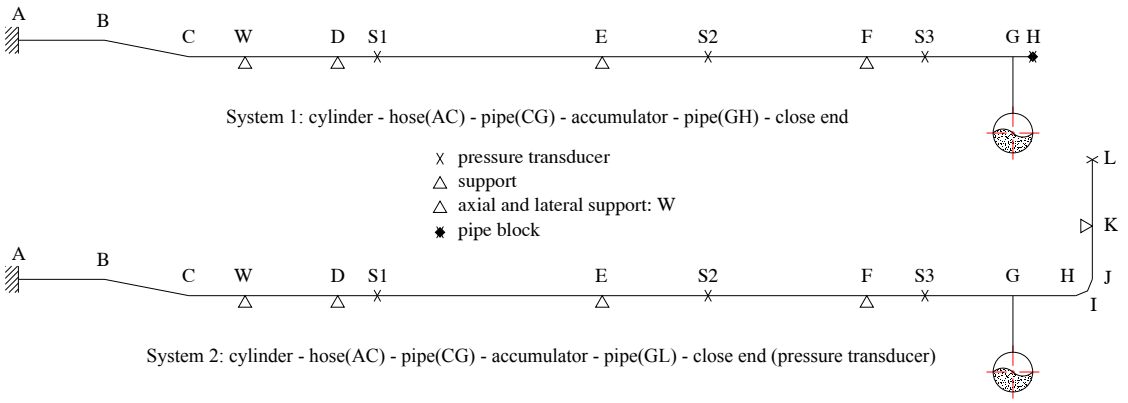

Figure 6.1 Simulation Model of Test Rig

Figure 6.1 illustrates the two experimental pipelines of the test rig. The hose (AC) is divided into two straight-hose elements joined by a hose bend. The elbow (HJ) is simplified as two curved-pipe elements; and the others are straight-pipe elements. The branch at Point W is regarded as a two-direction support. The other supports are only on the lateral direction. All fluidic and structural discontinuities are considered as non-dimensional points.

As shown in Figure 5.1, the pipelines connected with the two chambers of the cylinder are separately blocked at the other ends. The volume of the lower chamber is slightly

smaller than the upper chamber's volume due to the piston rod, thus the pressure force at the upper cylinder is a little higher than the lower cylinder's pressure. Therefore, the piston is moved towards the bottom end of the cylinder when the system is pressurised and there is almost no movement of the piston during the experiments.

The pipeline linked to the upper chamber is the one on which the experiments are performed. By considering the cylinder as a rigid body, the left boundary condition of the pipe is simplified as the fixed end. Since the filled liquid is regarded as incompressible fluid and the oil in the cylinder is almost at a standstill, the left boundary of fluid is assumed as the closed end. For the right boundary condition, there is no constraint and the pipe is blocked, thus it is the free and closed end.

6.1.2 Mechanical system parameters

The hydraulic circuit is pre-pressurised for all the experiments. The pressure of each test is recorded and the value is about 3~3.2 million Pascal. The steel pipe is employed in the experiments. The physical properties of the pipe are outlined in Table 5.1, where the average density and Poisson's ratio values are given.

Table 6.1 Physical Properties of Pipe [56, 124-128]

Property	Value
Inner diameter	0.0165 (m)
Thickness	0.0012 (m)
Density	7850 (kg/m^3)
Young's modulus	207×10^9 (Pa)
Shear modulus	79.3×10^9 (Pa)
Poisson's ratio	0.3

The experiments involve the Gate hydraulic hose (Gates 8M4K-STF), which is the Nitrile based hose reinforced by two braids of high tensile steel wire. Some of the physical properties of the hose can be found in the manual of the manufacturer. As the hose consists of two kinds of materials (Nitrile and steel wire), the value of the properties is determined by considering the combined influence. Table 6.2 shows the hose properties

used in this research. The radius of reinforcement is considered at the middle of the hose wall, i.e. $r_r = \frac{(r_i + r_o)}{2}$.

where

r_i is inner radius of hose wall

r_o is outer radius of hose wall

Table 6.2 Physical Properties of Hydraulic Hose [74, 84, 128-131]

Property	Value (Nitrile)	Value (steel)	Combined value (steel wire)
Inside diameter	0.0127 (m)		
Outside diameter	0.0208 (m)		
Density	1×10^3 (kg/m^3)	7.9×10^3 (kg/m^3)	1.5×10^3 (kg/m^3)
Axial Young's modulus	$10\sim20\times10^6$ (Pa)	200×10^9 (Pa)	1.5×10^9
Lateral Young's modulus	$3\sim5\times10^6$ (Pa)	200×10^9 (Pa)	1×10^7 (Pa)
Shear modulus	1.2×10^6 (Pa)	79.3×10^9 (Pa)	3.5×10^6 (Pa)
Axial Poisson's ratio	0.5	0.3	0.35
Lateral Poisson's ratio	0.5	0.3	0.45

The liquid used in the experiments is a synthetic fluid (fluide LDS). According to previous study [12] and the information from the manufacturer, the properties are listed in Table 6.3. The properties of the accumulator (Hydac SBO 210) used in the experiments are obtained by reading the content printed on the accumulator and measuring the actual equipment. The values are shown in Table 6.4. Since the accumulator is equipped in the pipeline with joints, the mass of the accumulator is assumed to be 2 kilograms.

Table 6.3 Physical Properties of Hydraulic Oil

Oil property	Value
Density	870 (kg/m^3)
Bulk modulus	1400×10^6 (Pa)
Viscosity	0.05 (N s/m^2)

Table 6.4 Physical Properties of Hydraulic Accumulator

Accumulator property	Value
Weight	1.8076 (kg)
Pre-pressure	0.2×10^6 (Pa)
Pre-volume	0.32 (L)
Distance between ball centre and centre line of pipe	0.115 (m)

The weight of concentrated mass, such as pressure transducers and the close end, and the length of pipe and hose sections are measured in the laboratory. The weight of accelerometer transducers is ignored due to their very small mass. The constraints used in this research are simplified as spring supports, and their stiffness is determined by a test. The detailed explanation of the test is described at Section 10.2.

6.2 Results Comparison

For System 1 and System 2, the system natural frequencies and some modal shapes of simulation models are compared with the experimental results in this section. The differences between the results are explained and discussed.

6.2.1 Frequency results

Figure 6.2 shows the frequency response of the simulation model for System 1. The range of calculation frequency is from zero to 450 Hz because the disturbances cover the higher results. Figure 6.3 shows the experimental results of system frequency response for System 1. The results come from two types of transducers: three pressure transducers and a lateral direction accelerometer transducer. Figure 6.3b combines the results of the three tests at different days.

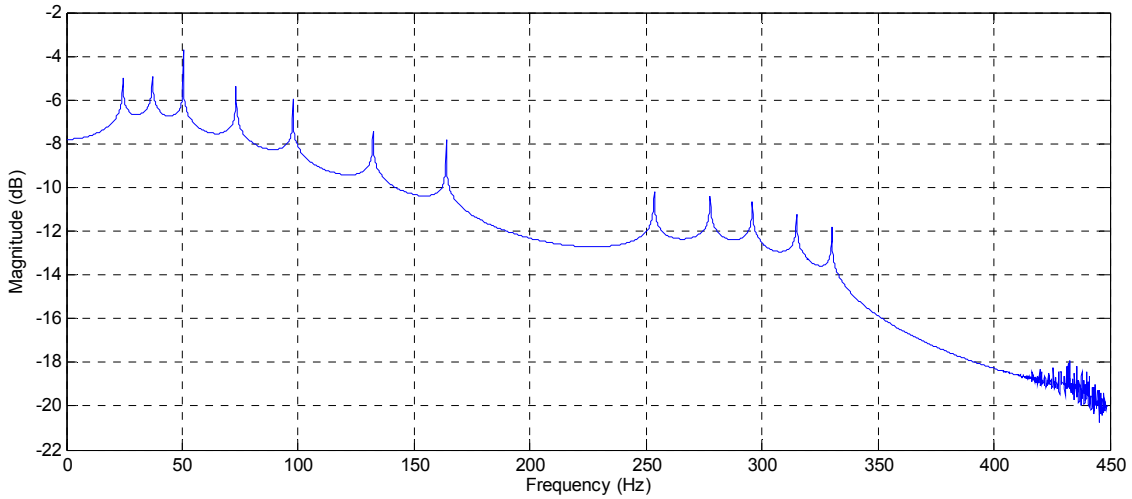

Figure 6.2 Simulation Results of System 1 Frequency Response

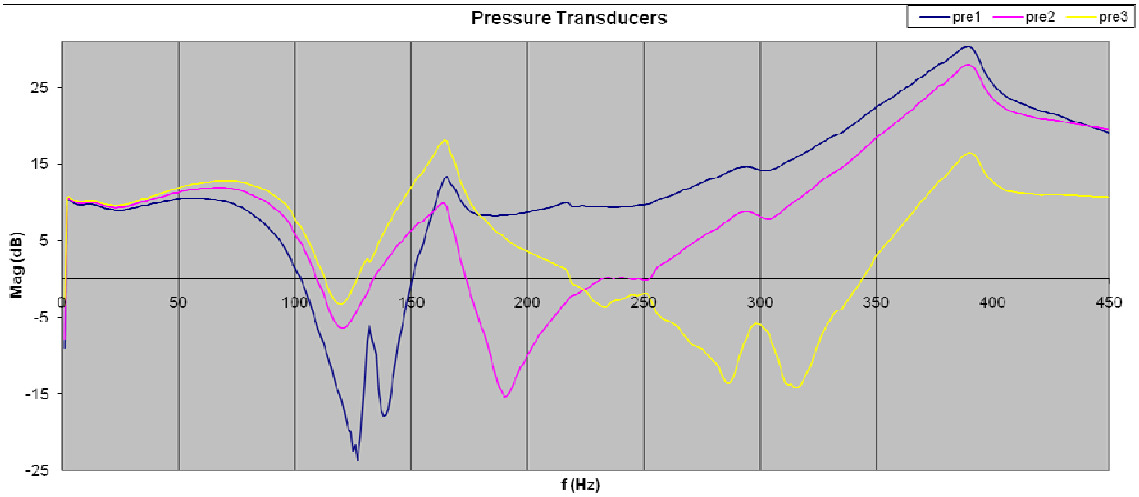

6.3a Results of 3 Pressure Transducers

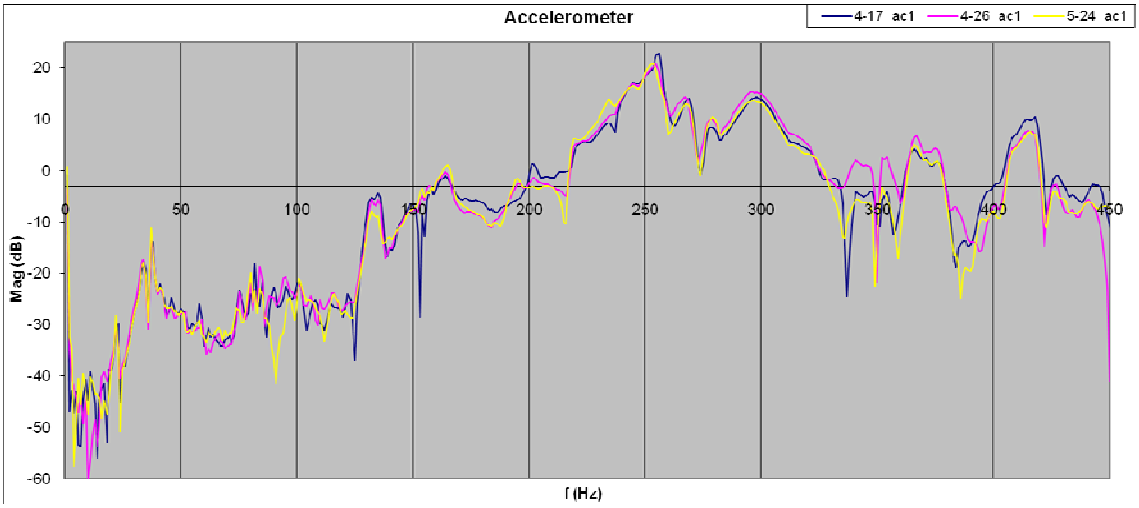

6.3b Results of Lateral Accelerometer Transducer (3 times)

Figure 6.3 Experimental Results of System 1 Frequency Response

According to Figure 6.3, it can be concluded that the pressure transducers cannot measure many structural mode signals, so the frequency peaks displayed in Figure 6.3a are fewer than those displayed in Figure 6.3b. When processing the test data, it is found that the accelerometer transducer cannot measure some fluidic signals. Therefore, the two sets of frequency responses are analysed together to obtain the whole measurement results.

The comparison of the simulation and experimental results is listed at Table 6.5. It can be seen that the results match well with each other. There are some lower frequencies shown in the simulation results that are not found in the experiments. These frequencies should be the structural mode results that are measured by accelerometer transducers. Some low frequencies might be mixed with environmental noise and missed by the accelerometer transducer owing to its very small mass.

Table 6.5 Simulation and Test Results of System 1

Frequency (Hz)		$\mathbf{f_1}$			$\mathbf{f_2}$	$\mathbf{f_3}$	$\mathbf{f_4}$	$\mathbf{f_5}$	$\mathbf{f_6}$	$\mathbf{f_7}$
Simulation results	24.5	37.2	50.5	73.2	97.7	132.3	163.8	253.5	277.7	295.7
Test results		37			95	132	164	254	277	296

Figure 6.4 displays the frequency response of the simulation model for System 2. The range of calculation frequency is from zero to 400 Hz. However, above 300 Hz, the frequency is hardly identified due to the disturbances. Figure 6.5 shows the experimental results of system frequency response for System 2. The results come from four pressure transducers and two accelerometer transducers at different directions.

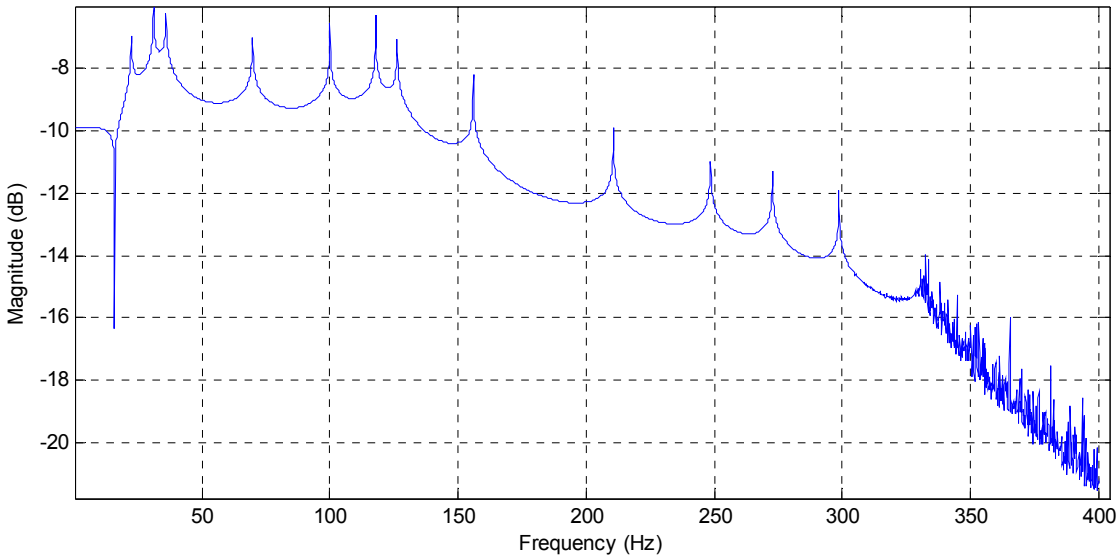

Figure 6.4 Simulation Results of System 2 Frequency Response

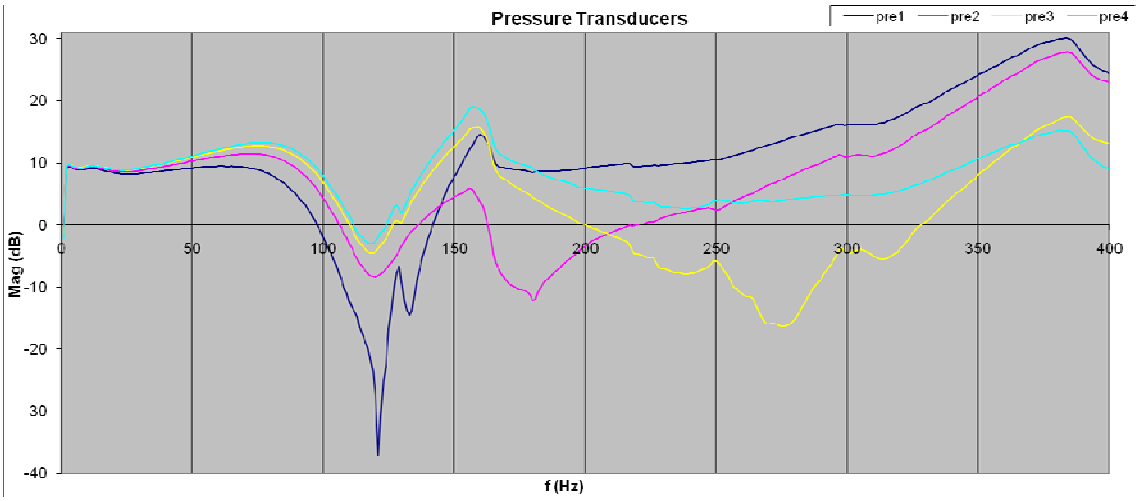

6.5a Results of 4 Pressure Transducers

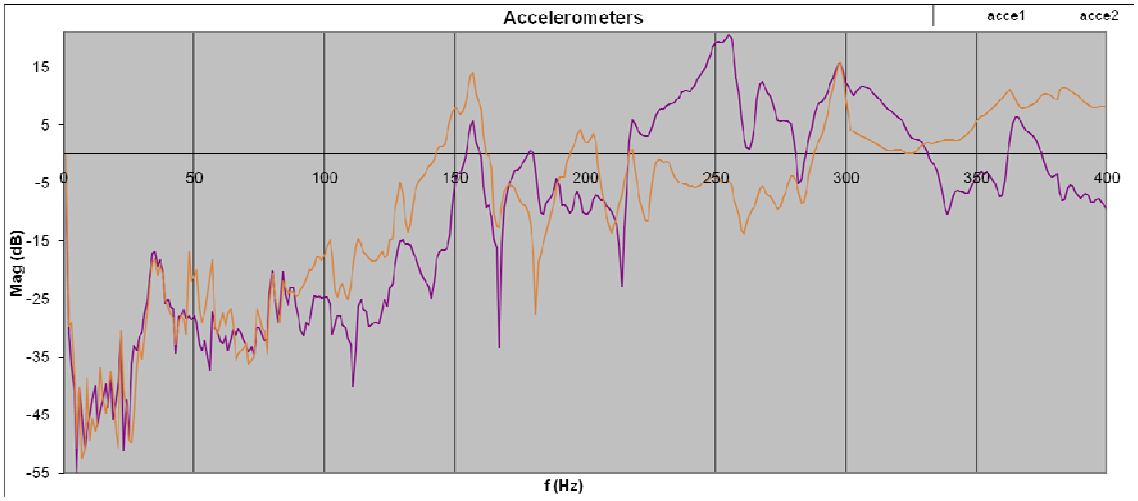

6.5b Results of 2 Accelerometer Transducers

Figure 6.5 Experimental Results of System 2 Frequency Response

The three lines of Figure 6.3b are very close as they are the results of the same transducers only at different test times. Unlike Figure 6.3b, the results shown in Figure 6.5b come from two different accelerometer transducers. For the local position, one of the transducers measures the lateral signals and the other measures the axial signals. As System 2 is the L-shaped pipeline, the axial and lateral vibrations are coupled with each other. Therefore, the responses of the two positions are different although both of the transducers are in a vertical direction. The two lines in Figure 6.5b show the differences.

Table 6.6 lists the simulation and experimental results of the natural frequencies of System 2. The results match each other except at two lower frequencies.

Table 6.6 Simulation and Test Results of System 2

Frequency (Hz)		f_1		f_2	f_3	f_4	f_5	f_6	f_7	f_8	f_9
Simulation results	22.6	35.2	69.7	100.3	118.4	126.2	156.9	237.8	248.8	272.8	298.6
Test results		35		100	114	128	157	237.5	249	268	298

The axial mode frequencies measured by pressure transducers are mainly influenced by fluid dynamics; and those measured by accelerometer transducers are lateral mode frequencies, which are mostly affected by structural dynamics. Some frequencies are measured by both types of transducers, which means that these are fluid-structure coupling frequencies. These frequencies are considered as key frequencies of the system.

The frequencies measured by pressure transducers are found in the simulation results. The measurement by pressure transducers is more reliable than that by accelerometer transducers because the transducers are enclosed by fluid and the outer structures and noise has little effect on them. The higher frequencies relate to the status with less stored energy and the simulation shows the noise results at high-frequency range, thus the discussion in this research focuses on the frequencies lower than 300 Hz.

6.2.2 Result stability

The disturbance in the calculation frequency results of simulation models could come from the phenomenon named "*stiff equation*". In mathematics, a stiff equation is a differential equation in which certain numerical methods used to solve the equation are numerically unstable [134]. The mathematical model derived in this thesis comes from a number of differential equations. If the piping system is investigated only in the axial direction, the results are stable. However, when the lateral direction is analysed with or without the axial direction, the disturbance appears. This means the equations of axial dynamics are not stiff equations, but the lateral equations are.

Another possible reason for the unstable results could be the combined matrix itself. The magnitude of the terms in the axial matrix is much lower than those in the lateral matrices. When the value of the variable "ω" (circular frequency) is increased during the calculation process, the combined matrix tends to be singular. This could be said to cause the problem. Furthermore, this also explains why the disturbance is shown at the higher frequency range.

6.2.3 Modal shape results

Figure 6.6 illustrates the modal shapes of three key system natural frequencies for System 1. The frequencies are influenced by both the fluid and structures, thus the modal shapes of the lateral force and the pressure of some positions are displayed. The pressure modal shapes of the whole pipeline could not be obtained due to the limited signals. There are three pressure transducers incorporated in this pipeline, so the pressure signals on the three points can be acquired and the pressure relationship of the three locations can be obtained.

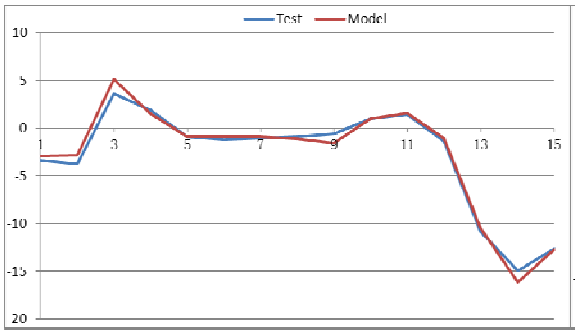

Fig. 6.6a Lateral Force at 132 Hz

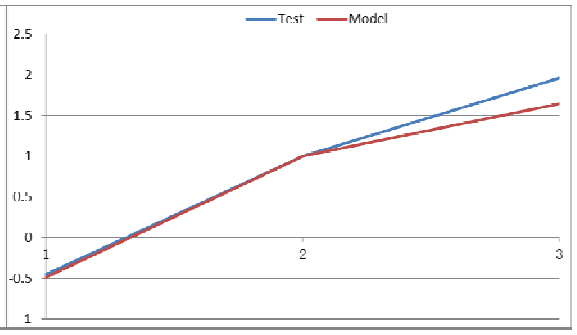

Fig. 6.6b Pressure at 132 Hz

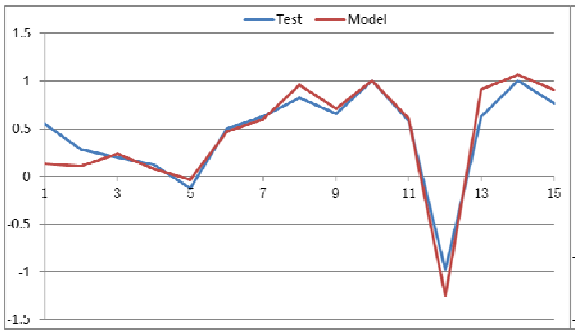

Fig. 6.6c Lateral Force at 164 Hz

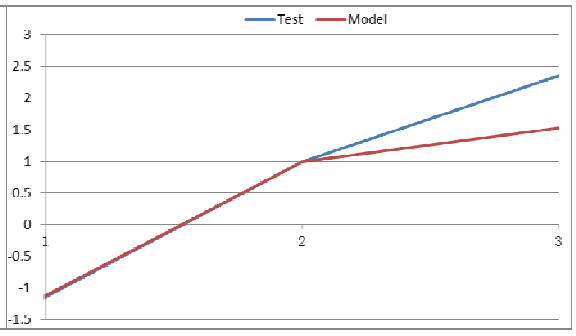

Fig. 6.6d Pressure at 164 Hz

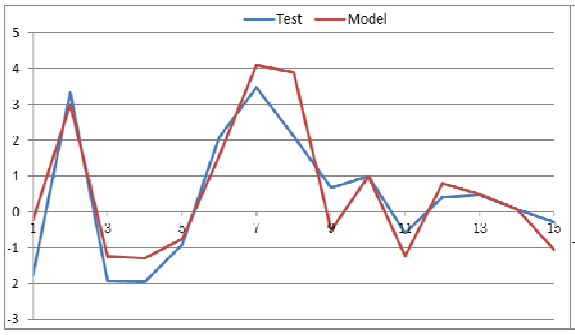

Fig. 6.6e Lateral Force at 296 Hz

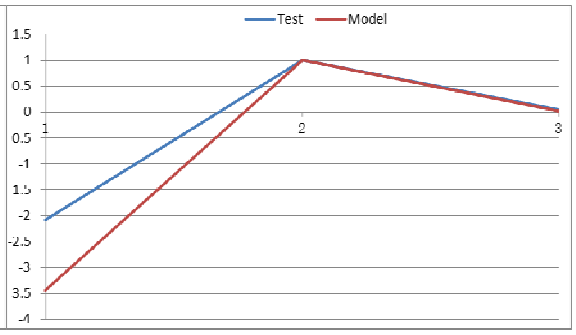

Fig. 6.6f Pressure at 296 Hz

Figure 6.6 Modal Shapes of System 1 Natural Frequency

From Figure 6.6, it can be concluded that the modal shapes of the simulation model and experimental results are essentially matched. The deviations of pressure modes could result from the simplification of the actual fluid. For example, comparing two modal shapes of the lateral force at 296 Hz, the obvious difference may be due to both imprecise measuring and calculation limitation.

The measured modal shape involves the mobile accelerometer that is moved by human. The acquired data depend on the position and direction of the accelerometer, thus the human factor affects the measured results. On the other hand, the assumption of simulation models could influence the calculation results.

Figure 6.7 illustrates the modal shapes of the key system natural frequencies for System 2. Again for the pressure, there is not enough information acquired to derive the modal shapes of the whole pipeline because only four pressure transducers are installed in this system. Therefore, the pressure relationship of these four points is described in this Figure.

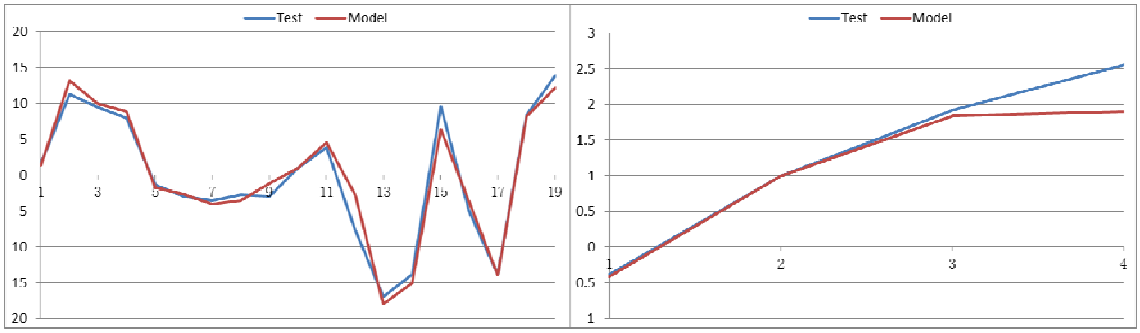

Fig. 6.7a Lateral Force at 126 Hz

Fig. 6.7b Pressure at 126 Hz

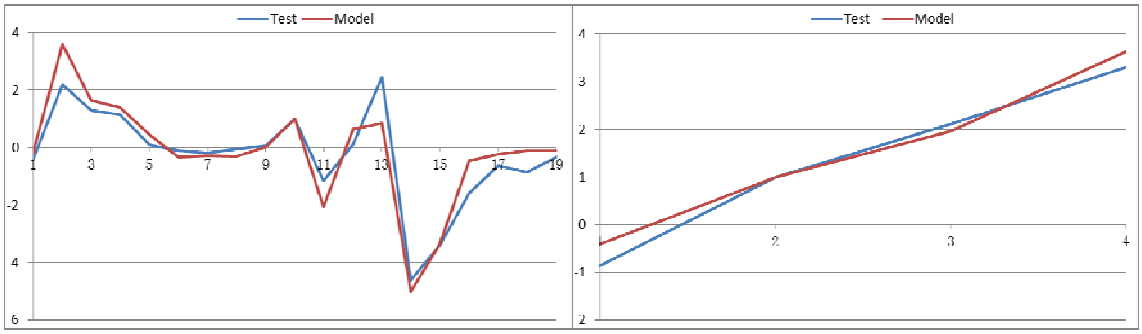

Fig. 6.7c Lateral Force at 157 Hz

Fig. 6.7d Pressure at 157 Hz

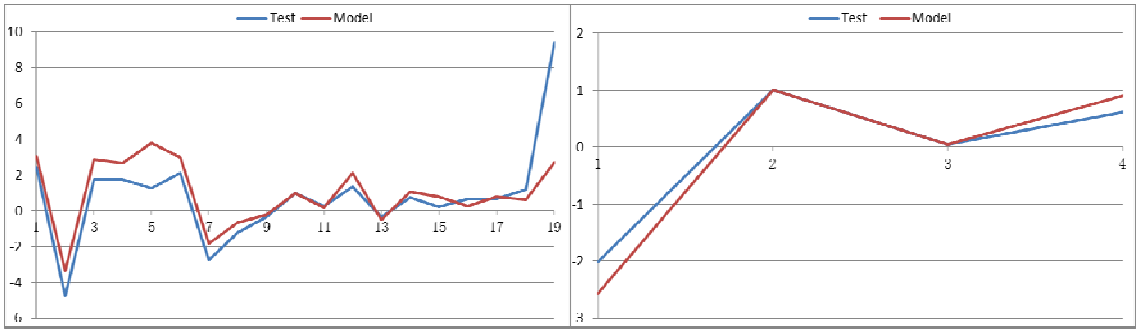

Fig. 6.7e Lateral Force at 298 Hz

Fig. 6.7f Pressure at 298 Hz

Figure 6.7 Modal Shapes of System 2 Natural Frequency

During the process of modal shape calculations, it can be found that the assumption of very small pressure inputs leads to incorrect results. It is difficult to find out the input pressure of experiments at the left end of the system; and it is not necessary to perform this. Applying assumed value, the required modal shapes can be derived from the MATLAB programme. In order to conveniently compare the simulation and test results,

the data are normalised. We divide all the pressure data by that at the point of pressure transducer 2 (see Figure 6.1) because the reference accelerometer transducer is located at this position.

6.3 Validation

According to the comparison presented in last section, it can be concluded that the simulation model effectively describes the experimental systems. Furthermore, the similar systems that are composed of pipe-hose elements connected with structural and fluidic discontinuities may be usefully represented by this model.

6.3.1 Reason of deviation

The deviation between the simulation and experimental results always results from both sides. For the experiments, the measurement is influenced by numerous factors (see section 5.5). For example, the frequency range of the circumstantial noise may cover some low structural frequencies, which are displayed at Table 6.5 and 6.6 where the natural frequencies cannot be identified.

On the other hand, the simulation model usually simplifies the actual situations. The cylinder end is considered as the fixed and close end, but actually it is more complex. As shown in Figure 5.2 and 5.3, although the circuits connected to the top and bottom chambers are separated by valves, an accumulator that is installed in the lower circuit allows for possible fluid movement in the systems when the experiments are performed. Besides, the cylinder is not really a rigid body, thus the simplified boundary may affect the simulation results. The liquid of the experiments is assumed as an inviscid and incompressible flow, which also could affect the simulation results.

6.3.2 Modification of simulation model

The preliminary mathematical models employ the equations of steel pipe to represent the hose by changing the material properties. Only the axial direction is considered in this model and the calculation results show a very large deviation to the test results even

when combined with the lateral matrix. This indicates that the hose model cannot properly represent the actual situation, thus the new hose model is derived.

Before the simulation model is revised to obtain its last version, the deviation between the calculation and test results of System 1 is smaller than that of System 2. The increased pipe elbow and pressure transducer show their effects on the system dynamics. Figure 6.8 shows the structure of the pressure transducer and the whole length of the transducer is 71mm. Since the centre of its mass is at the middle position, when it is simplified as a mass point, the length of the last pipe section should be reduced to fit this situation. Modifying the angle of the pipe elbow and the method of dividing the bend sections also improves the accuracy of the simulation model.

Figure 6.8 Last Pressure Transducer of System 2

6.4 Concluding Remarks

The assumption, mathematical simulation and experimental tests of pipelines are presented and investigated in this chapter. The pipeline is regarded as a chain system and the boundary conditions are decided. The system parameters are determined and the calculation results can be obtained by applying the models.

The simulation results and experimental results are compared, which indicates that the derived mathematical models can reasonably represent the relevant systems. Possible

reasons for result deviations are described and discussed. The preliminary mathematical model is revised several times to derive the final version of the model.

The simulation model is validated and it can be concluded that the proper model for the hydraulic pipeline is able to deliver reliable analyses of the system for improving the design of the system. The model can also be employed to create higher-level system simulations.

Chapter 7

CHARACTERISTICS ANALYSIS AND DISCUSSION

In this chapter, the hydraulic elements and structural parameters are analysed and their impact on the system dynamics are discussed. These factors show a significant influence on the system and the changes of the factors can help to optimise the system performance, especially for the noise reduction.

7.1 Impact of Hydraulic Components

For the pipe-guided liquid-filled piping systems, the hydraulic components (especially valves and accumulators) mainly show impact on the longitudinal direction of the pipeline. Most of the practical applications also concern the system dynamics in this direction. Therefore, the simulation of valves and accumulators and the discussion of their effects are in the axial direction. For the hoses, the effects in the lateral directions are mostly at the structural dynamics, which is similar to the situation of the pipes. In this section, the axial influence of hoses is discussed.

7.1.1 Orifice influence

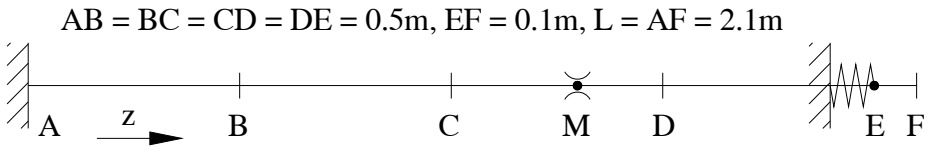

Figure 7.1 Orifice Investigation System

In this and the next sections, the discussion is focused on the effects of the orifice and accumulator, thus the hose is not included in the assumed systems. Figure 7.1 illustrates a liquid-filled piping system, which includes pipe sections, a support, and an orifice. The axial direction of this system is analysed and the orifice location is changed to show its influence. Figure 7.2 shows the first and second vibration modal shapes of fluid dis-

placement for the system without the orifice, which represents the fluid velocity distribution along the pipe. The pipe is divided into 20 sections during the simulation process. The *x* axis lists the series numbers of the sections. The *y* axis illustrates the magnitude of the velocity.

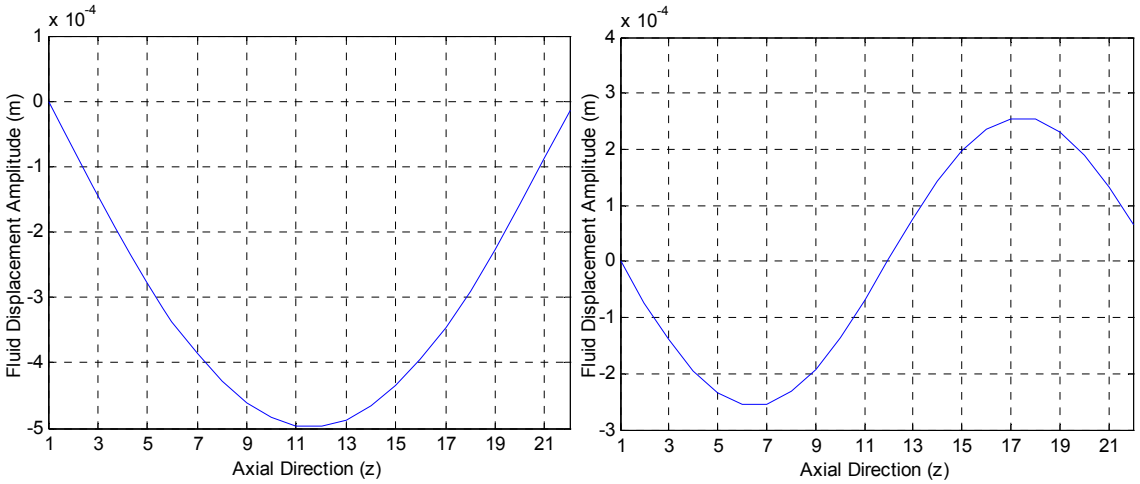

Figure 7.2 1st and 2nd Vibration Modal Shapes of Fluid Displacement

The orifice shows its impact on the system dynamics only when the radius of the cross hole is small enough. These effects displayed in Table 7.1 demonstrate that the orifice has no impact if it is equipped at Location A. For the first system natural frequency, it has little effect when it is very near Location E. When the orifice is fixed between Location C and D, the first natural frequency is much larger than that of other locations, but it is close to the second natural frequency of other locations. The two values are almost same if the orifice is located at M and the distance of ME is equal to 0.79m. It can be concluded that the orifice has a significant influence on the first vibration mode but not on the second vibration mode at the same location.

Table 7.1 Influence of Orifice Location on System Natural Frequencies

Length (m)	support on E	$\mathbf{f}_1$ (Hz)	$\mathbf{f}_2$ (Hz)
AE = 2.0	no orifice	293.6	524.3
	orifice on A	293.6	524.3
	orifice on B	383.1	540.5
	orifice on C	518.0	608.8
	orifice on M	524.7	700.6
	orifice on D	428.6	529.2
	orifice very near E	305.4	542.9

These phenomena can be explained by analysing the first two modal shapes shown in Figure 7.2. For example, the orifice has no influence at Location A, which is the closed end and the fluid velocity at this point is always equal to zero. Since the function of the orifice is to limit fluid velocity in piping systems, the orifice cannot have its influence if it is located at the nodal point at which the fluid velocity is always equal to or very close to zero. For the same reason, the orifice has no impact on the second system natural frequency at Location M.

7.1.2 Accumulator influence

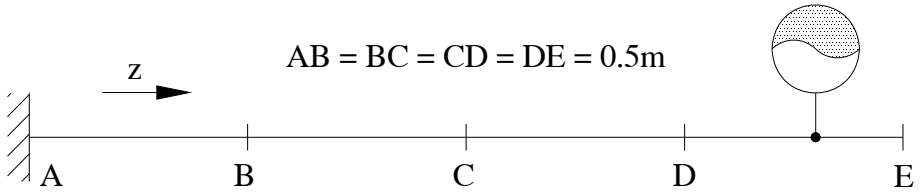

Figure 7.3 Accumulator Investigation System

The system shown in Figure 7.3 is to analyse the accumulator influence on the system. To reduce the effects from other factors, only an accumulator and pipe sections are included. The axial direction of this system is analysed and the accumulator position is changed to obtain the results of different situations. Figure 7.4 shows the first and second vibration modal shapes of fluid pressure for the system without the accumulator, which represents the pressure distribution along the pipe. The *x* axis is the series number of pipe sections and the *y* axis is the inside pressure.

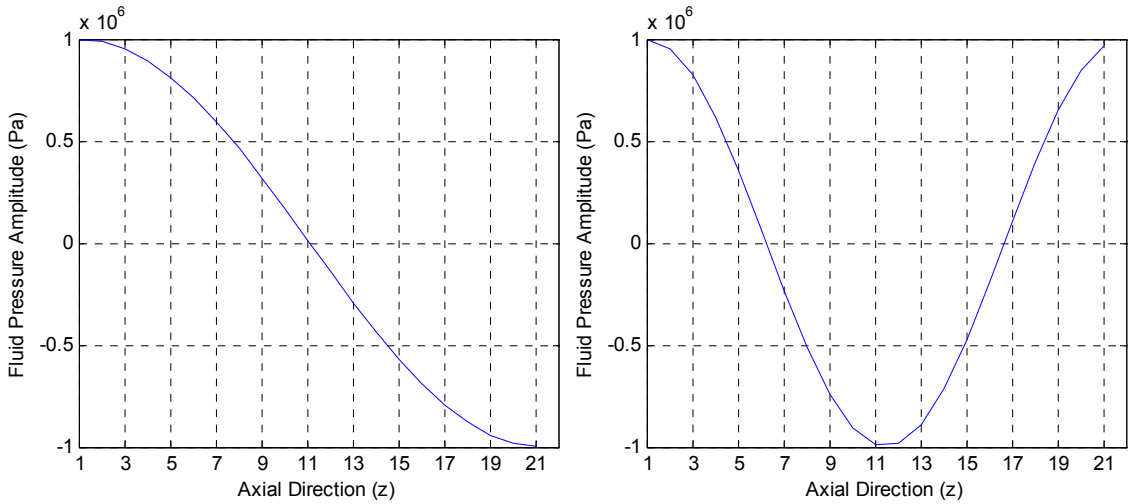

Figure 7.4 1st and 2nd Vibration Modal Shapes of Fluid Pressure

Table 7.2 shows the influence of the accumulator's location on the system natural frequencies. The accumulator has no impact on the first natural frequency when it is placed on the middle of the piping (Location C) because the pressure amplitude almost equals zero at this nodal point. The function of the accumulator is to reduce the water hammer influence, i.e. the fluid pressure peak value in piping systems. Therefore, the accumulator cannot have its influence if it is located at the point that the pressure is always equal to zero. The same phenomenon is shown on the second system natural frequency when the accumulator is equipped on Location B or D.

Table 7.2 Influence of Accumulator Location on System Natural Frequencies

Length (m)	Accumulator position	$\mathbf{f}_1$ (Hz)	$\mathbf{f}_2$ (Hz)
AE = 2.0	no accumulator	309.1	598.7
	accumulator on C	309.1	643.1
	accumulator on B	219.6	598.6
	accumulator on D	220.7	600.0

According to conservation of energy, the total amount of the potential energy and the kinetic energy of the system is constant at any point. Large pressure implies large potential energy and large velocity means large kinetic energy. At one location on which the potential energy is dominant, the kinetic energy must be small, and vice versa. This conclusion can be proved by comparing Figure 7.2 and 7.4.

7.1.3 Hose influence

By comparing the preliminary model [132] and the further model in this study, the hose shows significant effects on system dynamics. Taking the System 1 as an example, Figure 7.5, 7.6, and 7.7 show that the influence of hose length, hose elastic moduli, and hose density on the axial system natural frequencies respectively. The figures display that these characteristics of the hose show obvious effects at the middle to high frequency range.

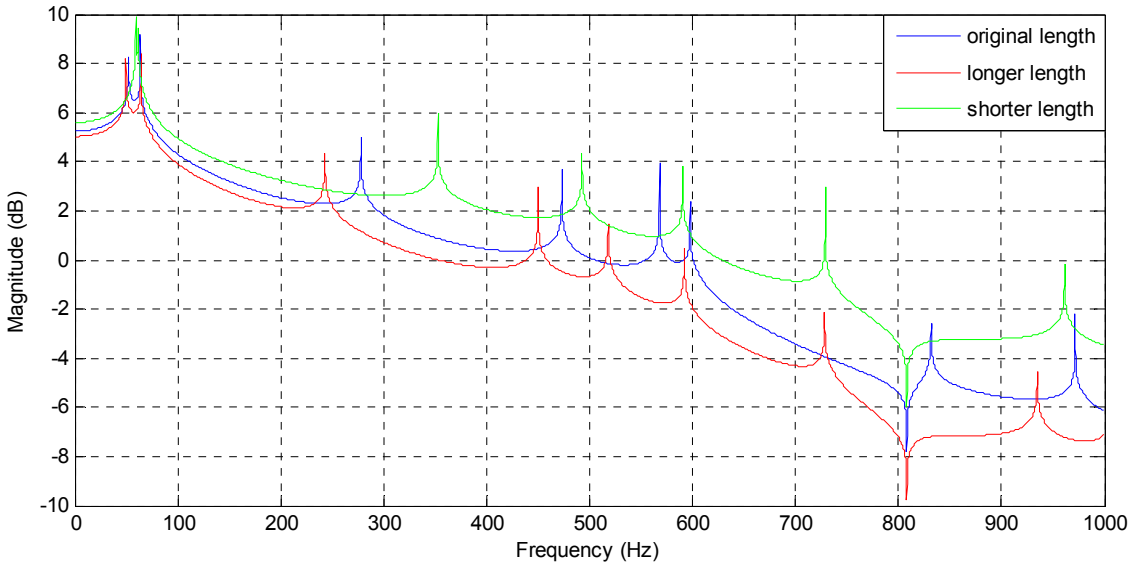

Figure 7.5 Effect of Hose Length

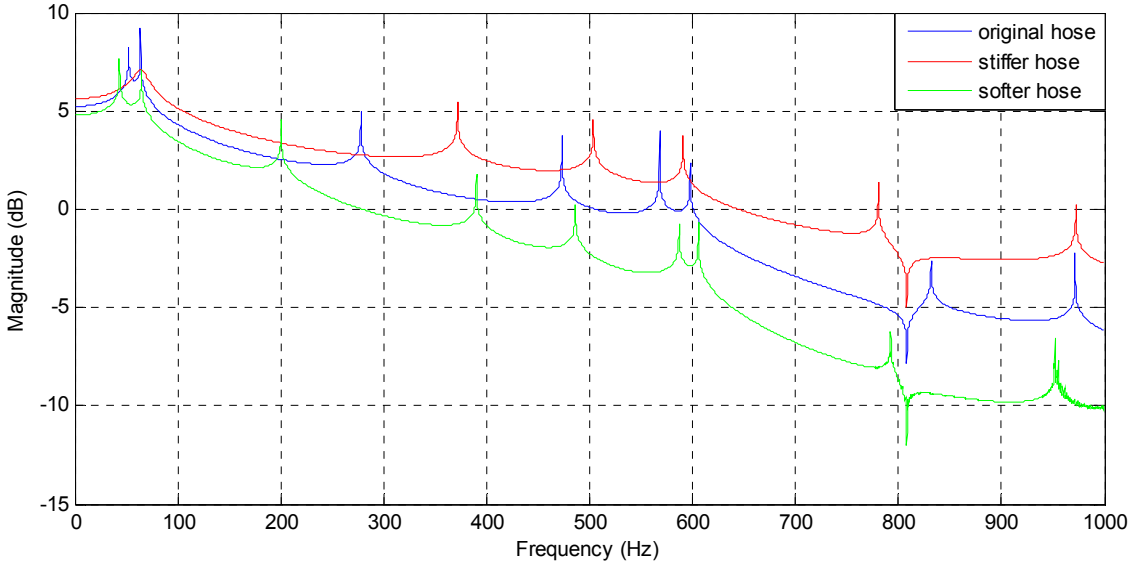

Figure 7.6 Effect of Hose Elastic Moduli

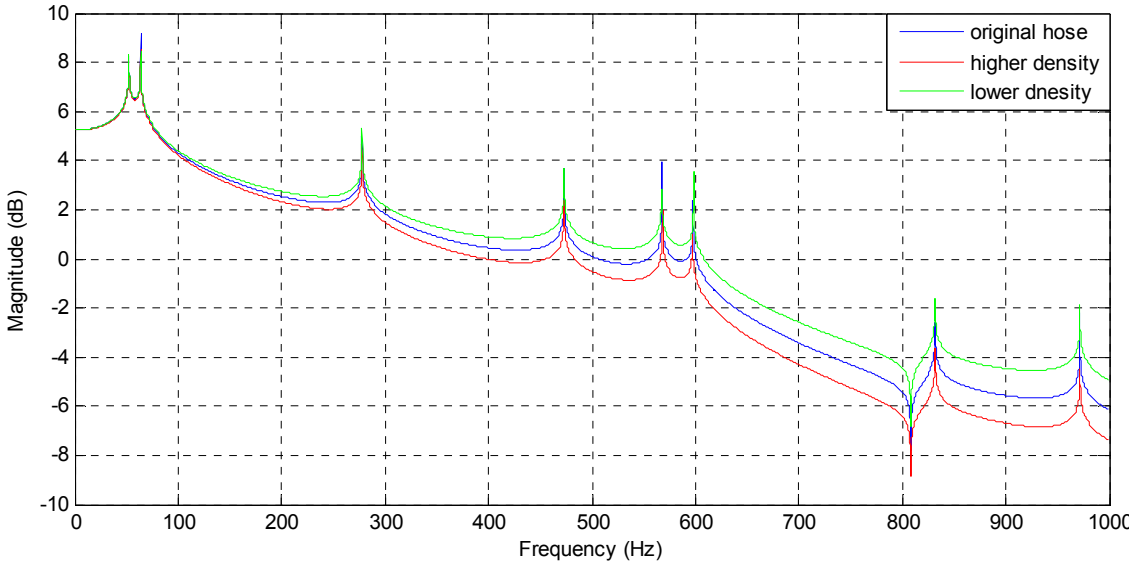

Figure 7.7 Effect of Hose Density

According to Figure 7.5, the longer the hose, the lower the system natural frequencies are. Since the longer hose decreases the system stiffness, the natural frequencies of the "*softer*" system are lower than the original ones. Figure 7.6 shows that the increasing stiffness of hoses could raise the system natural frequencies because it increase the system stiffness. From Figure 7.7, it can be concluded that the hose density has almost no impact on the axial system natural frequencies.

From the three figures, it can be concluded that the length and elastic moduli of the hose have more impact than the density of the hose on system natural frequencies. For the straight pipeline, the axial frequencies are influenced by the hose wall with the Poisson coupling, which is mainly determined by the elasticity of the hose wall (the moduli of the hose wall). Hoses can be considered as *soft* pipes, thus the length of the hose in a system affects the elastic moduli of the whole pipeline. Therefore, the hose length also shows obvious effects at the system.

The hose density would have more effects at systems with curved pipes and hoses, in which the junction coupling is dominated. The stiffness of a system is the key characteristics under this circumstance. The density of hoses influences the system stiffness and, consequently, affects the system dynamics.

7.2 Impact of Structural Components

In this section, structural elements are analysed and investigated to show their impact on the natural frequencies of System 1. Unlike System 1 that has no bend, System 2 is applied for the investigation of the pipe bend. The change of pipe properties modifies the stiffness of the system, which influence the natural frequencies. For the piping system with the pipe elbow, the angle of the bend and the radius of the curve have a low impact on the system dynamics.

7.2.1 Pipe influence

The diameter of the pipeline has an impact on the system natural frequencies, shown in Figure 7.8 and Table 7.3. The results illustrate that the bigger diameter of the pipeline offers a higher stiffness for the system, thus the natural frequencies shift towards higher value.

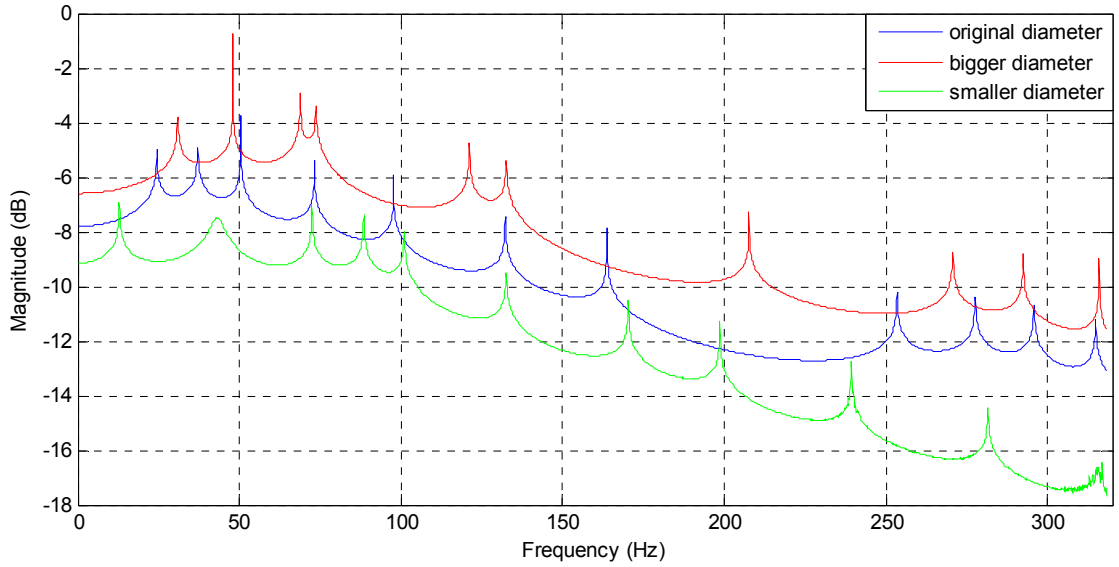

Figure 7.8 Effect of Pipeline Diameter

Table 7.3 Effect of Pipeline Diameter

Frequency (Hz)	f_1	f_2	f_3	f_4	f_5	f_6	f_7	f_8	f_9	f_{10}
D = 0.03 m	30.9	47.9	68.7	73.8	121.1	132.4	207.7	270.7	292.4	315.9
Original model D = 0.0166 m	24.5	37.2	50.5	73.2	97.7	132.3	163.8	253.5	277.7	295.7
D = 0.01 m	12.9		43.1	72.4	88.5	100.9	132.4	170.3	198.6	239.2 281.5

Table 7.4 and Figure 7.9 display the effects of pipe thickness on system natural frequencies. According to the simulation results, the thicker the pipe thickness, the higher the system natural frequencies are. The increased thickness of the pipe wall provides extra stiffness to the system, consequently increasing the natural frequencies.

Table 7.4 Effect of Pipe Thickness

Frequency (Hz)	f_1	f_2	f_3	f_4	f_5	f_6	f_7	f_8	f_9	f_{10}
e = 0.002 m	32.0	37.1	50.5	73.5	103.9	132.3	185.9	261.0	278.0	
Original model e = 0.0012 m	24.5	37.2	50.5	73.2	97.7	132.3	163.8	253.5	277.7	295.7
e = 0.0005 m	15.4	36.6	50.5	72.7	90.7	117.6	132.1	190.5	276.9	

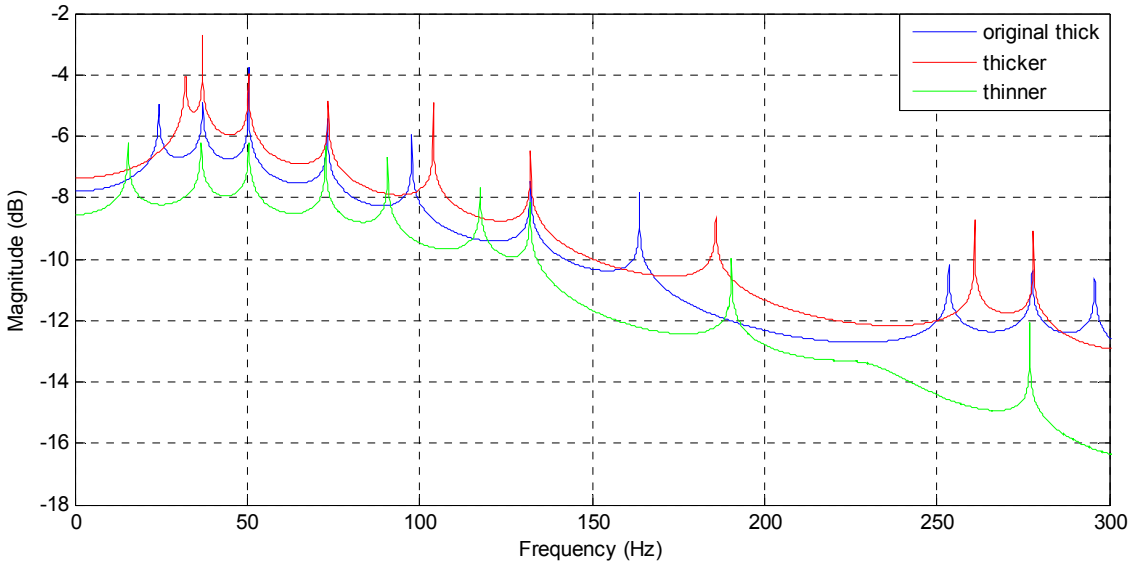

Figure 7.9 Effect of Pipe Thickness

Table 7.5 and Figure 7.10 show that the system natural frequencies move to higher range with the increased pipe elastic moduli, which increases system stiffness. The significant impact is on three frequencies ($\mathbf{f_7}$, $\mathbf{f_8}$, $\mathbf{f_{10}}$) as these frequencies are influenced by both the fluid and structures. The elastic moduli show significant effects on the Poisson coupling that in turn affects the fluid dynamics in the axial direction.

Table 7.5 Effect of Pipe Elastic Modulus

Frequency (Hz)	$\mathbf{f_1}$	$\mathbf{f_2}$	$\mathbf{f_3}$	$\mathbf{f_4}$	$\mathbf{f_5}$	$\mathbf{f_6}$	$\mathbf{f_7}$	$\mathbf{f_8}$	$\mathbf{f_9}$	$\mathbf{f_{10}}$
E = 250 GPa	26.6	37.2	50.5	73.4	100.1	132.3	173.6	264.2	277.9	310.2
Original model E = 207 GPa	24.5	37.2	50.5	73.2	97.7	132.3	163.8	253.5	277.7	295.7
E = 160 GPa	21.6	36.9	50.5	73.1	94.7	132.1	148.7	233.8	272.5	293.2

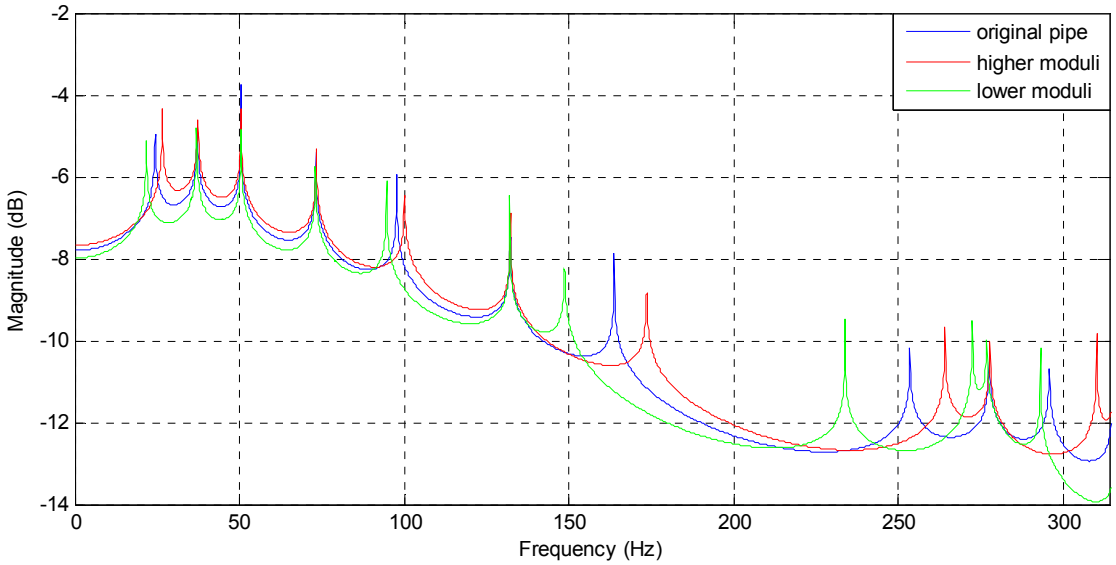

Figure 7.10 Effect of Pipe Elastic Modulus

From Table 7.6 and Figure 7.11, it can be concluded that the impact of pipe density on system natural frequencies is increased with the frequency value. At the high frequency range, the density shows more significant effects, which means the pipe density is sensitive to the high frequencies. Since the noise is always at a high frequency range, this could be used to modify the system parameters to reduce the noise.

Table 7.6 Effect of Pipe Density

Frequency (Hz)	f_1	f_2	f_3	f_4	f_5	f_6	f_7	f_8	f_9	f_{10}
$\rho_p = 9000$ kg/m^3	24.4	37.1	50.5	73.2	97.1	132.3	161.5	247.2	277.7	292.2
Original model $\rho_p = 7850$ kg/m^3	24.5	37.2	50.5	73.2	97.7	132.3	163.8	253.5	277.7	295.7
$\rho_p = 6700$ kg/m^3	24.5	37.2	50.5	73.2	98.4	132.3	166.0	260.2	277.7	299.4

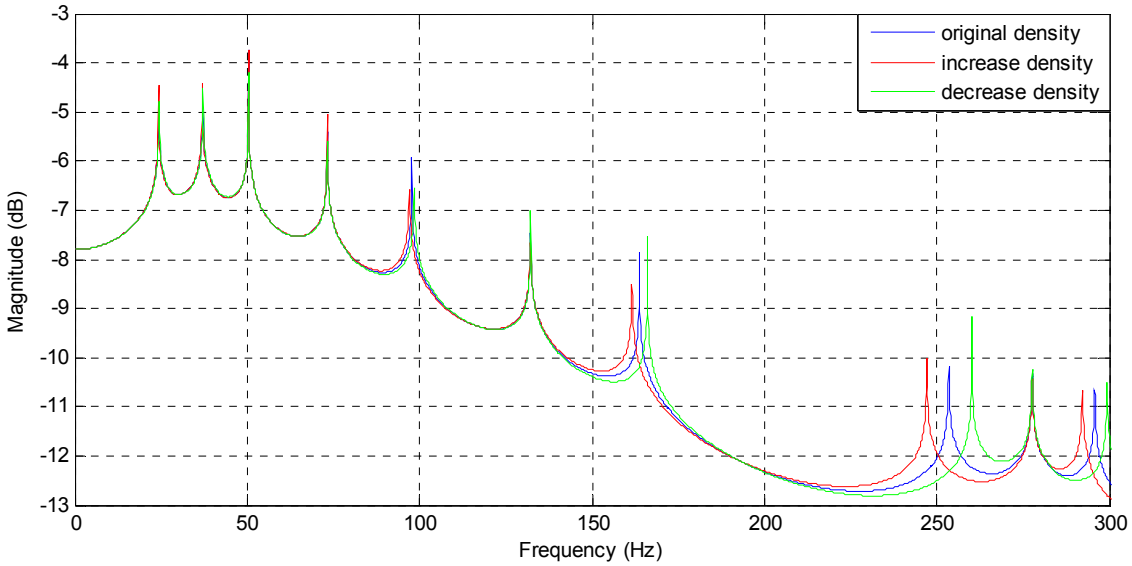

Figure 7.11 Effect of Pipe Density

7.2.2 Pipe elbow influence

The angle of two adjacent pipe sections and the radius of the curvature influence piping systems with curved pipes. Figure 7.12 and 7.13 illustrate these effects. According to Figure 7.12, the radius of the pipe curve shows little effect on most system natural frequencies except in one frequency. The increased radius shifts this frequency towards a higher value. The effect of the elbow angle on system frequencies is not very significant either. The frequencies are increased with the larger angle.

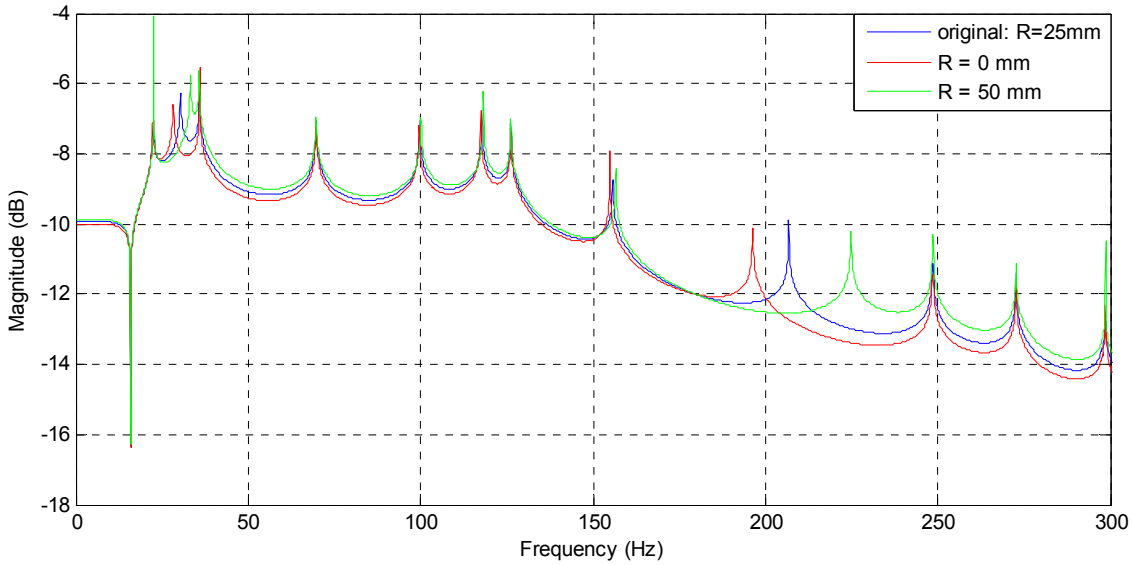

Figure 7.12 Effect of Curvature Radius

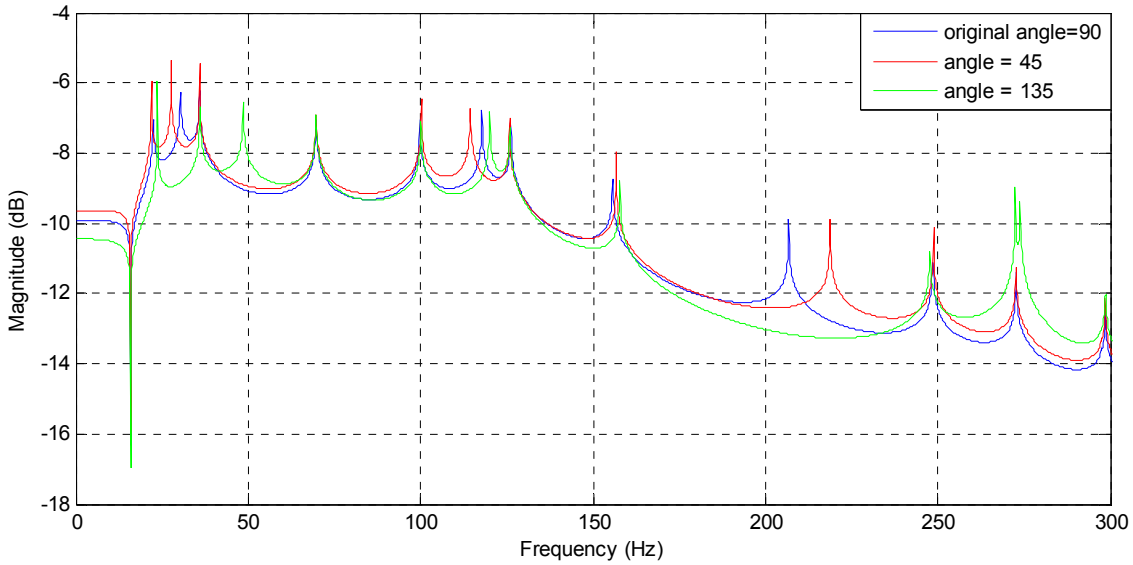

Figure 7.13 Effect of Elbow Angle

From these two figures, it can be concluded that the pipe elbow decreases the system stiffness. Increasing either the curvature radius or the elbow angle reduces this influence. Therefore, any effort that tries to reduce this influence could increase the system stiffness. However, the figures show that these two parameters are not sensitive to the system natural frequencies.

The changes of these two factors affect the length of curved pipes and adjacent pipes, which are removed at this section in order to clearly show their influence. For the pipeline with elbows, the effects of fluidic and structural components are not only in one di-

rection of the vibrations. The longitudinal and radial vibrations are coupled at the pipe bends and the influence is relatively complex.

7.3 Noise Reduction Methods

Vehicle performance requirements are mainly decided by the characteristics of valves, accumulators, hoses, and pipes. Compared with handling efficiency and safety reliability, the noise problems should be a secondary consideration. However, the equipment positions of valves and accumulators and the length of pipes and hoses could be adjusted to avoid some noise when the assembly convenience is taken into account as well. According to the sensitivity analysis described in the above section, the radius of pipe curvature and the angle of the bend are not good choices when the system natural frequencies need for any reason to be changed. The decision of these parameters must comply with the assembly requirement.

The number, position, and stiffness of the support mainly influence the lateral frequencies and modal shapes. According to the modal shape of certain frequencies, the vibration could be reduced by equipping a support at the position with maximum amplitude. The detailed analyses are not displayed here because numerous researchers have studied this type of investigation. In order to reduce the fluid induced vibrations in the HIS system and the consequent noise of the vehicle, the supports that are equipped to fix the pipeline should be considered. Resonant frequencies can be avoided and some vibrations amplitude can be decreased by adjusting the numbers and locations of the supports. Normally the stiffness of a support is almost decided when it is installed on the system. However, the different type of supports can be applied to modify the stiffness.

7.4 Concluding Remarks

The effects of fluidic and structural parameters on system natural frequencies are investigated in this chapter. The hydraulic components mainly influence the axial direction of piping systems. The structural parts display their impact on both the axial and lateral directions. The fluid induced vibrations in pipe-guided liquid-filled hydraulic systems are affected by numerous factors.

Noise results from these vibrations in the HIS system need to be decreased to improve the vehicle performance. In order to reduce the noise, the parameters can be adjusted to change the system dynamics even if some of them are decided by the handling and safety performance requirements of the vehicle due to their higher priority. The understanding of the pipe-guided liquid-filled piping system can provide a theoretical basis when the system needs to be modified with particular requirements.

Chapter 8

CONCLUSION

8.1 Contribution and Potential Impact

This dissertation presented an extended transfer matrix method for free vibration analysis of pipe-guided liquid-filled hydraulic piping systems and the experimental validation of the mathematical model. The derived element models of hydraulic components improve the understanding of fluid-structure interactions in these types of systems. The system model includes field matrices for pipe sections and hose sections, point matrices for fluidic discontinuities such as valves and accumulators, and structural discontinuities like concentrated masses, supports, and elbows. Various combinations of the element models represent different systems.

The newly developed models of hydraulic components and improved models of structural parts extend the understanding of transfer matrix method. The investigation methods of pure piping systems can be applied on the chain systems that consist of lines and discontinuous joints. The impedance characteristics are employed in the developed matrices, which provide the possible combination between the TMM and the impedance method.

The system experiments of two configurations are performed on a UTS designed test rig. The experiments have been performed several times and the models have been revised according to the measuring and calculated results. The comparison between experimental and simulation results displayed in this thesis shows that the deviation is relatively small, thus the theoretical model can properly describe both piping systems. The environmental factors and the processes of tests affect the experimental measurements. The tests can be improved by eliminating the noise and human factors and applying advanced apparatuses and equipment.

The system dynamic characteristics have been investigated at various system configurations. The obtained results show that the influence of the orifice and accumulator can be explained by their physical implications. For a certain vibration mode, the accumulator shows an obvious impact on the pressure ripple when it is equipped at the position where the pressure change is large; and the orifice can effectively control the fluid speed if it is fitted at the location of large fluid velocity.

The sensitivity analysis of hose and pipe properties shows that the system steady state characteristics can be modified by changing these parameters. Both the material and dimension of hoses shows a significant impact on system dynamics. The axial vibrations of different pipe sections are coupled by pipe elbows to produce complicated system dynamics at the two dimensional plane. However, the angle of the bend and the radius of the curvature have a small impact on the system.

In order to reduce the fluid-induced noises at HIS and connecting structures, the dynamic characteristics of the piping system could be adjusted by considering the properties and positions of hydraulic and structural components. However, the characteristics of valves, accumulators, hoses, and pipes are mainly related to vehicle performance requirements. The change of the configuration of the components and their positions could modify the system dynamics and has to satisfy the easy assembly requirement.

The mathematical model developed in this thesis is a fluid-structure interaction representation of piping systems in terms of conventional hydraulic components (valves, accumulators, and hoses). According to the investigations and analyses of element models and system models, the key system parameters are identified and possible methods for decreasing fluid-induced vibrations have been found. The development and discussion of the models provide a theoretical basis for future optimisation and improvement.

The analysis method in this thesis can be widely used in many engineering applications, especially in aerospace, aviation, the petroleum industry, and the nuclear industry. The fluid induced vibrations in the piping system cause serious problems in these industries, thus considerable studies focus on investigations of the nature of the vibration. This study provides an extended understanding of this area and the method of this study can be employed in particular applications.

8.2 Future Work and Recommendation

8.2.1 Curved hose

The mathematical model can be applied on various combinations of system configurations. Table 8.1 lists the simulation and experimental system natural frequencies of a piping system that includes pipe elbows and a hose bend. The signals of measured frequencies come from pressure transducers, thus some structural results are not included here. An obvious deviation is shown between the test and calculation results, which could result from the added hose bend. In this thesis, the straight-hose model is employed to represent hose sections. For the two pipelines studied above, the included hoses are almost straight, thus the straight-hose model is suitable for the straight hose.

Table 8.1 Frequency Comparison

Frequency (Hz)	f_1	f_2	f_3	f_4	f_5	f_6
Simulation results	88	264	276	496	512	624
Test results	66	222.8	276.9	467	518.5	616.4

The simulation model used for Table 8.1 regards the hose bend as several straight hoses connected with elbow joints. The comparison results imply that this assumption is not precise to demonstrate the actual situation. This is related with the modelling of the FSI phenomenon in the hose. The FSI includes three coupling mechanisms: Poisson coupling, junction coupling, and friction coupling which is ignored in most practical systems. The Poisson coupling is distributed along the axis of a pipe element, whereas junction coupling acts at discrete locations such as the elbows, branches, T-junctions etc. [34, 36]. It can be concluded that for FSI phenomena in the hose, the Poisson coupling can be similarly modelled to the pipe situation, but the junction coupling shows more complex dynamics than it does in the pipe.

Future studies could extend the existing model in order to achieve a more accurate representation of the curved hose situation. The developed system model of the piping system can be employed to analyse the system steady state dynamics, however for transient dynamics, further works are needed.

8.2.2 Coupling with connected structure

As the investigation of the fluid-structure interaction in piping systems can be widely used in many fields e.g. aerospace, aviation, the petroleum industry, and nuclear industry, further studies could analyse the coupling between the piping systems and the connected structures. These types of studies could be more specific for the particular application.

As the simulation models developed in this research are transfer matrices and the connected structures are represented by different models, the methodology of how to combine various mathematical models could be the focus of further research. In addition, further analyses, investigation, discussion, and applications of the extended models are also important.

APPENDIX A

Curved Pipe Section versus Straight Pipe Section

As mentioned in Chapter 3 (Section 3.3.1), the principle of the straight-pipe model [45-48] and developed curved-pipe model [49, 50] are the same. Besides, the curved-pipe model is no better than the other one; and it presents more difficulty when combined with other element models due to the consideration of the elbow. An eight-equation model is used as an example to explain this comparison in detail.

According to Valentin et al. [50], an eight-equation model of the pipe elbow is shown as:

$$\begin{cases} \dfrac{\partial p}{\partial s}+\rho_f \dfrac{\partial \dot{v}}{\partial t}=0 \\ \left(\dfrac{1}{K}+2\dfrac{r}{e_p}\dfrac{1-\nu^2}{E}\right)\dfrac{\partial p}{\partial t}+2\dfrac{R^2}{r^2}\left[1-\left(1-\dfrac{r^2}{R^2}\right)^{\frac{1}{2}}\right]\dfrac{\partial \dot{v}}{\partial s}-2\nu\dfrac{\partial \dot{u}_s}{\partial s}+(1-2\nu)\dfrac{\dot{u}_t}{R}=0 \\ \dfrac{\partial f_s}{\partial s}+\dfrac{1}{R}f_t-\rho_p A_p\dfrac{\partial \dot{u}_s}{\partial t}=0 \\ \dfrac{1}{EA_p}f_s-\dfrac{u_t}{R}-\dfrac{\partial u_s}{\partial s}-\dfrac{r\nu}{e_p E}P=0 \end{cases} \quad \text{(Equation 9.1)}$$

$$\begin{cases} \dfrac{\partial f_t}{\partial s}+\dfrac{1}{R}f_s+\dfrac{A_f}{R}p-(\rho_f A_f+\rho_p A_p)\dfrac{\partial \dot{u}_t}{\partial t}=0 \\ \dfrac{1}{\kappa G_p A_p}f_t-\dfrac{\partial u_t}{\partial s}+\theta+\dfrac{u_s}{R}=0 \\ \dfrac{\partial m}{\partial s}+f_t-\rho_p I_p\dfrac{\partial \dot{\theta}}{\partial t}=0 \\ \dfrac{1}{EI_p}m-\dfrac{\partial \theta}{\partial s}=0 \end{cases} \quad \text{(Equation 9.2)}$$

In these equations, the subscript *s* represents the longitudinal direction of the curved pipe, i.e. the coordinate line is along the centreline of the pipe; and *t* represents the latitudinal direction, which is the transverse axis of the centreline. The letter *R* is the radius of the curvature of the pipe centreline, being equal to infinity on the condition that a

straight pipe is described by this model. In this case, the term $\frac{1}{R}$ equals to zero, thus the two equations turn to:

$$\begin{cases} \dfrac{\partial p}{\partial s}+\rho_f \dfrac{\partial \dot{v}}{\partial t}=0 \\ \left(\dfrac{1}{K}+2\dfrac{r}{e_p}\dfrac{1-\nu^2}{E}\right)\dfrac{\partial p}{\partial t}+2\dfrac{R^2}{r^2}\left[1-\left(1-\dfrac{r^2}{R^2}\right)^{\frac{1}{2}}\right]\dfrac{\partial \dot{v}}{\partial s}-2\nu\dfrac{\partial \dot{u}_s}{\partial s}=0 \\ \dfrac{\partial f_s}{\partial s}-\rho_p A_p \dfrac{\partial \dot{u}_s}{\partial t}=0 \\ \dfrac{1}{EA_p}f_s-\dfrac{\partial u_s}{\partial s}-\dfrac{r\nu}{e_p E}P=0 \end{cases} \quad \text{(Equation 9.3)}$$

$$\begin{cases} \dfrac{\partial f_t}{\partial s_s}-(\rho_f A_f+\rho_p A_p)\dfrac{\partial \dot{u}_t}{\partial t}=0 \\ \dfrac{1}{\kappa G_p A_p}f_t-\dfrac{\partial u_t}{\partial s}+\theta=0 \\ \dfrac{\partial m}{\partial s}+f_t-\rho_p I_p \dfrac{\partial \dot{\theta}}{\partial t}=0 \\ \dfrac{1}{EI_p}m-\dfrac{\partial \theta}{\partial s}=0 \end{cases} \quad \text{(Equation 9.4)}$$

According to the principle of limit, the term $2\dfrac{R^2}{r^2}\left[1-\left(1-\dfrac{r^2}{R^2}\right)^{\frac{1}{2}}\right]$ equals to 1, with moving some coefficients, the equation 9.3 and 9.4 can be displayed as follows:

$$\begin{cases} \dfrac{\partial p}{\partial s}+\rho_f \dfrac{\partial \dot{v}}{\partial t}=0 \\ \left[\dfrac{1}{K}+(1-\nu^2)\dfrac{2r}{Ee_p}\right]\dfrac{\partial p}{\partial t}+\dfrac{\partial \dot{v}}{\partial s}-2\nu\dfrac{\partial \dot{u}_s}{\partial s}=0 \\ \dfrac{\partial f_s}{\partial s}-\rho_p A_p \dfrac{\partial \dot{u}_s}{\partial t}=0 \\ f_s-EA_p\dfrac{\partial u_s}{\partial s}-\dfrac{r\nu A_p}{e_p}P=0 \end{cases} \quad \text{(Equation 9.5)}$$

$$\begin{cases} \dfrac{\partial f_t}{\partial s} - (\rho_f A_f + \rho_p A_p)\dfrac{\partial \dot{u}_t}{\partial t} = 0 \\ f_t - \kappa G_p A_p\left(\dfrac{\partial u_t}{\partial s} + \theta\right) = 0 \\ \dfrac{\partial m}{\partial s} - \rho_p I_p \dfrac{\partial \dot{\theta}}{\partial t} + f_t = 0 \\ m - EI_p \dfrac{\partial \theta}{\partial s} = 0 \end{cases} \quad \text{(Equation 9.6)}$$

In these equations, the s is the z coordinate (axial direction) and the t represent x axis (lateral direction).

Since the studies of Zhang et al. [45-48] focus on the analyses of the straight pipe in the longitudinal direction not in the other directions, the eight-equation model of straight pipe section presented by Wiggert et al. [133] is applied as a reference.

$$\begin{cases} \dfrac{\partial p}{\partial z} + \rho_f \dfrac{\partial \dot{v}}{\partial t} = 0 \\ \left[\dfrac{1}{K} + (1-\nu^2)\dfrac{2r}{Ee_p}\right]\dfrac{\partial p}{\partial t} + \dfrac{\partial \dot{v}}{\partial z} - 2\nu\dfrac{\partial \dot{u}_z}{\partial z} = 0 \\ \dfrac{\partial f_z}{\partial z} - \rho_p A_p \dfrac{\partial \dot{u}_z}{\partial t} = 0 \\ \dfrac{\partial f_z}{\partial t} - EA_p \dfrac{\partial \dot{u}_z}{\partial z} - \dfrac{r\nu A_p}{e_p}\dfrac{\partial p}{\partial t} = 0 \end{cases} \quad \text{(Equation 9.7)}$$

$$\begin{cases} \dfrac{\partial f_x}{\partial z} - \left(\rho_p A_p + \rho_f A_f\right)\dfrac{\partial \dot{u}_x}{\partial t} = 0 \\ \dfrac{\partial f_x}{\partial t} - \kappa G_p A_p\left(\dfrac{\partial \dot{u}_x}{\partial z} - \dot{\theta}_y\right) = 0 \\ \dfrac{\partial m_y}{\partial z} - \left(\rho_p I_p + \rho_f I_f\right)\dfrac{\partial \dot{\theta}_y}{\partial t} + f_x = 0 \\ \dfrac{\partial m_y}{\partial t} - EI_p \dfrac{\partial \dot{\theta}_y}{\partial z} = 0 \end{cases} \quad \text{(Equation 9.8)}$$

When eliminating the differential to time ($\dfrac{\partial}{\partial t}$), the equations are expressed as:

$$\begin{cases} \dfrac{\partial p}{\partial z}+\rho_f \dfrac{\partial \dot{v}}{\partial t}=0 \\ \left[\dfrac{1}{K}+(1-\nu^2)\dfrac{2r}{Ee_p}\right]\dfrac{\partial p}{\partial t}+\dfrac{\partial \dot{v}}{\partial z}-2\nu\dfrac{\partial \dot{u}_z}{\partial z}=0 \\ \dfrac{\partial f_z}{\partial z}-\rho_p A_p \dfrac{\partial \dot{u}_z}{\partial t}=0 \\ f_z-EA_p\dfrac{\partial u_z}{\partial z}-\dfrac{r\nu A_p}{e_p}p=0 \end{cases} \quad \text{(Equation 9.9)}$$

$$\begin{cases} \dfrac{\partial f_x}{\partial z}-\left(\rho_p A_p+\rho_f A_f\right)\dfrac{\partial \dot{u}_x}{\partial t}=0 \\ f_x-\kappa G_p A_p\left(\dfrac{\partial u_x}{\partial z}-\theta_y\right)=0 \\ \dfrac{\partial m_y}{\partial z}-\left(\rho_p I_p+\rho_f I_f\right)\dfrac{\partial \dot{\theta}_y}{\partial t}+f_x=0 \\ m_y-EI_p\dfrac{\partial \theta_y}{\partial z}=0 \end{cases} \quad \text{(Equation 9.10)}$$

When Equation 9.5 is compared with Equation 9.9, it can be concluded that the two groups of equations are identical to each other respectively. The same situation is shown in the comparison of Equation 9.6 and Equation 9.10.

APPENDIX B

Spring Support Test

In order to determine the stiffness of the supports used in this research, a test is performed. Figure 9.1 shows the configuration of the test. A displacement meter with 0.01 millimetre resolution (Figure 9.2) and several weight plates are employed in the test. Since three supports of the test rig are same, the test is performed on two supports to compare the results and show the relationship between support stiffness and installation status.

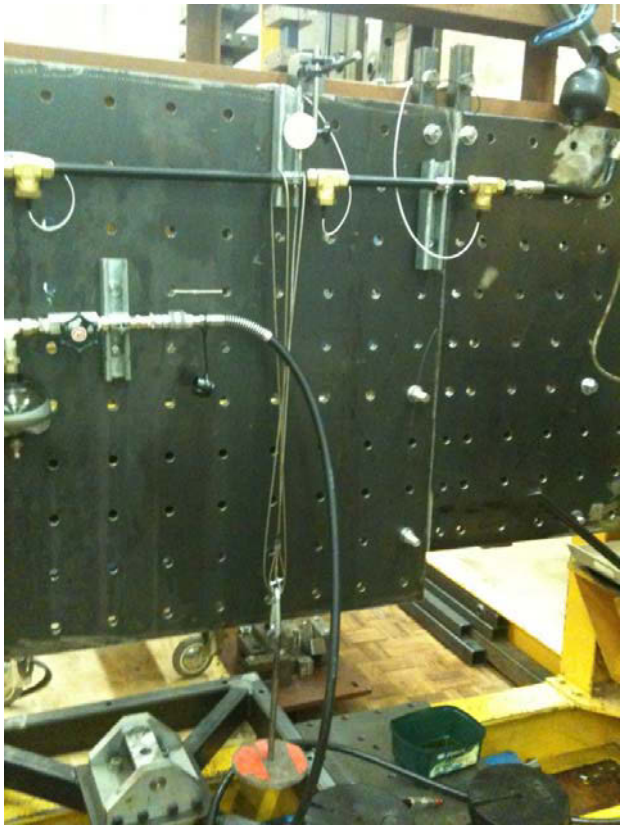

Figure 9.1 Photo of Support Test Equipment

Figure 9.2 Photo of Displacement Meter

To prepare the test, a displacement meter is fixed above the support and the probe is placed on the top of the support. Two steel wires are hung on both sides of a support and the bottom endings of the wires are connected with a weight plate tray. We then adjust the meter at ZERO position before any block-weight is put on the tray. When all the equipment is settled, three 100N weight plates are added one by one on the tray and the displacement values shown on the meter are recorded for each plate. We then take away each plate and record the displacement value until all the plates are removed.

The stiffness can be calculated by the equation $k = \frac{F}{\Delta L}$. Table 9.1 shows the stiffness of two supports, which is obtained from the test. It can be concluded that a stiffness of one support is not a constant, i.e. the relationship between force and deformation is nonlinear. In order to simplify the model of the spring support, the stiffness is assumed as a constant.

Table 9.1 Measured Stiffness

Force(N) / Stiffness(10^6N/m)	**0**	**100**	**200**	**300**
Support 2	0	1	1.5	2.1
Support 3	0	5	6.7	7.2

Table 9.1 also shows that the stiffness of two supports is not the same. This means the results are influenced by the installation status of supports. Figure 9.3 displays the status

of three supports. According to this figure and the above table, it can be concluded that the stiffness of a support is affected by the tightness of the screw when it is assembled. Therefore, the stiffness of Support 1 should be smaller than the others.

9.3a Photo of Support 1 9.3b Photo of Support 2 9.3c Photo of Support 3

Figure 9.3 Photos of Supports

PUBLICATION

Zhao, J. and Zhang, N., 2009, *Vibration of hydraulically interconnected suspensions due to fluid-structure interaction*, Proceedings of the 13th Asia-Pacific Vibration Conference, Christchurch, New Zealand, Nov 22-25, paper 28.

Zhao, J. et al., 2010, *Fluid induced vibration in liquid-filled pipe guided hydraulic circuit systems*, Proceedings of 6th Australasian Congress on Applied Mechanics, ACAM 6, Perth, Australia, Dec 12-15.

Zhao, J. et al., 2011, *Fluid induced vibration in the liquid-filled hydraulic circuit of passive interconnected suspensions*, Proceedings of the ASME 2011 International Mechanical Engineering Congress & Exposition, Denver, Colorado, USA, Nov 11-17.

REFERENCE

1. Wikipedia. Suspension (vehicle). [cited 2 March 2007]; Available from: http://en.wiki pedia.org/wiki/Suspension_%28vehicle%29.
2. Bastow, D., G. Howard, and J.P. Whitehead, Car suspension and handling. 4th edition ed. 2004, USA: SAE International, Warrendale, Pa.
3. Monroe. Suspension system fundamentals. 2005 [cited 2 March 2007]; Available from: http://www.monroe.com/tech_support/tec_suspsystemfund.asp.
4. Gillespie, T.D., Fundamentals of vehicle dynamics. 1992, Warrendale, Pennsylvania: Society of Automotive Engineers.
5. Sharp, R.S. and C. Pilbeam. Achievability and value of passive suspension designs for minimum pitch response. in IMechE International Conference–Vehicle Ride and Handling. 1993. Birmingham.
6. Griffin, M.J., Discomfort from feeling vehicle vibration. Vehicle System Dynamics, 2007. 45: p. 679-698.
7. Evaluation of human exposure to whole-body vibration - part 1: general requirements, in ISO 2631-1. 1997.
8. Kinetic. Cannonball productions. 2005 [cited 13 July 2008]; Company Website]. Available from: http://www.kinetic.com.au.
9. Zhang, N., et al., Determination of modal parameters of a half-car fitted with a hydraulically interconnected suspension from simulated free decay responses, in Australasian Congress on Applied Mechanics (5th : 2007 : Brisbane, Qld.). 2007, Engineers Australia: Brisbane, Qld.
10. Jeyakumaran, J., W. Smith, and N. Zhang, Transient characteristics of a hydraulically interconnected suspension system, in SAE World Congress & Exhibition, April 2007. 2007, SAE International: Detroit, MI, USA.
11. Wilde, J.R., et al., Experimental evaluation of fishhook maneuver performance of a Kinetic Suspension System. SAE Technical Paper Series, 2005. SAE 2005-01-0392.

12. Smith, A.W., An investigation into the dynamics of vehicles with hydraulically interconnected suspensions, in Faculty of Engineering and Information Technology. 2009, University of Technology, Sydney: Australia. p. 213.
13. Shedlowsky, J.P., Interior noise control in an automobile - a complex and significant challenge, in Inter-Noise 92. 1992: Toronto. p. 1073-1078.
14. Fahy, F.J., Sound and structural vibration: radiation, transmission and response. 1987, London: Academic Press.
15. Smith, M.C. and G.W. Walker, Interconnected vehicle suspension. Proceedings of the Institution of Mechanical Engineers, Part D: Journal of Automobile Engineering, 2005. 219(3): p. 295-307.
16. Pevsner, J.M., Equalizing types of suspension. Automobile Engineer, 1957: p. 10-16.
17. Hawley, J.B., Shock absorber and the like for vehicles. 1927: US Patent.
18. Moulton, A.E. and A. Best, Hydragas suspension. SAE Technical Paper Series, 1979. SAE 790374.
19. Rideout, G. and R.J. Anderson, Experimental testing and mathematical modeling of the interconnected Hydragas suspension system. SAE Transactions, 2003. 112(6): p. 280- 288.
20. Moulton, A.E. and A. Best, Rubber springs and inter-connected suspension systems. Engineering Design Show Conference, 1970. No. 15a: p. 1-31.
21. Tanahashi, H., et al., Toyota electronic modulated air suspension for the 1986 soarer. SAE Technical Paper Series, 1987. SAE 870541.
22. Iijima, T., et al., Development of a hydraulic active suspension. SAE Technical Paper Series, 1993. SAE 931971.
23. Liu, P.J., An analytical study of ride and handling performance of an interconnected vehicle suspension. 1994, Concordia University.
24. Liu, P.J., S. Rakheja, and A.K.W. Ahmed, Analytical study of an interconnected vehicle suspension, in Proceedings of the 1995 ASME International Mechanical Engineering Congress and Exposition. 1995: San Francisco, USA. p. 151-160.
25. Liu, P.J., S. Rakheja, and A.K.W. Ahmed, Properties of an interconnected hydro-pneumatic suspension system. Transactions of the Canadian Society for Mechanical Engineering, 1995. 19(4): p. 383-396.

26. Rakheja, S., et al., Analysis of an interlinked hydro-pneumatic suspension, in Proceedings of the 1993 ASME Winter Annual Meeting. 1993: New Orleans, USA. p. 279-288.
27. Fontdecaba i Buj, J., Integral suspension system for motor vehicles based on passive components. SAE Technical Paper Series, 2002. SAE 2002-01-3105.
28. Ortiz, M., Principles of interconnected suspension, in RaceCar Engineering. 1997. p. 56-59, 76-81.
29. Zapletal, E., Balanced suspension. SAE Technical Paper Series, 2000. SAE 2000-01- 3572.
30. Mace, N., Analysis and synthesis of passive interconnected vehicle suspensions. 2004, University of Cambridge: Cambridge, UK.
31. Mavroudakis, B. and P. Eberhard, Mode decoupling in vehicle suspensions applied to race cars, in III European Conference on Computational Mechanics: Solids, Structures and Coupled Problems in Engineering. 2006: Lisbon, Portugal.
32. Dowell, E.H. and K.C. Hall, Modeling of fluid-structure interaction. Annual Reviews of Fluid Mechanics, 2001. 33(445-90).
33. Bungartz, H.-J. and M. Schäfer, eds. Fluid-structure interaction - modelling, simulation, optimisation. Lecture Notes in Computational Science and Engineering, ed. T.J. Barth, et al. Vol. 53. 2006, Springer: Netherlands.
34. Tijsseling, A.S., Fluid-structure interaction in liquid-filled pipe systems: a review. Journal of Fluids and Structures (UK), 1996. 10(2): p. 109-146.
35. Skalak, R., An extension of the theory of waterhammer. Transactions of ASME, 1956. 78: p. 105-116.
36. Wiggert, D.C. and A.S. Tijsseling, Fluid transients and fluid-structure interaction in flexible liquid-filled piping. Applied Mechanics Reviews, 2001. 54(5): p. 455-481.
37. Tijsseling, A.S. and C.S.W. Lavooij, Waterhammer with fluid-structure interaction. Applied Scientific Research, 1990. 47(3): p. 273-285.
38. Zhang, L., Y. Guo, and S. He, Numerical simulation of three-dimensional incompressible fluid in a box flow passage considering fluid-structure interaction by differential quadrature method. Applied Mathematical Modelling, 2007. 31(9): p. 2034-2049.
39. Kulak, R.F., Three-dimensional fluid-structure coupling in transient analysis. Computers & Structures, 1985. 21(3): p. 529-542.

40. Szabó, G. and J. Györgyi, Three-dimensional fluid-structure interaction analysis for bridge aeroelasticity, in Proceedings of the World Congress on Engineering and Computer Science 2009, WCECS 2009. 2009: San Francisco, USA.
41. Tam, D.S.W., A two-dimensional fluid-structure coupling algorithm for the interaction of high-speed flow with open shells, in Department of Aeronautics and Astronautics. 2004, Massachusetts Institute of Technology: Cambridge, MA, USA. p. 94.
42. Hart, J.D., et al., A two-dimensional fluid–structure interaction model of the aortic value. Journal of Biomechanics, 2000. 33(9): p. 1079-1088.
43. Čanić, S., A. Mikelić, and J. Tambača, A two-dimensional effective model describing fluid-structure interaction in blood flow: analysis, simulation and experimental validation. Comptes Rendus Mécanique, 2005. 333(12): p. 867-883.
44. Wiggert, D.C., Coupled transient flow and structural motion in liquid-filled piping systems: a survey, in Proceedings of the ASME Pressure Vessels and Piping Conference. 1986, American Society of Mechanical Engineers: Chicago, U.S.A.
45. Li, Q.S., et al., Frequency domain analysis of fluid-structure interaction in liquid-filled pipe systems by transfer matrix method. International Journal of Mechanical Sciences, 2002. 44(10): p. 2067-2087.
46. Zhang, L., S.A. Tijsseling, and E.A. Vardy, FSI analysis of liquid-filled pipes. Journal of Sound and Vibration, 1999. 224(1): p. 69-99.
47. Li, Q.S., K. Yang, and L. Zhang, Analytical solution for fluid-structure interaction in liquid-filled pipes subjected to impact-induced water hammer. Journal of Engineering Mechanics, 2003. 129(12): p. 1408-1417.
48. Yang, K., Q.S. Li, and L. Zhang, Longitudinal vibration analysis of multi-span liquid-filled pipelines with rigid constraints. Journal of Sound and Vibration, 2004. 273(1-2): p. 125-147.
49. Hu, C.K. and J.W. Phillips, Pulse propagation in fluid-filled elastic curved tubes. ASME Journal of Pressure Vessel Technology, 1981. 103: p. 43-49.
50. Valentin, R.A., J.W. Phillips, and J.S. Walker, Reflection and transmission of fluid transients at an elbow, in Transactions of SMiRT5. 1979, Structure Mechanics in Reactor Technology: Berlin, Germany.
51. Tijsseling, A.S., Water hammer with fluid-structure interaction in thick-walled pipes. Computers & Structures, 2007. 85(11-14): p. 844-851.

52. Heinsbroek, A.G.T.J., Fluid-structure interaction in non-rigid pipeline systems. Nuclear Engineering and Design, 1997. 172(1-2): p. 123-135.
53. D'souza, A.F. and R. Oldenburger, Dynamic response of fluid lines. ASME Journal of Basic Engineering, 1964. 86: p. 589-598.
54. Wilkinson, D.H., Acoustic and mechanical vibrations in liquid-filled pipework systems, in Proceedings of the BNES International Conference on Vibration in Nuclear Plant. 1978, British Nuclear Energy Society: Keswick, UK. p. 863-878.
55. Kuiken, G.D.C., Amplification of pressure fluctuations due to fluid-structure interaction. Journal of Fluids and Structures, 1988. 2(5): p. 425-435.
56. Lesmez, M.W., Modal analysis of vibrations in liquid-filled piping systems, in Department of Civil and Environmental Engineering. 1989, Michigan State University: East Lansing, Michigan, USA.
57. Lesmez, M.W., D.C. Wiggert, and F.J. Hatfield, Modal analysis of vibrations in liquid-filled piping-systems. ASME Journal of Fluids Engineering, 1990. 112: p. 311-318.
58. Tentarelli, S.C., Propagation of noise and vibration in complex hydraulic tubing systems, in Department of Mechanical Engineering. 1990, Lehigh University: Pennsylvania, United States. p. 163.
59. Brown, F.T. and S.C. Tentarelli, Analysis of noise and vibration in complex tubing systems with fluid-wall interactions, in Proceedings of the 43rd National Conference on Fluid Power. 1988: Chicago, USA. p. 139-149.
60. Brown, F.T. and S.C. Tentarelli, Dynamic Behavior of Complex Fluid-Filled Tubing Systems, Part 1: Tubing Analysis. Journal of Dynamic Systems, Measurement, and Control, 2001. 123(1): p. 71-77.
61. Tentarelli, S.C. and F.T. Brown, Dynamic Behavior of Complex Fluid-Filled Tubing Systems, Part 2: System Analysis. Journal of Dynamic Systems, Measurement, and Control, 2001. 123(1): p. 78-84.
62. Jong, C.A.F.D., Analysis of pulsations and vibrations in fluid-filled pipe systems, in Institute of Applied Physics. 1994, Eindhoven University of Technology: Delft, Netherlands. p. 170.
63. Svingen, B., Fluid-structure interaction in piping systems. 1996, Norwegian University of Science and Technology (Norway): Ann Arbor. p. 129.

64. Edge, K.A. and D.N. Johnston, The impedance characteristics of fluid power components: relief valves and accumulators. Proc IMechE, Part I: Journal of Systems and Control Engineering, 1991. 205: p. 11-22.
65. Johnston, D.N. and K.A. Edge, The impedance characteristics of fluid power components: restrictor and flow control valves. Proc IMechE, Part I: Journal of Systems and Control Engineering, 1991. 205: p. 3-10.
66. Edge, K.A. and D.G. Tilley, The use of plane wave theory in the modelling of pressure ripple in hydraulic systems. Transactions of the Institute of Measurement and Control, 1983. 5(4): p. 171-178.
67. Johnston, D.N. and K.A. Edge, Simulation of the pressure ripple characteristics of hydraulic circuits. Proceedings of the Institution of Mechanical Engineers, Part C: Journal of Mechanical Engineering Science, 1989. 203(C4): p. 275-282.
68. Johnston, D.N. and K.A. Edge, In-situ measurement of the wavespeed and bulk modulus in hydraulic lines. Proc IMechE, Part I: Journal of Systems and Control Engineering, 1991. 205: p. 191-197.
69. Ionescu, F., Some aspects concerning nonlinear mathematical modeling and behaviour of hydraulic elements and systems. Nonlinear Analysis, 1997. 30(3): p. 1447-1460.
70. Taylor, S.E.M., Development of numerical models for hydraulic pipelines and flexible hoses. 1998, University of Bath. p. 253.
71. Longmore, D.K., The transmission and attenuation of fluid borne noise in hydraulic hose, in Institution of Mechanical Engineers Seminar on Quiet Oil Hydraulic Systems. 1977, Mechanical Engineering Publications: London. p. 127-138.
72. Longmore, D.K. and B. Tuc, Reduction of fluid borne noise in hydraulic circuits by means of flexible hoses, in Institution of Mechanical Engineers Seminar on Quieter Oil Hydraulics. 1980: London.
73. Johnston, D.N., A time-domain model of axial wave propagation in liquid-filled flexible hoses. Proceedings of the Institution of Mechanical Engineers, Part I: Journal of Systems and Control Engineering, 2006. 220(7): p. 517-530.
74. Drew, J.E., The use of flexible hose to reduce pressure ripple in power steering. 1997, University of Bath. p. 225.
75. Drew, J.E., D.K. Longmore, and D.N. Johnston, Measurement of the longitudinal transmission characteristics of fluid-filled hoses. Proceedings of the Institu-

tion of Mechanical Engineers,Part I: Journal of Systems & Control Engineering, 1997. 211(3): p. 219-228.

76. Drew, J.E., D.K. Longmore, and D.N. Johnston, Theoretical analysis of pressure and flow ripple in flexible hoses containing tuners. Proceedings of the Institution of Mechanical Engineers, Part I: Journal of Systems and Control Engineering, 1998. 212(6): p. 405-422.
77. Longmore, D.K. and A. Schlesinger, Transmission of vibration and pressure fluctuations through hydraulic hoses. Proceedings of the Institution of Mechanical Engineers, Part I: Journal of Systems and Control Engineering, 1991. 205(I2): p. 94-104.
78. Longmore, D.K. and A. Schlesinger, Relative importance of the various vibration transmitting mechanisms in hoses in typical hydraulic systems. Proceedings of the Institution of Mechanical Engineers, Part I: Journal of Systems and Control Engineering, 1991. 205(I2): p. 105-111.
79. Tuc, B., Comparison of vibration transmission mechanism in hydraulic hoses. Journal of the Institute of Science and Technology of Erciyes University, 1985. 1: p. 257-277.
80. Longmore, D.K. and C.W. Stammers. Combined longitudinal and lateral vibration of a curved reinforced hose. in Proceedings of the International Conference on Recent Advances in Structural dynamics, I.S.V.R. 1980. Southampton, UK: Institute of Sound and Vibration Research, University of Southampton.
81. Longmore, D.K., C.W. Stammers, and B. Tuc, Measurement of the longitudinal wave propagation properties of reinforced flexible hose, in The Institute of Acoustics Spring Conference. 1981: Newcastle. p. 75-78.
82. Longmore, D.K., D.N. Johnston, and J.E. Drew, Measurement of the dynamic properties of hose walls required for modelling fluid-borne noise, in Proceedings of the 1997 ASME International Mechanical Engineering Congress and Exposition. 1997, The Fluid Power and Systems Technology Division (Publication) FPST: Dallas, TX, USA. p. 105-111.
83. Johnston, D.N., M.W. Tim, and M.C. Kerry, Measurement of wave propagation characteristics of flexible hoses, in ASME 2007 International Mechanical Engineering Congress and Exposition (IMECE2007). 2007, ASME: Seattle, Washington, USA p. 159-167.

84. Yu, J. and E. Kojima, Wave propagation in fluids contained in finite-length anisotropic viscoelastic pipes. Journal of the Acoustical Society of America, 1998. 104(6): p. 3227-3235.
85. Evans, J.J. and P.D. Wilcox, A structural model for high pressure helical wire-wound thermoplastic hose. International Journal of Solids and Structures, 2002. 39(5): p. 1307-1326.
86. Prek, M., Analysis of wave propagation in fluid-filled viscoelastic pipes. Mechanical Systems and Signal Processing, 2007. 21(4): p. 1907-1916.
87. Kleinsteuber, S. and N. Sepehri, A polynomial network modeling approach to a class of large-scale hydraulic systems. Computers & Electrical Engineering, 1996. 22(2): p. 151-168.
88. Cobo, M., R. Ingram, and S. Cetinkunt, Modeling, identification, and real-time control of bucket hydraulic system for a wheel type loader earth moving equipment. Mechatronics, 1998. 8(8): p. 863-885.
89. Mrad, R.B., J.A. Levitt, and S.D. Fassois, Non-linear dynamic modeling of an automobile hydraulic active suspension system. Mechanical Systems and Signal Processing, 1994. 8(5): p. 485-517.
90. Qatu, M., D. Llewellyn, and R. Edwards, Correlation of hydraulic circuit dynamic simulation and vehicle. SAE Technical Paper Series, 2000. SAE 2000-01-0811: p. 103-112.
91. Chaudhry, M.H., Applied hydraulic transients. 2nd ed. 1987, New York, USA: Van Nostrand Reinhold Company.
92. Wylie, E.B., V.L. Streeter, and L. Suo, Fluid transients in systems. 1993, Englewood Cliffs, New Jersey: Prentice Hall, Inc.
93. Tesar, A. and L.u. Fillo, Transfer Matrix Method. Mathematics and its Applications. East European series, ed. M. Hazewinkel. 1988, Czechoslovakia: Kluwer Academic Publishers.
94. Rocard, Y., Les phénomènes d'auto-oscillation dans les installations hydrauliques. Théories mécaniques. Vol. 9. 1937, Paris Hermann.
95. Paynter, H.M., Electrical Analogies and Electronic Computers: A Symposium: Surge and Water Hammer Problems. Transactions of the American Society of Civil Engineers, 1953. 118(1): p. 962-989.

96. Waller, E.J., Prediction of pressure surges in pipelines by theoretical and experimental methods. 1958, Stillwater Oklahoma: Engineering Experiment Station, Oklahoma State University.
97. Wylie, E.B., Resonance in pressurized piping systems. Journal of Fluids Engineering, 1965. 87(4): p. 960-966.
98. Wylie, E.B. and V.L. Streeter, Fluid transients. 1983: FEB Press.
99. Pestel, E. and F.A. Leckie, Matrix methods in elastomechanics. 1963, New York: McGraw-Hill.
100. Molloy, C.T., Use of four pole parameters in vibration calculations. Journal of the Acoustical Society of America, 1957. 29(7): p. 842-853.
101. Reed, M.B., Electrical network synthesis. 1955, New York: Prentice-Hall, Inc.
102. Chaudhry, M.H., Resonance in pressurized piping systems. 1970, University of British Columbia: Canada. p. 222.
103. Chaudhry, M.H., Resonance in pipe systems, in Water Power. 1970: London. p. 241-245.
104. Chaudhry, M.H., Resonance in pressurized piping systems. ASCE: Journal of Hydraulics Division, 1970. 96: p. 1819-1839.
105. Chaudhry, M.H., Resonance in pipes having variable characteristics. ASCE: Journal of Hydraulics Division, 1972. 98(2): p. 325-333.
106. MATLAB®. MATLAB Help. [cited 14 November 2012]; MATLAB 7.1.
107. MATLAB®. MATLAB: The language of technical computing. [cited 14 November 2012]; Available from: http://www.mathworks.com.au/products/matlab/.
108. National Instruments. NI LabVIEW. [cited 14 November 2012]; Available from: http:// www.ni.com/labview/whatis/.
109. National Instruments. LabVIEW Help. [cited 14 November 2012]; LabVIEW 2012.
110. Cowper, G.R., The shear coefficient in Timoshenko's beam theory. ASME Journal of Applied Mechanics, 1966. 33: p. 335-340.
111. Vigness, I., Elastic properties of curved tubes. Transactions of the ASME, 1943. 65: p. 105-120.
112. Timoshenko, S., D.H. Young, and W. Weaver Jr., Vibration problems in engineering. 4th ed. 1974, USA: John Wiley & Sons.
113. Cremer, L., M. Heckl, and E.E. Ungar, Structure-Borne Sound. 2nd Edition ed. 1988, Berlin & New York: Springer-Verlag.

114. Zhang, N. and S. Hayama, Identification of structural system parameters from time domain data: identification of global modal parameters of structural system by the improved state variable method. JSME International Journal, 1990. 33(2): p. 168-175.
115. Zaruba, J., Water hammer in pipe-line systems. 1993, Czechoslovakia: Elsevier Science Publishers.
116. Johnston, D.N., K.A. Edge, and M. Brunelli, Impedance and stability characteristics of a relief valve. Proceedings of the Institution of Mechanical Engineers, Part I: Journal of Systems and Control Engineering, 2002. 216(I5): p. 371-382.
117. Brunelli, M., D.N. Johnston, and K.A. Edge, Impedance characteristics of cartridge relief valve, in 8th Scandinavian International Conference on Fluid Power. 2003: Tampere, Finland.
118. Lau, K.K., K.A. Edge, and D.N. Johnston, Impedance characteristics of hydraulic orifices. Proceedings of the Institution of Mechanical Engineers, Part I: Journal of Systems and Control Engineering, 1995. 209(4): p. 241-253.
119. Stecki, J.S. and D.C. Davis, Fluid transmission lines - distributed parameter models, part 1: a review of the state of the art. Proceedings of the Institution of Mechnical Engineers, Part A: Power and Process Engineering, 1986. 200(A4): p. 215-228.
120. Stecki, J.S. and D.C. Davis, Fluid transmission lines - distributed parameter models, part 2: comparison of models. Proceedings of the Institution of Mechnical Engineers, Part A: Power and Process Engineering, 1986. 200(A4): p. 229-236.
121. MATLAB®. SimHydraulics: Fixed Orifice. [cited 8 September 2013]; Available from: http://www.mathworks.com.au/help/physmod/hydro/ref/fixedorifice.html.
122. MATLAB®. SimHydraulics: Gas-Charged Accumulator. [cited 8 September 2013]; Available from: http://www.mathworks.com.au/help/physmod/hydro/ref/gaschargedaccu mulator.html.
123. PCB Piezotronics. PCB Products. [cited 25 October 2013]; Available from: http://www.pcb.com/products.aspx?s=111a26.
124. Wikipedia. Steel. [cited 11 March 2010]; Available from: http://enwikipedia.org/wiki/Steel.
125. Density of Steel. [cited 13 November 2010]; Available from: http://hypertextbook.com/facts/2004/KarenSutherland.shtml.

126. Wikipedia. Young's modulus. [cited 11 March 2010]; Available from: http://en.wikipedia.org/wiki/Young%27s_modulus.
127. Wikipedia. Shear modulus. [cited 11 March 2010]; Available from: http://en.wikipedia.org/wiki/Shear_modulus.
128. Wikipedia. Poisson's ratio. [cited 1 April 2010]; Available from: http://en.wikipedia.org/wiki/Poisson%27s_ratio.
129. Parker. Gates M4K Hydraulic Hose. 2013 [cited 5 October 2013]; Available from: http:// www.parkerhydraulics.co.uk/hydraulics/m4k/.
130. Hydraulink. Product List: Hose. [cited 5 October 2013]; Available from: http://www.hydraulink.com/hose.
131. Matbase. Material Properties of Nitrile Rubber. [cited 25 March 2010]; Available from: http://www.matbase.com/material/polymers/elastomers/nitrile-rubber/ properties.
132. Zhao, J., Vibration of hydraulically interconnected suspensions due to fluid-structure interaction, in Proceedings of the 13th Asia-Pacific Vibration Conference. 2009: Christchurch, New Zealand.
133. Wiggert, D.C., F.J. Hatfield, and S. Struckenbruck, Analysis of liquid and structural transients in piping by the method of characteristics. ASME Journal of Fluids Engineering, 1987. 109: p. 161-165.
134. Wikipedia. Stiff equation. [cited 30 April 2014]; Available from: http://en.wikipedia.org/wiki/Stiff_equation.